Simulating the Low Redshift UV Background and the Absorber-Galaxy Connection

by

Joshua Moloney

B.A., Washington University in St. Louis, 2011

M.S., University of Colorado Boulder, 2013

A thesis submitted to the

Faculty of the Graduate School of the

University of Colorado in partial fulfillment

of the requirements for the degree of

Doctor of Philosophy

Department of Astrophysical & Planetary Sciences

2017

This thesis entitled:
Simulating the Low Redshift UV Background and the Absorber-Galaxy Connection
written by Joshua Moloney
has been approved for the Department of Astrophysical & Planetary Sciences

Prof. J. Michael Shull

Prof. James C. Green

Prof. Mitchell C. Begelman

Dr. Benjamin Oppenheimer

Prof. Kevin Stenson

Date

The final copy of this thesis has been examined by the signatories, and we find that both the content and the form meet acceptable presentation standards of scholarly work in the above mentioned discipline.

Moloney, Joshua (Ph.D., Astrophysical & Planetary Sciences)

Simulating the Low Redshift UV Background and the Absorber-Galaxy Connection

Thesis directed by Prof. J. Michael Shull

The majority of baryons in the low-redshift universe are found in the intergalactic medium (IGM) and circumgalactic medium (CGM). Understanding the thermal and ionization state of this gas can provide insights into numerous astrophysical problems, including the distribution of baryons in the universe, the intensity of the metagalactic ionizing UV radiation background (UVB), and the nature of the flows of gas that connect galaxies to their environments. This thesis uses cosmological simulations of the IGM and CGM to study two of these problems. The first part of the thesis focuses on constraining the nature of the low-redshift UVB. By comparing simulations run with a range of UVB prescriptions to observations of the column-density distribution of H I absorption lines, we find that the $z = 0$ UVB has approximately twice the intensity of the commonly used Haardt & Madau (2012) background. We begin to test the assumption of a spatially uniform UVB by post-processing one of our simulations to include the effects of local density variations on the UVB intensity. We find that these local variations are unimportant for lower column density ($N_{HI} \lesssim 10^{15}$ cm^{-2}) absorption lines associated with the IGM and the CGM of low-mass galaxies, but they become significant for partial Lyman-limit systems and Lyman-limit systems associated with the most massive halos.

The second portion of the thesis traces the distribution of highly ionized oxygen in circumgalactic gas out to distances of five virial radii. Ionization models using both collisional ionization equilibrium (CIE) and collisional + photoioinization equilibrium (C+P) predict distributions of O VI within the virial radius that are consistent with observations. The overall spatial distributions of O VI differ significantly between the models, with high O VI column densities extending to impact parameters of $4r_{vir}$ in the CIE model, but restricted to within $1.5r_{vir}$ for C+P. The C+P model also predicts high column densities of O VIII, potentially detectable by future X-ray

observations, out to distances of $3r_{vir}$. The overall broad distribution of ionized oxygen indicates that metal-enriched galactic outflows play an important role in the evolution of the surrounding IGM.

Contents

Chapter

Tables

Table

Figures

Figure

Chapter 1

Tracing the Cosmic Baryons

Observations of the cosmic microwave background (CMB) provide information on the mean densities of the various components that make up our universe, including baryonic matter. For a flat ΛCDM cosmology, the mean baryon density at $z = 0$ is given by

$$\rho_b = \frac{3{H_0}^2}{8\pi G}\Omega_b, \tag{1.1}$$

where H_0 is the Hubble constant and Ω_b is the baryon density parameter. The Planck concordance cosmological parameters of $H_0 = 67.74$ km s^{-1} Mpc^{-1} and $\Omega_b = 0.04860$ (Planck Collaboration et al. 2016) imply a mean baryon density of 4.189×10^{-31} g cm^{-3}, which corresponds to a hydrogen number density of $n_H = 1.88 \times 10^{-7}$ cm^{-3} for a primordial helium abundance of $Y_p = 0.2470$ (Cyburt et al. 2016).

With robust theoretical estimates for Ω_b provided by the CMB and primordial nucleosynthesis, there has been a significant effort made over the past several decades to complete an observational census of baryons in the low-redshift ($z \lesssim 0.5$) universe. The earliest attempts focused on luminous matter in galaxies and X-ray emitting hot gas in the intracluster medium (ICM) and found that these reservoirs accounted for only $\sim 10\%$ of the cosmic baryons (Persic & Salucci 1992). Even generous assumptions about the galaxy luminosity function and the presence of gas within galaxy groups resulted in baryon densities that were half of the cosmological prediction (Bristow & Phillipps 1994; Fukugita et al. 1998). This deficit was termed the "missing baryons problem."

Observations of active galactic nuclei (AGN) with UV spectrographs including the Goddard High-Resolution Spectrograph and Space Telescope Imaging Spectrograph on the *Hubble Space*

Telescope (HST) and the *Far Ultraviolet Spectroscopic Explorer* (FUSE) led to the detection of absorption lines tracing large reservoirs of gas in the intergalactic medium (IGM). This gas included both a warm ($T \leq 10^5$ K) phase traced by the Lyα forest (Penton et al. 2004) as well as the warm-hot intergalactic medium (WHIM) traced by broad (line width $b \geq 40$ km s^{-1}) Lyα as well as O VI (Sembach et al. 2004). By the mid 2000s, it was clear that the IGM contained the majority of the missing baryons (Shull 2003; Danforth & Shull 2005; Bregman 2007).

Numerous surveys with ever larger numbers of AGN sight lines have improved the baryon census of the intergalactic medium, as well as detected an additional reservoir of baryons in the circumgalactic medium (CGM), within the virial radius (r_{vir}) of galaxies. Figure 1.1 shows a summary of the modern baryon census from Shull et al. (2012b). Over half of the cosmic baryons are located in the IGM, with $28 \pm 11\%$ in the Lyα forest and $29 \pm 10\%$ in the WHIM. Smaller portions of the baryon budget are contained in galaxies ($7 \pm 2\%$), CGM ($5 \pm 3\%$), ICM ($4 \pm 1.5\%$), and cold atomic gas ($1.7 \pm 0.4\%$). This census leaves $29 \pm 13\%$ of the cosmic baryons unaccounted for. Much of this gas likely exists either in a hot ($T > 10^6$ K) phase of the IGM that cannot be detected in O VI or trace amounts of broad Lyα lines (Shull et al. 2012b) or in hot space-filling gas within galaxy groups (Stocke et al. 2013).

Detecting these remaining gas reservoirs is important for reasons beyond completing the baryon census. Understanding the distribution of gas across various phases of the IGM provides insight into the physical processes responsible for determining the thermal and ionization state of the gas. In addition, the contents of these various phases are not static; baryons flow from the IGM into the CGM and galaxies and back out again, and these flows play a crucial role in the evolution of the universe. The remainder of this chapter describes in greater detail the current understanding of the distribution of baryons within the universe, as well as the flows of baryons between the various phases.

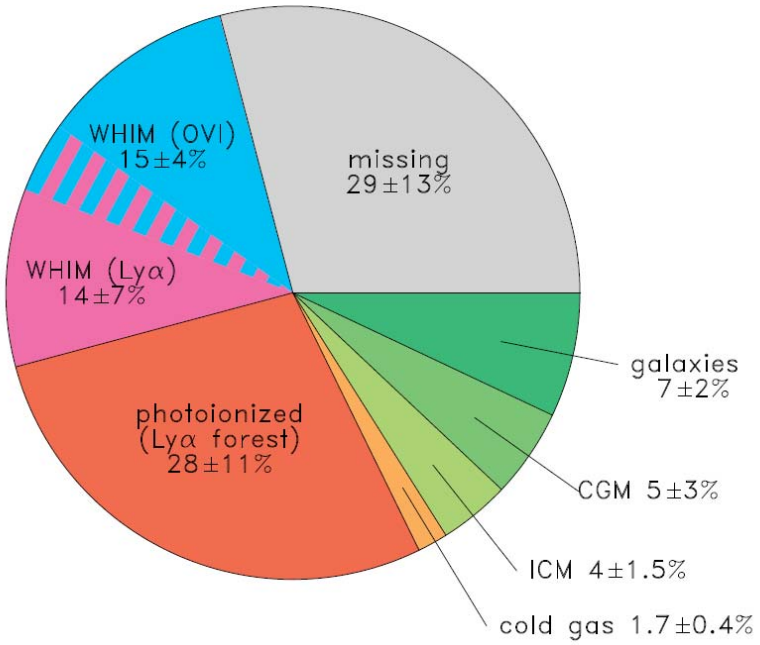

Figure 1.1 Summary of the cosmic baryon census from Shull et al. (2012b). The majority of the cosmic baryons are found in the IGM, with less than 10% found in galaxies and an additional 5% in the CGM. Of the $\sim 30\%$ of baryons that are still unaccounted for, roughly half are likely found in hot ($T > 10^6$ K) phases of the IGM and much of the remainder may be in a space-filling medium within galaxy groups.

1.1 Observing Baryons in AGN Spectra

The low density of gas in the CGM and IGM means that it cannot typically be detected in emission (although see Cantalupo et al. 2014 for an exception). Detecting gas in absorption requires a bright background light source. The high luminosity of AGN makes them useful light sources at cosmological distances. In addition, despite a large number of broad emission lines (see Shull et al. 2012c for a list of prominent lines), AGN are relatively lacking in intrinsic absorption features, and the underlying spectra can be well characterized by a power law in the UV (Telfer et al. 2002; Scott et al. 2004; Shull et al. 2012c; Stevans et al. 2014; Lusso et al. 2015; Tilton et al. 2016). This makes the identification of absorption lines due to foreground gas relatively straightforward. The disadvantage of AGN is that they are rare point sources of emission, so they typically provide only a one-dimensional picture of the intervening material. Inferring information about the three-dimensional properties of observed structures requires either numerical modeling or the presence of multiple bright AGN with small angular separations (e.g., Keeney et al. 2013), an extremely rare occurrence. Using galaxies as background sources would provide significantly better sampling of coherent structures in the IGM and CGM, but their complex intrinsic spectra, arising from multiple stellar populations of various ages and metallicities, make the identification and measurement of foreground absorption features problematic.

A single AGN sight line does not probe a sufficient pathlength to develop a robust statistical picture of the distribution of gas in the IGM. Penton et al. (2004) made their estimate of the baryon content of the Lyα forest using 15 AGN spectra covering a total redshift pathlength of $\Delta z = 0.770$. Subsequent surveys of the IGM, including Lehner et al. (2007), Danforth & Shull (2008), Tripp et al. (2008), Danforth et al. (2010), and Tilton et al. (2012) have included an increasing number of sight lines. Danforth et al. (2016), the largest IGM survey to date, includes 82 AGN sight lines observed with the Cosmic Origins Spectrograph (Green et al. 2012) on the *HST* covering a total pathlength of $\Delta z = 21.7$ in the Lyα absorption line of H I.

Despite the highly ionized nature of the low-redshift IGM, the overall abundance of hydrogen

and the strength of the UV transitions of H I means that Lyα and higher-order Lyman-series lines are by far the most commonly observed absorption lines in AGN spectra. Numerous metal absorption species are also observed in the IGM and CGM, with the O VI doublet at $\lambda\lambda$1032, 1038 Å being the mostly commonly observed metal line. O VI is particularly important because its peak collisional ionization abundance occurs at $T \approx 10^{5.5}$ K, which corresponds to the middle of the temperature range of the WHIM. Other strong UV absorption lines include C III λ977, C IV $\lambda\lambda$1548, 1551, Si III λ1207, Si IV $\lambda\lambda$1394, 1403, and N V $\lambda\lambda$1239, 1243 (Danforth & Shull 2008). At temperatures above 10^6 K, the previously mentioned species have been ionized away. Gas in the hot phase of the IGM must be detected through X-ray transitions of higher ions, including O VII Kα, O VIII Kα and Kβ, and C V Kα.

1.2 Ionization of the IGM and CGM

Column densities ($N_{\rm ion}$) of absorption lines are determined by Voigt profile fitting or by comparing measured equivalent widths to a curve of growth. Individual column density measurements are then combined to create an overall distribution of column densities per unit redshift $\partial^2\mathcal{N}/\partial\log(N_{\rm ion})\partial z$. Converting this distribution to an overall baryon density traced by the atomic species requires additional information about the metal abundances and ionization state of the gas. Tilton et al. (2012) provide a method for calculating the overall IGM density (relative to the critical density) traced by a given ion as

$$\Omega_{\rm IGM}^{\rm (ion)} = \frac{1.83\times10^{-23}h_{70}^{-1}{\rm cm}^{-2}}{Z(M/H)_\odot f_{\rm ion}} \times \int_0^{z_{\rm max}} \int_{N_{\rm min}}^{N_{\rm max}} \frac{\partial^2\mathcal{N}}{\partial\log(N_{\rm ion})\partial z} N_{\rm ion} d\log(N_{\rm ion}) dz, \qquad (1.2)$$

where Z is the metallicity, $(M/H)_\odot$ is the metal abundance relative to Solar values, and $f_{\rm ion}$ is the fractional abundance of the given ion. For hydrogen absorption lines the dependence on metallicity is no longer present, but the correction for the neutral hydrogen fraction remains. Therefore, an accurate baryon census requires a good understanding of the ionization state of the CGM and IGM.

If absorption lines from multiple atomic species are present at the same redshift, the ionization state of the gas can be determined through numerical modeling with an ionization code such as

CLOUDY (Ferland et al. 2013) or XSTAR (Bautista & Kallman 2001). However, most H I and many O VI absorption lines are not accompanied by other ions. In this case, a simpler model must be used to estimate the ionization state of the gas. In general, ionization is determined by a balance between collisional ionization, photoionization, and radiative recombination. Both the collisional ionization and radiative recombination rates depend on the gas temperature and the hydrogen number density (or, equivalently, the electron number density n_e). The photoionization rate depends only on the flux of ionizing photons ($\Gamma_{\rm ion}$). Many of these values cannot be measured directly from the absorption lines and instead must be assumed based on global properties of the IGM or from analytic models. Shull et al. (2012b) provide a discussion of the assumptions that need to be made for Lyα absorbers.

The low density of the IGM and the photoionizing flux available from AGN mean that collisional ionization is typically unimportant for determining the H I ionization fraction. In addition, the low-redshift IGM has a large mean free path for hydrogen-ionizing Lyman continuum (LyC) photons. This means that one of the most important parameters for determining $f_{\rm HI}$ is the value of $\Gamma_{\rm H}$ for a mean metagalactic ionizing UV background (UVB). Ionizing photons in the low-redshift universe come primarily from AGN. Their overall contribution to the ionizing background is determined by combining an AGN UV luminosity function (e.g., Hopkins et al. 2007; Croom et al. 2009; Palanque-Delabrouille et al. 2013) with a mean power-law spectral slope measured from an AGN composite spectrum (e.g., Telfer et al. 2002; Scott et al. 2004; Shull et al. 2012c; Stevans et al. 2014; Lusso et al. 2015; Tilton et al. 2016). Additional ionizing photons come from O and B stars within galaxies. However, the high opacity of the interstellar medium (ISM) to LyC radiation means that on average $< 3\%$ of these photons reach the IGM (Bridge et al. 2010; Siana et al. 2010), limiting their contribution to the low-redshift UVB. Combining these LyC radiation sources with a one-dimensional radiative transfer calculation for the IGM produces a model for the redshift evolution of $\Gamma_{\rm H}$. Many such models have been produced, with notable examples including Haardt & Madau (1996), Shull et al. (1999), Haardt & Madau (2001), which was updated in the 2005 release of CLOUDY, Faucher-Giguère et al. (2009), Haardt & Madau (2012), and Madau &

Haardt (2015). The $z = 0$ values of $\Gamma_{\rm H}$ predicted by the various backgrounds vary by a factor of ~ 6 (Table 3.1), making the choice of UVB very significant for the resulting ionization fractions.

1.3 Ionization State of the IGM and CGM

As shown Figure 1.1, most of the reservoirs containing the low-redshift baryons have been identified observationally. Despite the uncertainties inherent in ionization modeling with limited information, the general ionization states of many of these reservoirs are also well-constrained. The rest of this section summarizes the current observational understanding of the thermal and ionization states of gas in the IGM and CGM.

1.3.1 Lyα Forest

The largest survey of absorbers in the Lyα forest comes from Danforth et al. (2016), with 2256 H I absorption systems in their "uniform sample." The majority of these absorbers are associated with warm $T < 10^5$ K gas in the IGM, but some trace either hotter gas in the WHIM or gas within the CGM of galaxies located along the line of sight. An upper limit on the gas temperature for an absorber can be obtained by assuming that the line width (after correcting for the instrumental line spread function) is produced entirely by thermal broadening. For Lyα, a thermal line width of $b = 40.6$ km s^{-1} corresponds to $T = 10^5$ K, so lines with lower b-values are not associated with the WHIM. In the Danforth et al. (2016) survey, $\sim 73\%$ of the Lyα absorption lines have $b < 40.6$ km s^{-1}.

Determining which absorption systems may be associated with nearby galaxies is significantly more difficult. Galaxies surveys such as the Sloan Digital Sky Survey (SDSS Collaboration et al. 2016) do not have sufficient completeness to directly identify galaxy-absorber pairs. Instead, associations between H I absorption lines and nearby galaxies must be inferred through indirect means. One method is comparing the clustering of Lyα absorbers to that of galaxies. Danforth et al. (2016) found that absorbers with $N_{HI} < 10^{13.5}$ cm^{-2} have a two-point correlation function consistent with a random spatial distribution, while higher column density absorbers show a clus-

tering signal similar to that of galaxies for velocity offsets of $\Delta v \lesssim 100$ km s^{-1}. This potentially indicates a transition at $N_{HI} \approx 10^{13.5}$ cm^{-2} from absorbers primarily tracing the IGM to those tracing circumgalactic gas.

Metal absorption is rare in the Lyα forest; only $\sim$ 3% of the H I systems with $N_{HI} < 10^{13.5}$ cm^{-2} in Danforth et al. (2016) have associated metal lines. The ions most commonly associated with this low-temperature presumable photoionized gas are C III, C IV, Si III, and Si IV (Tilton et al. 2012; Danforth et al. 2016). Ionization modeling of the relative abundances of these species indicates that the Lyα forest is photoionized by a low-z background with $\Gamma_{\rm H} \approx 8 \times 10^{-14}$ s^1 (Shull et al. 2014), a value intermediate between the strengths of the various backgrounds in Table 3.1.

1.3.2 WHIM

Despite an increase in collisional ionization due to the higher gas temperature, H I is still an important tracer of IGM gas in the 10^5 K $< T < 10^6$ K range of the WHIM. Of the 2256 H I absorption systems in the Danforth et al. (2016) survey, $\sim$ 27% have line widths consistent with temperatures in this range. However, turbulent broadening of the lines means that the actual fraction of H I that traces the WHIM is lower. The exact breakdown of H I absorber temperatures is somewhat academic, as the 10^5 K temperature cutoff is arbitrary and all of the absorption systems contribute to the baryon census.

As the hydrogen neutral fraction decreases, metal absorption lines become increasingly important for tracing the IGM. Despite a peak collisional ionization abundance of ~ 0.2, lithium-like O VI is a particularly important tracer of the WHIM due to the strength of the $\lambda\lambda$1032, 1038 Å doublet and the fact that its collisional ionization abundance peaks at $T \approx 10^{5.5}$ K. Other useful metal ions are N V, C IV, and Ne VIII, with peak ionization fractions at $T \approx 10^{5.25}$ K, $T \approx 10^5$ K, and $T \approx 10^{5.8}$ K, respectively. Estimates of the baryon fraction contained in the WHIM depend on contributions from both H I and these metal species, so care must be taken to avoid counting these absorption systems twice (Danforth et al. 2010; Shull et al. 2012b).

At temperatures above 10^6 K, hydrogen in the IGM is almost entirely ionized and can no

longer be detected in absorption. This means that observations of the hot IGM rely entirely on highly ionized metals, in particular O VII, O VIII, C V, and C VI. The strongest spectral lines of these ions lie in the X-ray, and the relatively low effective areas and resolutions of the X-ray spectrographs on *Chandra* and *XMM Newton* make the detection of these lines difficult. Despite these difficulties, detections of X-ray absorption in the WHIM have been claimed along multiple sight lines (e.g., Nicastro et al. 2005, 2013; Fang et al. 2010; Bonamente et al. 2016). However, the number of absorption systems is still too small to provide a meaningful statistical sample, and many of the reported detections remain controversial (Yao et al. 2012). As a result, predictions for the fraction of baryons residing in hotter portions of the WHIM still rely mainly on the results of cosmological simulations. Shull et al. (2012b) find that $\sim 15\%$ of the cosmic baryons may be found in this X-ray-traced gas, using simulations from Smith et al. (2011).

1.3.3 CGM

The precise definition of the CGM is ambiguous, but it is often taken to refer to material located within the virial radius of a galaxy. The definition of r_{vir} also shows significant variation. It is typically taken to be the radius of a sphere centered on the galaxy for which the matter density within the sphere is equal to some virial overdensity (Δ_{vir}). However, the specific value of Δ_{vir} varies from paper to paper, and it is often unclear whether this density is measured relative to the critical density or the mean matter density. In this thesis, Δ_{vir} will be measured with respect to the critical density at the observed redshift of the galaxy and given by

$$\Delta_{vir}(z) = 18\pi^2 + 82\left[\Omega_m(z) - 1\right] - 39\left[\Omega_m(z) - 1\right]^2, \tag{1.3}$$

where $\Omega_m(z)$ is the matter density parameter at redshift z (Bryan & Norman 1998). For a full discussion of the various definitions of the virial radius, see Shull (2014).

Although large surveys of AGN absorption lines undoubtedly contain many absorbers located within the CGM of foreground galaxies, there has recently been considerable interest in creating surveys specifically targeting the CGM. These surveys specifically identify AGN sight lines that

pass near foreground galaxies and focus on identifying absorption lines at the galaxy's redshift. The most comprehensive of these is the COS-Halos survey (Tumlinson et al. 2011, 2013; Werk et al. 2012, 2014) which includes absorption lines of H I, O VI, N V and several lower ionization species of C, N, and Si within the CGM of 44 galaxies with stellar masses of $10 \leq \log(M_*/M_\odot) \leq 11$ along 33 AGN sight lines. This survey is complemented by COS-Dwarfs (Bordoloi et al. 2014), which focused on C IV within the CGM of galaxies with $M_* < 10^{10}$ $M_\odot$. Other surveys of the CGM include Prochaska et al. (2011), Stocke et al. (2013), and Keeney et al. (2017).

The presence of ions with both low (C II, S II) and high (O VI, N V) ionization energies requires the CGM to have a multi-phase thermal structure analogous to that of the IGM. Ionization modeling of the H I and low ion absorption lines indicates that they trace cool ($T \approx 10^4$ K) photoionized gas (Werk et al. 2014). The ionization state of the intermediate temperature gas traced by O VI and N V is more controversial, with debate as to whether the observations can be matched with models incorporating only collisional ionization equilibrium and photoionization by the UVB (Cen & Safarzadeh 2016), or if local ionizing radiation and non-equilibrium effects are needed (Werk et al. 2016). In addition, X-ray detections of O VII and O VIII absorption in the CGM of the Milky Way (Nicastro et al. 2002; Gupta et al. 2012) indicate that a hot volume-filling phase is likely present in the CGM as well.

1.4 Flows Between the Baryon Reservoirs

The universe is not a static place, and much of its evolution is driven by the flow of baryons between their various reservoirs. Many galaxies in the low-redshift universe have molecular gas depletion timescales of $\sim 10^9$ yr (e.g., Genzel et al. 2015; Saintonge et al. 2016), so ongoing star formation must be sustained by inflowing gas. Both one-dimensional (Dekel & Birnboim 2006) and cosmological simulations (Kereš et al. 2005) indicate that the efficiency with which galaxies accrete gas is a function of dark matter halo mass (M_{vir}). Gas accreted by galaxies with $M_{vir} \lesssim 10^{11.4}$ $M_\odot$ remains cool ($T < 10^5$ K) as it passes through the CGM, allowing efficient accretion. In higher mass halos, gas is shock-heated to the halo virial temperature as it enters the CGM, significantly

increasing the time required for it to cool and accrete onto the galaxy. Depending on the density and temperature of the CGM, the cooling time may be longer than the Hubble time, effectively stopping further gas accretion. The transition between these "cold" and "hot" accretion modes may be at least partly responsible for the quenching of star formation that transforms active star-forming galaxies into "red and dead" ellipticals (Larson et al. 1980).

The presence of metals in the CGM and IGM requires these flows of gas to proceed in both directions. Peeples et al. (2014) found that only $\sim 20\% - 25\%$ of the metals produced in star-forming galaxies still reside in the galaxy itself, so these outflows must be significant and ongoing. Supernovae drive expanding bubbles of metal-enriched gas into the ISM. Although a single supernova bubble is a relatively local phenomenon, repeated supernovae from a burst of star formation in an OB stellar association can create a much more energetic "superbubble" that escapes the disk of the galaxy and drives a wind into the CGM (McCray & Snow 1979; Chevalier & Clegg 1985; Mac Low et al. 1989). The starburst galaxy M82 is perhaps the best local exemplar of such a galactic wind. The existence of this outflow was first noted by Lynds & Sandage (1963), and has been observed in phases including cold molecular gas (Leroy et al. 2015), warm Hα-emitting ionized gas (Westmoquette et al. 2009), and hot ($T > 10^7$ K) X-ray-emitting gas (Strickland & Heckman 2009). The ultimate fate of this gas depends on the energetics of the wind, and in particular the efficiency with which energy injected by the supernovae drive the outflow and the degree to which the wind is "mass loaded" by entraining gas from the ISM (Oppenheimer & Davé 2006; Strickland & Heckman 2009). If the wind does not reach escape velocity, then the ejected material will spend $\sim 10^9$ yr in the CGM before potentially returning to the galaxy in a "galactic fountain" (Shapiro & Field 1976). Winds that exceed the escape velocity will go on to enrich the IGM.

AGN are also believed to power significant outflows. Highly energetic, moderately relativistic ($\sim 0.1c$) outflows from the accretion disk are detected in some AGN (e.g., Tombesi et al. 2010). AGN activity is also associated with molecular outflows on kpc scales (e.g., Cicone et al. 2014), but as of yet there is no direct observational connection between the winds at these two spatial scales. Further observations are needed to understand the mechanisms driving these outflows and

the extent to which they influence the CGM and IGM.

1.5 Focus of This Thesis

The primary focus of this thesis is on using cosmological simulations to study the ionization state of the IGM and CGM. Chapters 3 and 4 focus on the UVB. As discussed previously, photoionization by the UVB is important in nearly every phase of the IGM and CGM. Despite this, there are many competing models for the UVB with various intensities, spectral energy distributions, and redshift evolutions. Chapter 3 uses comparisons between cosmological simulations with differing UVB models and the observed H I column density distributions from Tilton et al. (2012) and Danforth et al. (2016) to determine the value of $\Gamma_{\rm H}$ for $z < 0.4$. The assumption of a spatially uniform UVB is also taken for granted in many papers. Chapter 4 begins the process of questioning this assumption by exploring the effects of attenuation of the UVB due to local density variations on H I column densities at $z = 0$.

Chapter 5 focuses on the distribution and mode of ionization (collisional vs photoionization) of O VI, O VII, and O VIII in circumgalactic gas. Observational studies of the CGM such as COS-Halos have focused on material within r_{vir} of the host galaxy. However, galactic winds exceeding the escape velocity of the halo can carry enriched material out beyond the virial radius into the IGM. By examining the distribution of oxygen-enriched gas out to distances of $5r_{vir}$, we can determine the volume over which galaxies influence their environments. The distributions of O VI can be directly compared to existing studies of the CGM and IGM, while the O VII and O VIII will be useful for planning future X-ray observations of circumgalactic gas.

Chapter 2

An Overview of Cosmological Simulations

Observations of absorption lines in AGN spectra are an extremely useful tool, and have answered many questions about the distribution of baryons in the universe. However, they are limited by their fundamentally one-dimensional nature. Information about the three-dimensional nature of observed structures must be inferred from a statistical sample of many absorption systems or though analytic arguments. In addition, many important gas properties of the absorption systems, including density, temperature, metallicity, and ionization state can not be measured directly from the spectra. In systems with absorption lines from multiple ions many of these properties can be estimated through numerical modeling of the ionization balance, but for the many absorbers traced by only a single atomic species they remain unconstrained. Due to their inherently three-dimensional nature, cosmological simulations can supply much of this missing information. If analogues of a given population of absorbers can be identified in the simulation, then their spatial structures can be directly measured. Simulations also store information on the densities, temperatures, and metallicities of every piece of gas, so these quantities are immediately known for any simulated absorption system. Additional information about the absorbers, including their temporal evolution and broader physical context (such as the locations of nearby galaxies or clustering properties of absorbers) can be readily extracted.

Cosmological simulations also provide a useful tool for testing various models for physical properties in the universe. Astrophysics is not an experimental science, and there is only one universe to observe. Simulations are the closest that we can come to a laboratory for testing and

comparing various ideas. By running sets of simulations with a range of physical models, the effects of different parameters can be explored and their values constrained through comparison to observations. Chapter 3 follows this process; we run simulations with three different prescriptions for the intensity and evolution of the UVB and by comparing the simulated column density distribution of H I absorption lines to observations from Tilton et al. (2012) and Danforth et al. (2016), constrain the intensity of the low-redshift UVB. The comparison between simulation outcomes and observations of the universe is of fundamental importance. It is easy to get lost in the intricacies of a simulation, but in the end the purpose of the simulation is to learn about the properties of the real universe. This means that all measurements made in a simulation must eventually be connected to an observable quantity.

2.1 Types of Cosmological Simulation Code

In ΛCDM, dark matter interacts only via gravity (and potentially the weak nuclear force). This makes the handling of dark matter in simulations relatively straightforward. Dark matter is typically implemented as a set of collisionless particles that interact with the rest of the simulation only through gravity. The details of the gravity solver vary from code to code, but the general prescription for handling dark matter is universal. Simulating the physics of baryonic matter is significantly more difficult. Hydrodynamic processes within the baryons are more complex than gravitational interactions from both theoretical and computational standpoints. Accurate and efficient handling of shocks is particularly problematic. Several different approaches have been developed for handling the gas hydrodynamics, and the particular method chosen is the most fundamental property of any cosmological simulation code.

The first of these methods is an Eulerian (grid-based) approach, where the simulation volume is divided into a uniform grid of cells. Each cell records the bulk thermodynamic properties of the gas within it (density, temperature, velocity, etc.), and these properties are updated with each simulation time step as gas crosses the cell boundaries. Examples of modern Eulerian codes include `Enzo` (Bryan et al. 2014, used for the simulations in this thesis), FLASH (Fryxell et al. 2000),

RAMSES (Teyssier 2002), and ART (Kravtsov 1999). The primary advantage of the Eulerian approach is that the boundaries between cells provide a clear location for shocks to develop. The gas properties on both sides of the shock are well defined, and a variety of numerical techniques can be applied to solve the shock equations. Creating mock observations from Eulerian simulations is also straightforward. The gas properties at any given location within the simulation are just those of the cell containing it. Properties of larger structures such as galaxies can be easily determined by summing or averaging the properties of multiple adjacent cells.

The uniform nature of Eulerian simulations is also their biggest limitation. Matter in the universe is highly clustered, with much of the interesting physics occurring in small, dense regions. A simple grid-based approach does not provide additional resolution in these regions of interest. Most Eulerian codes address this limitation by allowing the grid to be refined by subdividing grid cells into smaller high-resolution cells. Refinement can be done either when the simulation is initialized or on-the-fly through "adapative mesh refinement" (AMR). Typically refinement is done based on density, but in principle any property of the simulation can be used to identify regions for refinement. Repeated levels of refinement can be used to obtain arbitrarily high resolutions in small regions. For example, the simulation described in Xu et al. (2013) has a (comoving) base resolution of 78.1 kpc in unrefined regions and reaches a maximum resolution of 19 pc after 12 levels of refinement. Another drawback of the Eulerian approach is that it does not naturally record the history of individual parcels of gas. When gas crosses a cell boundary, its properties are subsumed into the overall values for the cell's gas and any history of its movement is lost. Accounting for gas history requires adding massless "tracer particles" to the simulation which are advected along with the gas and record the evolution of its properties over time.

The second major paradigm for cosmological hydrodynamics is Lagrangian smoothed particle hydrodynamics (SPH). In this approach, baryons are divided up into a number of (typically equal mass) SPH particles. Each particle is characterized by its position, velocity, and either energy or entropy. SPH particles move under the influence of both gravity and pressure from neighboring particles. The volume influenced by a given particle is defined by a "smoothing kernel." Examples

of SPH codes include Gasoline (Wadsley et al. 2004) and the many versions of GADGET (Springel 2005). The greatest advantage of SPH is that it automatically adapts to variations in density. The size of a particle's smoothing kernel is typically defined to include a fixed number or mass of nearby particles. This means that the spatial resolution of the simulation is naturally higher in regions of higher density, without any need for refinement of individual particles. The Lagrangian nature of SPH also means that the history of any given gas parcel can easily be tracked by following its host SPH particle over time.

The fixed mass of SPH particles creates difficulty for following the hydrodynamics of the gas. As there are no mass flows between particles, shocks do not naturally develop in the simulation. Instead, the thermodynamic effects of shocks must be accounted for with an artificial viscosity term (e.g., Monaghan & Gingold 1983). The discrete nature of SPH particles also increases the difficulty of creating mock observations from a simulation. The fluid properties at any given point in the simulation volume are determined by averaging the properties of all SPH particles that include the location within their smoothing kernels. This means that fundamental gas properties such as density are only defined with respect to a given choice of smoothing kernel, making the interpretation of quantities measured in SPH simulations more difficulty than in the Eulerian case.

In recent years, a third method for cosmological hydrodynamics has been developed that combines the Eulerian and Lagrangian approaches. This "moving mesh" technique subdivides the simulation domain into cells as in an Eulerian scheme, but these cells are no longer constrained to be cubes and can be chosen so that each encompasses a constant gas mass. In each simulation time step, gas moves between cells under the effects of gravity and hydrodynamic forces. Subsequently, the cells themselves are redefined to trace the new gas structure in the simulation. Simulations with a moving mesh possess the dynamic resolution of SPH simulations while maintaining the accurate shock capturing of Eulerian schemes. The tradeoff is an increased computational cost associated with repartitioning the simulation volume at every time step. In addition, care must be taken to ensure that individual cells do not become too highly deformed. A moving mesh is implemented in AREPO (Springel 2010) and a related technique is used in GIZMO (Hopkins 2015).

2.2 Subgrid Physics

The fundamental challenge for cosmological simulations is one of dynamic range. Galaxies and AGN, particularly at the highest luminosities, are separated by distances of many Mpc. Obtaining useful statistical samples of these objects requires simulation boxes with sizes of 10s to 100s of Mpc on a side. Meanwhile, much of the astrophysical processes in the universe take place on sub-pc scales. The later stages of star formation occur on scales of 10^{-3} pc, while the accretion disks that feed AGN have sizes of 10^{-3} – 10^{-2} pc. Current computational resources are not able to simulate this full range of scales simultaneously. Instead, most of the astrophysical processes in a simulation are implemented through semi-analytic "subgrid physics" algorithms. As both scientific knowledge and computational power increase, new subgrid physics implementations are constantly being developed and refined. The rest of this section summarizes some of the primary subgrid physics modules used in modern cosmological simulations.

2.2.1 Star Formation

Stars are typically implemented in simulations as collisionless star particles, which are treated in the same way as dark matter particles by the gravitational solver. Each star particle represents an entire coeval stellar population. Although the details of different star formation prescriptions differ (e.g., Cen & Ostriker 1992; Springel & Hernquist 2003; Schaye & Dalla Vecchia 2008), they share several general characteristics: a minimum gas density or pressure for star formation, a maximum temperature, and an efficiency parameter used to scale the star formation rate per dynamical time to match observations (e.g., Kennicutt 1998). The value of the efficiency parameter is highly dependent on resolution. In particular, with sufficiently high resolution and stellar feedback included, a local star formation efficiency of 100% per free fall time can reproduce observations on galactic scales (Hopkins et al. 2014). This means that the observed efficiency of star formation arises naturally from a balance between the collapse of molecular clouds and their disruption by stellar feedback.

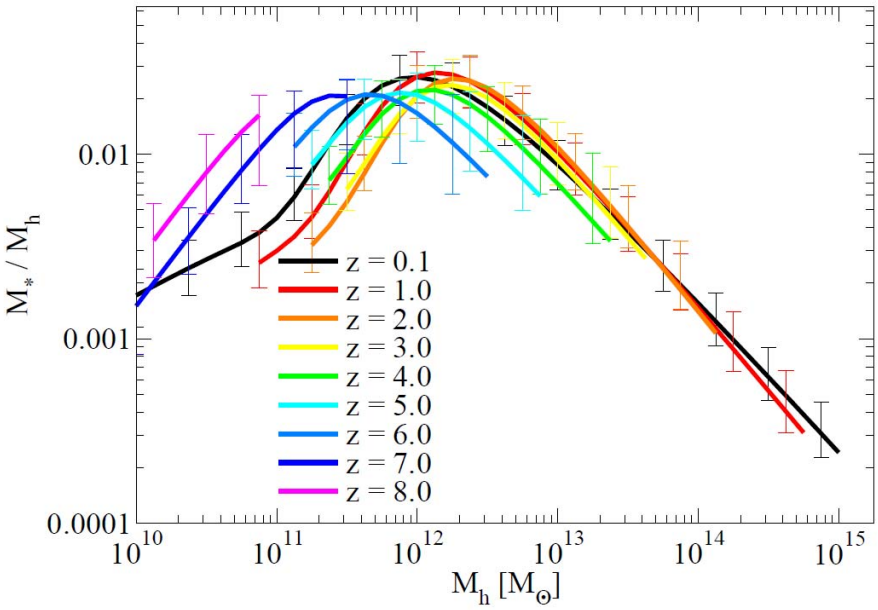

Figure 2.1 Stellar mass fraction of galaxies as a function of halo mass and redshift from Behroozi et al. (2013a). The efficiency of star formation peaks for halo masses of $\sim 10^{12}\ M_{\odot}$. Feedback from supernovae and AGN are required to match the star formation efficiencies of low and high mass halos, respectively.

2.2.2 Stellar Feedback

Star formation alone can not match observations of galaxy stellar masses. The efficiency of star formation peaks for dark matter halos with masses of $\sim 10^{12}\ M_{\odot}$, as shown in Figure 2.1. Appropriate tuning of the star formation prescription can match this peak efficiency, but can not account for the decreasing efficiency of star formation in low and high mass halos. Feedback from supernovae is needed to reduce the efficiency of star formation in low mass halos, as well as to explain the metal enrichment of the IGM and CGM.

Supernova feedback takes the form of gas, metals, and energy returned from star particles to the surrounding gas. The gas and metal feedback is straightforward, with material deposited in nearby grid cells or SPH particles in an amount depending on the star particle mass, stellar initial mass function, and observationally determined supernova metal yields. The injection of supernova energy into the simulation is more problematic. Most simulations cannot resolve the

initial adiabatic expansion of a supernova and must instead tune the energy injection to match observations. In addition, this energy can be injected in different forms, including thermal energy (Smith et al. 2011; Dalla Vecchia & Schaye 2012) or mechanical energy of a wind (Springel & Hernquist 2003; Oppenheimer & Davé 2006).

If supernova feedback is injected naively, the newly enriched dense gas can rapidly cool and form additional stars before the feedback is able to drive an outflow. This over-cooling problem (Balogh et al. 2001) can lead to a runaway cycle of star formation, feedback, and rapid cooling that leads to unrealistically high star formation rates. Many different approaches have been taken to avoid this problem, including injecting feedback over a larger volume (Smith et al. 2011), imposing a minimum temperature on post-feedback gas (Dalla Vecchia & Schaye 2012), or temporarily decoupling particles affected by feedback from the simulation's hydrodynamics solver (Springel & Hernquist 2003).

2.2.3 AGN Feedback

While stellar feedback can account for the decrease in star formation efficiency in halos with masses below 10^{12} $M_{\odot}$, the escape velocities of higher mass halos are too large for supernovae to drive significant outflows. Outflows driven by AGN are needed to explain the reduced star formation efficiency in these high mass halos. The initial formation of supermassive black holes (SMBHs) within galaxies is poorly understood (e.g., Volonteri 2010), but SMBHs are believed to be a universal feature of dark matter halos at low redshift. Cosmological simulations typically avoid the problem of SMBH formation by placing a seed SMBH of fixed mass in any dark matter halo that exceeds a prescribed mass threshold (e.g., Di Matteo et al. 2008). Once seeded, AGN grow by accreting material from the surrounding gas, with a rate that is typically based on the Bondi-Hoyle-Lyttleton accretion rate (Hoyle & Lyttleton 1939; Bondi & Hoyle 1944; Bondi 1952). A fraction of the accretion energy, scaled by an efficiency parameter, is then injected into the gas and deposited as either thermal (Di Matteo et al. 2008) or mechanical (Sijacki et al. 2007) feedback.

2.2.4 Atomic Chemistry

The thermal and ionization state of gas in cosmological simulations is determined by a number of related atomic processes. Most simulation codes directly trace the chemistry of hydrogen and helium, potentially along with H_2, using a non-equilibrium chemical reaction network (e.g., Anninos et al. 1997). In metal-enriched gas, additional cooling comes from radiative processes (recombination and de-excitation) in the metals. Fully following a non-equilibrium chemical network for metals adds significant computational expense to a simulation, so metal cooling is typically implemented assuming ionization equilibrium and solar metal abundances, with rates obtained from pre-compiled tables of CLOUDY ionization models (Smith et al. 2008). However, some recent simulations have directly tracked metal abundance ratios from supernovae in the simulation (Hopkins et al. 2014) or implemented full non-equilibrium metal chemistry (Oppenheimer et al. 2016). The metagalactic UV background also contributes to heating and ionization, and simulations must couple their choice of UVB to the rest of the chemistry modules. A few simulations also include the effects of local ionizing radiation from star particles (Hopkins et al. 2014).

2.3 Creating Mock Observations

To analyze cosmological simulations, data must be extracted in a way that allows for direct comparison to observations. This is often done by creating data products that mimic the results of observational studies. Two sets of mock observables that are particularly import for studies of the IGM and CGM are galaxy catalogs and AGN absorption spectra. Galaxies are identified in simulation outputs by the clustering of dark matter particles. Halo finders construct halos from groups of dark matter particles that are clustered in space (Davis et al. 1985; Eisenstein & Hut 1998) or in six-dimensional phase space (Behroozi et al. 2013b). Dark matter halos identified in this way may be further divided into subhalos (e.g., Springel et al. 2001) that may host either central or satellite galaxies. The halos are characterized by properties including location, velocity, virial mass, and virial radius. Additional galaxy properties can be determined by analyzing the gas

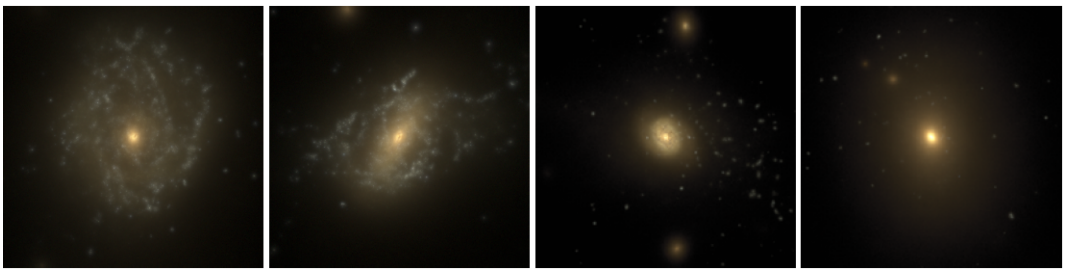

Figure 2.2 Mock SDSS images of galaxies from Oppenheimer et al. (2016). The images were created with the SKIRT radiative transfer code (Camps & Baes 2015).

and stars found within the halo. Each star particle in a halo represents a stellar population with a defined age, mass, and metallicity. When combined with a stellar population synthesis model such as Starburst99 (Leitherer et al. 1999) and dust radiative transfer (e.g., Baes et al. 2011; Camps & Baes 2015), mock images can be created from the galaxies (Figure 2.2).

Creating mock AGN observations is a relatively simple process. The AGN sight line is represented by a ray through the simulation volume, which may be either randomly placed or oriented to intercept a specific structure of interest. Gas properties along the sight line are either taken directly from grid cells intersecting the ray (for Eulerian codes) or interpolated from neighboring gas particles using a smoothing kernel (for SPH). Additional information such as the locations and properties of nearby dark matter halos can also be attached to the AGN sight line. Absorption lines can be identified by either directly summing column densities from a contiguous segment of the sight line, or by first creating a synthetic spectrum and then applying standard spectral fitting routines. The advantage of the first method is that the absorbers identified can be directly tied to the simulation volume where they originate, while the second is more closely aligned with observational methods. The column densities derived from the two methods are in good agreement. For a full comparison of the two methods, see Egan et al. (2014).

Chapter 3

The Metagalactic Ionizing Background: A Crisis in UV Photon Production or Incorrect Galaxy Escape Fractions?

The contents of this chapter were published in the *The Astrophysical Journal* as Shull, J. M., Moloney, J., Danforth, C. W., & Tilton, E. M. 2015, ApJ, 811, 3.

3.1 Abstract

Recent suggestions of a "photon underproduction crisis" (Kollmeier et al. 2014) have generated concern over the intensity and spectrum of ionizing photons in the metagalactic ultraviolet background (UVB). The balance of hydrogen photoionization and recombination determines the opacity of the low-redshift intergalactic medium (IGM). We calibrate the hydrogen photoionization rate ($\Gamma_{\rm H}$) by comparing *Hubble Space Telescope* spectroscopic surveys of the low-redshift column density distribution of H I absorbers and the observed ($z < 0.4$) mean Lyα flux decrement, $D_A = (0.014)(1+z)^{2.2}$, to new cosmological simulations. The distribution, $f(N_{\rm HI}, z) \equiv d^2\mathcal{N}/d(\log N_{\rm HI})dz$, is consistent with an increased UVB that includes contributions from both quasars and galaxies. Our recommended fit, $\Gamma_{\rm H}(z) = (4.6 \times 10^{-14}\ {\rm s}^{-1})(1+z)^{4.4}$ for $0 < z < 0.47$, corresponds to unidirectional LyC photon flux $\Phi_0 \approx 5700\ {\rm cm}^{-2}\ {\rm s}^{-1}$ at $z = 0$. This flux agrees with observed IGM metal ionization ratios (C III/C IV and Si III/Si IV) and suggests a 25-30% contribution of Lyα absorbers to the cosmic baryon inventory. The primary uncertainties in the low-redshift UVB are the contribution from massive stars in galaxies and the LyC escape fraction ($f_{\rm esc}$), a highly directional quantity that is difficult to constrain statistically. We suggest

that both quasars and low-mass starburst galaxies are important contributors to the ionizing UVB at $z < 2$. Their additional ionizing flux would resolve any crisis in photon underproduction.

3.2 Introduction

One the most important but poorest known parameters in studies of the intergalactic medium (IGM) and circumgalactic medium (CGM) is the intensity of the metagalactic ionizing ultraviolet background (UVB). This uncertainty is not surprising, considering the strong absorption of extreme ultraviolet (EUV) photons at wavelengths $\lambda \leq 911.753$ Å by the interstellar medium (ISM). Lacking direct measurements of the metagalactic radiation field in the Lyman continuum (LyC), astronomers rely on indirect probes of photoionizing radiation and theoretical estimates[1] based on the presumed ionizing sources and cosmological radiative transfer. An accurate characterization of this UVB is necessary for modeling the thermal and ionization conditions (Bolton et al. 2014; Boera et al. 2014) of the IGM and CGM, for a census of IGM baryon content (Shull et al. 2012b), and for the ionization corrections needed to derive metallicities (Shull et al. 2014; Werk et al. 2014). For photoionization of hydrogen, helium, and many spectroscopically accessible ions of heavy elements (C, N, O, Ne, Mg, Si, S, Fe) the most important spectral range extends from the hydrogen Lyman edge (energies $E \geq 13.6$ eV) through the He II continuum ($E \geq 54.4$ eV) and into the extreme ultraviolet (EUV) and soft X-ray (100-1000 eV).

The claim of a "photon underproduction crisis" (Kollmeier et al. 2014, hereafter denoted K14) generated considerable anxiety in the extragalactic astronomy community and prompted a re-examination of the assumptions in modeling the EUV background at low redshift. These authors compared predictions from smoothed-particle hydrodynamic (SPH) simulations to observed properties of low-redshift H I (Lyα) absorbers. The balance of hydrogen photoionization and radiative recombination rates sets the opacity of the low-redshift IGM, which can be measured

[1] UVB models include calculations by Haardt & Madau (1996, 2001, 2012), denoted HM96, HM01 and HM12, Shull et al. (1999), and Faucher-Giguère et al. (2009). HM05 refers to the higher-flux spectrum in a 2005 August update to the Haardt & Madau (2001) "Quasars+Galaxies" spectra, provided for inclusion in the photoionization code Cloudy. The hydrogen photoionization rates, $\Gamma_{\rm H}$, in these models vary by up to a factor of six (see Table 3.1).

from the distribution of Lyα absorbers in redshift (z) and H I column density, $N_{\rm HI}$ (cm^{-2}). This allows one to infer the unidirectional ionizing photon flux Φ_0 (cm^{-2} s^{-1}) and specific intensity I_ν (erg cm^{-2} s^{-1} Hz^{-1} sr^{-1}) of LyC radiation. K14 found that the hydrogen photoionization rate ($\Gamma_{\rm H}$) required to match their simulated distribution of H I absorbers was *five* times larger than the value predicted in a recent calculation of the UVB by HM12. They found better agreement with previous estimates of a higher UVB (Shull et al. 1999; HM01) that included significant contributions from galaxies. A large part of the UVB discrepancy can be traced to the anomalously low values at $z < 2$ of the LyC escape fraction, $f_{\rm esc} = (1.8 \times 10^{-4})(1+z)^{3.4}$, adopted by HM12 for galaxies.

In this paper, we undertake a careful examination of this UVB discrepancy, comparing observations of low-z Lyα absorber to new cosmological simulations[2] . Differences among previous theoretical estimates for the UVB may arise from modeling of the evolution of sources of EUV radiation from galaxies and quasars. We use H I data from our recent surveys of low-redshift Lyα absorbers with UV spectrographs on the *Hubble Space Telescope* (*HST*): the STIS (Space Telescope Imaging Spectrograph) survey of 746 Lyα absorbers (Tilton et al. 2012) and the COS (Cosmic Origins Spectrograph) survey of over 2600 Lyα absorbers (Danforth et al. 2016). These surveys give consistent results for the bivariate distribution, $f(N_{\rm HI}, z) \equiv d^2\mathcal{N}/d(\log N_{\rm HI})dz$, of absorbers in redshift ($z \leq 0.47$) and H I column density ($12.5 \leq \log N_{\rm HI} \leq 15.5$).

In Section 3.3, we describe current estimates of the UVB and low-redshift hydrogen photoionization rates and compare our *HST* surveys of intergalactic H I column densities with new grid-code simulations of the IGM. We calibrate the UVB through its influence on the distribution of H I column densities and the flux decrement (D_A) from Lyα line blanketing. In Section 3.4, we justify boosting $\Gamma_{\rm H}$ by a factor of 2–3 above HM12 values, together with other parameters that characterize the UVB: the specific intensity I_0 (erg cm^{-2} s^{-1} Hz^{-1} sr^{-1}) at the Lyman limit and the integrated LyC photon flux Φ_0 (cm^{-2} s^{-1}). For $0 \leq z \leq 0.47$, our revised ionization rate is $\Gamma_{\rm H} \approx (4.6 \times 10^{-14}$ s$^{-1})(1+z)^{4.4}$. At $z = 0$, this corresponds to $\Phi_0 \approx 5700$ cm^{-2} s^{-1} and

[2] Our simulations are made with the N-body hydrodynamic grid code `Enzo` (http://enzo-project.org). For an overview of the code see Bryan et al. (2014). Our previous applications of `Enzo` to IGM astrophysics appear in Smith et al. (2011); Shull et al. (2012a,b).

$I_0 = 1.7 \times 10^{-23}$ erg cm^{-2} s^{-1} Hz^{-1} sr^{-1}. These parameters are in agreement with photoionization modeling in our recent IGM survey (Shull et al. 2014) of metal-ion ratios (C III/C IV and Si III/Si IV). This increase in the UVB is comparable to previous calculations (Shull et al. 1999; HM01, HM05) and likely arises from imprecise modeling of sources of EUV radiation (galaxies and quasars). The larger UVB would be consistent with an increased contribution of galaxies with LyC escape fractions, $f_{\rm esc} \approx 0.05$ at $z < 2$, in contrast to the very low values $f_{\rm esc} < 10^{-3}$ adopted by HM12. A recent analysis (Khaire & Srianand 2015) of the effects of a revised QSO luminosity function (Croom et al. 2009; Palanque-Delabrouille et al. 2013) increased the low-redshift UVB by a factor of two. Both of these results suggest that the UVB extrapolated to low redshift was under-estimated by HM12 by a factor of approximately 2–3.

3.3 Constraining the UV Background

3.3.1 Definitions and Measurements of the Ionizing Radiation Field

For an isotropic radiation field of specific intensity I_ν, the normally incident *photon flux* per frequency is $(\pi I_\nu / h\nu)$ into an angle-averaged, forward-directed effective solid angle of π steradians. The isotropic photon flux striking an atom or ion is $4\pi(I_\nu/h\nu)$, and the hydrogen photoionization rate follows by integrating this photon flux times the photoionization cross section over frequency from threshold (ν_0) to ∞.

$$\Gamma_{\rm H} = \int_{\nu_0}^{\infty} \frac{4\pi\, I_\nu}{h\nu} \sigma_\nu \, d\nu \approx \frac{4\pi I_0 \sigma_0}{h(\alpha+3)} \ . \tag{3.1}$$

Here, we approximate the frequency dependence of specific intensity and photoionization cross section by power laws, $I_\nu = I_0(\nu/\nu_0)^{-\alpha}$ and $\sigma_\nu = \sigma_0(\nu/\nu_0)^{-3}$, where $\sigma_0 = 6.30 \times 10^{-18}$ cm^2 and $\alpha \approx 1.4$ for AGN (Shull et al. 2012c; Stevans et al. 2014). The integrated unidirectional flux of ionizing photons is then

$$\Phi_0 = \int_{\nu_0}^{\infty} \frac{\pi I_\nu}{h\nu} \, d\nu = \frac{\pi I_0}{h\alpha} \ , \tag{3.2}$$

Table 3.1. Hydrogen Photoionization Rates

Model Reference	$\Gamma_{\rm H}(z=0)$	$\Gamma_{\rm H}(z=0.25)$
Haardt & Madau (1996)	4.14×10^{-14}	8.63×10^{-14}
Shull et al. (1999)	6.3×10^{-14}	15×10^{-14}
Haardt & Madau (2001)	10.3×10^{-14}	20.6×10^{-14}
Haardt & Madau (2005)	13.5×10^{-14}	29.1×10^{-14}
Haardt & Madau (2012)	2.28×10^{-14}	5.89×10^{-14}
Faucher-Giguère et al. (2009)	3.84×10^{-14}	7.28×10^{-14}
Shull et al. (2015)	4.6×10^{-14}	12×10^{-14}

Note. — Hydrogen photoionization rates $\Gamma_{\rm H}$ ($\rm s^{-1}$) computed at redshifts $z=0$ and $z=0.25$ by various theoretical models.

which is related to the density of hydrogen-ionizing photons by $\Phi_0 = n_\gamma(c/4)$ for an isotropic radiation field. We then have the relations among parameters:

$$\Gamma_{\rm H} = 4\sigma_0\Phi_0\left(\frac{\alpha}{\alpha+3}\right) = (8.06\times10^{-14}\ {\rm s^{-1}})\Phi_4 \tag{3.3}$$

$$\Gamma_{\rm H} = \frac{4\pi I_0\sigma_0}{h(\alpha+3)} = (2.71\times10^{-14}\ {\rm s^{-1}})I_{-23}\ , \tag{3.4}$$

where we normalize the incident flux of ionizing photons and specific intensity to characteristic values, $\Phi_0 = (10^4\ {\rm cm^{-2}\,s^{-1}})\Phi_4$ and $I_0 = (10^{-23}\ {\rm erg\ cm^{-2}\ s^{-1}\ Hz^{-1}\ sr^{-1}})I_{-23}$ at the hydrogen Lyman limit ($h\nu_0 = 13.60$ eV). In an *HST*/COS survey of IGM metallicity at $z \le 0.4$, Shull et al. (2014) found that $\Phi_4 \approx 1$ and $I_{-23} \approx 3$ gave reasonable fits to the observed ratios of adjacent ionization states of carbon and silicon, (Si III/Si IV) $= 0.67^{+0.35}_{-0.19}$, (C III/C IV) $= 0.70^{+0.43}_{-0.20}$, and their sum, $(\Omega_{\rm CIII}+\Omega_{\rm CIV})/(\Omega_{\rm SiIII}+\Omega_{\rm SiIV}) = 4.9^{+2.2}_{-1.1}$.

Over the past 20 years, numerous papers have estimated the ionizing background and photoionization rate. Table 3.1 lists $\Gamma_{\rm H}$ for several models, with values at $z=0$ ranging from $(2.28-13.5)\times10^{-14}$ $\rm s^{-1}$. The HM12 rate, $\Gamma_{\rm H} = 2.28\times10^{-14}$ $\rm s^{-1}$, corresponds to a one-sided ionizing flux $\Phi_0 = [\Gamma_{\rm H}(\alpha+3)/4\sigma_0\,\alpha] \approx 2630$ $\rm cm^{-2}$ $\rm s^{-1}$ and specific intensity $I_{-23} \approx 0.823$ for the radio-quiet AGN spectral index ($\alpha = 1.57$) assumed by HM12. These fluxes are lower by a factor of three compared to the $z=0$ metagalactic radiation fields from AGN and galaxies calculated by Shull et al. (1999), $I_{\rm AGN} = 1.3^{+0.8}_{-0.5}\times10^{-23}$ and $I_{\rm Gal} = 1.1^{+1.5}_{-0.7}\times10^{-23}$, respectively. Adding

these two values with propagated errors gives a total intensity and hydrogen ionization rate of $I_{\rm tot} = 2.4^{+1.7}_{-0.9} \times 10^{-23}$ erg cm^{-2} s^{-1} Hz^{-1} sr^{-1} and $\Gamma_{\rm H} = 6.0^{+4.2}_{-2.1} \times 10^{-14}$ s^{-1}. The difference between these radiation fields appears to be the contribution from galaxies. The HM12 background adopts a negligible UVB from galaxies, whereas the background models of Shull et al. (1999), HM01, and HM05 have comparable intensities from galaxies, owing to higher assumed LyC escape fractions.

3.3.2 *HST* Observations of the H I Column Density Distribution

Previous ultraviolet spectroscopic surveys of low-redshift Lyα absorbers estimated their contribution to the baryon census through the distribution of H I column densities in the diffuse Lyα forest (e.g., Penton et al. 2000, 2004; Lehner et al. 2007; Danforth & Shull 2008). Our recent *HST* surveys of the low-redshift IGM were more extensive, obtaining 746 Lyα absorbers with STIS (Tilton et al. 2012) and 2577 Lyα absorbers with COS (Danforth et al. 2016). The COS survey used the medium-resolution far-UV gratings (Green et al. 2012) with coverage between 1135–1460 Å (G130M) and 1390–1795 Å (G160M); a few spectra extended slightly outside these boundaries. Our COS survey probed 82 AGN sight lines with cumulative pathlength $\Delta z = 21.7$ with H I column densities $N_{\rm HI}$ (in cm^{-2}) between $12.5 < \log N_{\rm HI} < 17$. For this paper, we analyze a "uniform redshift-limited sample" of Lyα absorbers at $z \leq 0.47$. As discussed in these survey papers, the Lyα statistics are consistent with 24–30% of the baryons residing in the Lyα forest and partial Lyman-limit systems.

Table 3.2 summarizes the data selected from the STIS survey, with 613 Lyα absorbers at $z \leq 0.4$ over the range $12.9 \leq \log N_{\rm HI} \leq 14.7$, reprocessed as described in Danforth et al. (2016). Table 3.3 gives similar results from the COS survey at $z \leq 0.47$, with 2074 absorbers between $12.6 \leq \log N_{\rm HI} \leq 15.2$. For each bin in $\log N_{\rm HI}$, we list the number of absorbers ($\mathcal{N}_{\rm abs}$) and effective redshift pathlength ($\Delta z_{\rm eff}$) over which our Lyα survey is sensitive. From these data, we derive the bivariate distribution, $d^2\mathcal{N}/d(\log N_{\rm HI})dz$, of absorbers in H I column density and redshift by dividing $\mathcal{N}_{\rm abs}$ by $\Delta z_{\rm eff}$ and $\Delta \log N_{\rm HI} = 0.2$. An accurate calculation of this distribution function

Table 3.2. Column Density Distribution (STIS Survey)

$\langle \log N_{\rm HI} \rangle$	Range in $\log N_{\rm HI}$	$\mathcal{N}_{\rm abs}$	$\Delta z_{\rm eff}$	$f(N_{\rm HI}, z)$
13.0	(12.9–13.1)	115	4.637	124^{+13}_{-13}
13.2	(13.1–13.3)	115	5.003	115^{+11}_{-11}
13.4	(13.3–13.5)	106	5.216	102^{+10}_{-10}
13.6	(13.5–13.7)	75	5.327	70^{+9}_{-8}
13.8	(13.7–13.9)	73	5.341	68^{+9}_{-8}
14.0	(13.9–14.1)	50	5.360	47^{+8}_{-7}
14.2	(14.1–14.3)	35	5.379	33^{+6}_{-5}
14.4	(14.3–14.5)	26	5.382	24^{+6}_{-5}
14.6	(14.5–14.7)	18	5.382	17^{+5}_{-4}

Note. — For 613 low-redshift Lyα absorbers taken from *HST*/STIS survey (Tilton et al. 2012), the columns show: (1) mean column density ($N_{\rm HI}$ in cm^{-2}) with bin width $\Delta \log N_{\rm HI} = 0.2$; (2) bin range in $\log N_{\rm HI}$; (3) number of Lyα absorbers ($\mathcal{N}_{\rm abs}$) in bin; (4) total redshift pathlength $\Delta z_{\rm eff}$ at each $N_{\rm HI}$; (4) bivariate distribution of absorbers in column density and redshift, $f(N_{\rm HI}, z) \equiv d^2\mathcal{N}/d(\log N_{\rm HI})dz$, computed as $(\mathcal{N}_{\rm abs}/0.2\,\Delta z_{\rm eff})$ and plotted in Figures 3.2–3.7.

Table 3.3. Column Density Distribution (COS Survey)

$\langle \log N_{\rm HI} \rangle$	Range in $\log N_{\rm HI}$	$\mathcal{N}_{\rm abs}$	$\Delta z_{\rm eff}$	$f(N_{\rm HI}, z)$
12.7	(12.6–12.8)	194	3.67	260^{+1000}_{-120}
12.9	(12.8–13.0)	292	9.79	150^{+80}_{-40}
13.1	(13.0–13.2)	383	16.46	120 ± 10
13.3	(13.2–13.4)	368	18.78	98 ± 5
13.5	(13.4–13.6)	267	19.23	69^{+17}_{-12}
13.7	(13.6–13.8)	146	12.03	61 ± 5
13.9	(13.8–14.0)	123	12.25	50 ± 5
14.1	(14.0–14.2)	96	12.96	37 ± 4
14.3	(14.2–14.4)	75	13.75	27^{+4}_{-3}
14.5	(14.4–14.6)	47	14.17	17^{+3}_{-2}
14.7	(14.6–14.8)	45	14.24	16^{+3}_{-2}
14.9	(14.8–15.0)	19	14.25	$6.7^{+1.9}_{-1.5}$
15.1	(15.0–15.2)	19	14.25	$6.7^{+1.9}_{-1.5}$

Note. — Statistics of low-redshift Lyα absorbers ($12.6 \leq \log N_{\rm HI} < 15.2$) taken from the *HST*/COS survey (Danforth et al. 2016) using the "uniform sub-sample" of 2074 H I absorbers. The columns show: (1) mean column density ($N_{\rm HI}$ in cm^{-2}) with bin width $\Delta \log N_{\rm HI} = 0.2$; (2) bin range in $\log N_{\rm HI}$; (3) number of Lyα absorbers ($\mathcal{N}_{\rm abs}$) in bin; (4) total redshift pathlength $\Delta z_{\rm eff}$ at each $N_{\rm HI}$; (4) bivariate distribution of absorbers in column density and redshift, $f(N_{\rm HI}, z) \equiv d^2\mathcal{N}/d(\log N_{\rm HI})dz$, computed as $(\mathcal{N}_{\rm abs}/0.2\,\Delta z_{\rm eff})$ and plotted in Figures 3.2–3.7.

requires both good absorber counting statistics and knowledge of the pathlength $\Delta z_{\rm eff}$ covered in the survey for a given column density. As in Danforth & Shull (2008), we compute $\Delta z_{\rm eff}$ corresponding to the 4σ minimum Lyα equivalent width as a function of wavelength in each spectrum. Asymmetric error bars arise from statistical uncertainties in $N_{\rm abs}$ and $\Delta z_{\rm eff}$, computed for each bin using the formalism of Gehrels (1986). At low column densities, the errors are dominated by $\Delta z_{\rm eff}$, while at high column densities the errors are dominated by the small values of $N_{\rm abs}$ in bins at $\log N_{\rm HI} \geq 14.6$.

An important effect of the IGM is the flux decrement, D_A, produced by Lyα forest line blanketing of the continuum flux. Previous measurements of D_A were reported by Kirkman et al. (2007) using low-resolution UV observations with the *HST* Faint Object Spectrograph (FOS) toward 74 AGN. Their measured decrements were fitted to a power law, $D_A(z) = (0.016)(1+z)^{1.01}$, over the range $0 < z < 1.6$ with considerable scatter. Based on our moderate-resolution HST/COS survey, Figure 3.1 shows the fraction of light removed by Lyα absorption from the continuum for $0 < z < 0.47$. These statistics were found by summing the *observed-frame* equivalent widths of all identified ($> 4\sigma$) Lyα absorbers in the Danforth et al. (2016) catalog within a given redshift range, normalized by the effective redshift pathlength probed by the survey for absorbers of that strength. The uncertainty, σ_{D_A}, is the quadratic sum of measured equivalent-width uncertainties normalized in the same manner. The errors are small at lower redshifts ($z \lesssim 0.35$) where most of the surveyed Lyα absorbers are found. However, they remain small compared to D_A even at higher redshifts where $\Delta z_{\rm eff}$ is smaller. Figure 3.1 shows our results for bins of width $\Delta z = 0.01$ and $\Delta z = 0.05$ to illustrate the variance on small scales. The scatter in D_A is significantly larger than σ_{D_A}, and cosmic variance is significant, particularly at $z > 0.35$. These fluctuations are large in the $\Delta z = 0.01$ bins, which are comparable to the mean absorber separations for the observed Lyα absorption-line frequencies $d\mathcal{N}/dz \approx 100 - 200$ for $\log N_{\rm HI} = 12.7 - 13.3$.

Figure 3.1 shows a small dip in D_A between $0.2 < z < 0.3$. This redshift band corresponds to Lyα absorbers at 1459 Å to 1580 Å, observed primarily by the COS/G160M grating (1390–1795 Å) since G130M ends at 1460 Å. The dip appears in several ranges of column density, $13 < \log N_{\rm HI} < 14$ and $14 < \log N_{\rm HI} < 15$. The first range is expected to dominate line blanketing in the Lyα forest

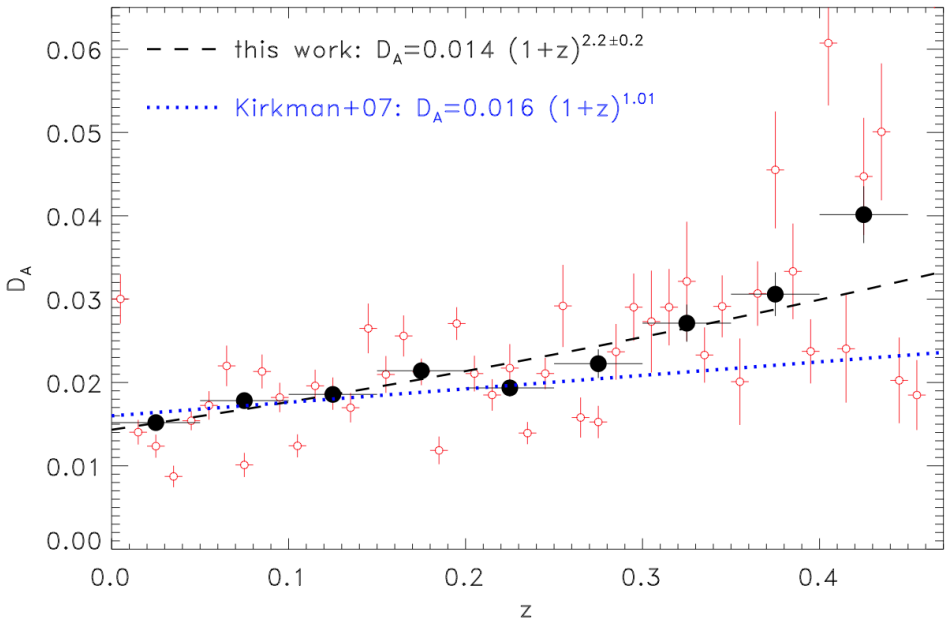

Figure 3.1 Flux decrement from the Danforth et al. (2016) low-z IGM survey with COS showing the fraction of flux removed from the continuum by Lyα absorbers for redshifts $0 < z < 0.47$. The decrement $D_A(z)$ is calculated from the normalized, summed,observed-frame equivalent widths of Lyα absorbers in a given redshift bin, divided by the effective pathlength ($\Delta z_{\rm eff}$) probed by the survey at each redshift. Red open circles show D_A in bins of width $\Delta z = 0.01$. Filled black circles show D_A in bins of width $\Delta z = 0.05$ and fitted to $D_A(z) = (0.014)(1+z)^{2.2\pm0.2}$ (dashed line). Blue dotted line shows the fit, $D_A(z) \approx (0.016)(1+z)^{1.01}$, found by Kirkman et al. (2007) in lower-resolution *HST*/FOS measurements. The small drop in D_A at $z \approx 0.2-0.3$ appears over several column-density ranges and remains when we shift the redshift bins.

for line profiles with Doppler velocity parameters $b \approx 25 - 30$ km s^{-1}. The dip also remains when we offset the redshift bins. Thus, we believe the dip to be real, although we do not have a plausible physical explanation for its presence.

We fitted the mean values of the *HST* observations with $\Delta z = 0.05$ bins to the power-law form $D_A(z) = (0.014 \pm 0.001)(1+z)^{2.2\pm0.2}$. For $z \leq 0.2$, these observations are in reasonable agreement with the lower-resolution *HST*/FOS results of Kirkman et al. (2007), although we find steeper redshift evolution. By post-processing the H I absorption-line profiles in our simulations (Sections 3.3.3 and 3.3.4) over the range $0 < z < 0.2$, we find mean decrements at $\langle z \rangle = 0.1$ of $D_A = 0.0116$, 0.0097, and 0.0332 for the HM01, HM05, and HM12 radiation fields, respectively. At $\langle z \rangle = 0.1$, these UVBs correspond to hydrogen photoionization rates $\Gamma_{\rm H} = 3.54 \times 10^{-14}$ s^{-1} (HM12), 1.38×10^{-13} s^{-1} (HM01), and 1.86×10^{-13} s^{-1} (HM05). Our simulations find that $D_A \propto \Gamma_{\rm H}^{-0.7}$. In their SPH simulations, K14 found decrements at $z \approx 0.1$ of $D_A = 0.024$ (HM01) and $D_A = 0.050$ (HM12), higher than our simulations by factors of 1.9 and 2.9, respectively. Similar offsets are seen in the distribution of H I column densities.

Our observations at $z \leq 0.47$ with STIS (Tilton et al. 2012) and COS (Danforth et al. 2016) yield consistent values for $f(N_{\rm HI}, z)$, the bivariate distribution of Lyα absorbers in column density and redshift. A least-squares fit of the COS data over the range $12.7 \leq \log N_{\rm HI} \leq 15.2$ had the form, $f(N_{\rm HI}, z) \equiv d^2\mathcal{N}/d(\log N_{\rm HI})dz \approx (167) N_{13}^{-0.65\pm0.02}$, where we define the dimensionless column density $N_{13} = [N_{\rm HI}/10^{13}\ {\rm cm}^{-2}]$. We can use this line frequency to make an analytic estimate of the Lyα line blanketing and flux decrement,

$$\begin{aligned} D_A &= \int_{N_1}^{N_2} \left(\frac{W_\lambda}{\lambda}\right) f(N,z)\, d(\log N) \\ &= \left(\frac{\pi e^2 f \lambda}{m_e c^2}\right) \left(\frac{167 \times 10^{13}\ {\rm cm}^{-2}}{2.303}\right) \int_{N_1}^{N_2} N_{13}^{-0.65}\, dN_{13}\ . \end{aligned} \tag{3.5}$$

In the last expression of Equation 3.5, we assume unsaturated Lyα lines, with equivalent widths $W_\lambda/\lambda = (\pi e^2/m_e c)(N f \lambda/c)$, where W_λ and $\lambda = 1215.67$ Å are defined in the rest-frame and $f = 0.4164$ is the Lyα oscillator strength. We adopt limits $\log N_1 = 12.5$ and $\log N_2 = 14.0$ for the integral, which we denote $I(N_1, N_2) \approx 4.49$. The estimated decrement $D_A = (0.00323) I(N_1, N_2) \approx$

0.0145, close to our observations at $z \approx 0$. Because line frequency $f(N_{\rm HI}, z) \propto (1+z)^{2.2}$ out to $z \approx 0.5$ (Danforth et al. 2016), we expect D_A to have the same dependence, as seen in Figure 3.1. This calculation shows that for the observed steep distribution of H I column densities, most of the line blanketing occurs from moderate-strength Lyα absorbers at $N_{\rm HI} \approx N_2$, beginning to saturate and appear on the flat portion of the curve of growth. Owing to line saturation, the stronger but rarer Lyα absorbers add a small amount to this estimate.

3.3.3 Cosmological Simulations of H I in the low-z IGM

Our simulations of the H I absorber distributions were run using the Eulerian N-body + hydrodynamics code `Enzo` (Bryan et al. 2014). The N-body dynamics of the dark matter particles in our simulations were calculated using a particle-mesh solver (Hockney & Eastwood 1988), and the hydrodynamic equations were solved using a direct-Eulerian piecewise parabolic method (Colella & Woodward 1984; Bryan et al. 1995) with a Harten-Lax-van Leer-Contact Riemann solver (Toro et al. 1994). Our modifications of this code and its applications to the IGM are discussed in Smith et al. (2011), where we conducted tests of convergence, examined various feedback schemes, and compared the results to IGM thermal phases, O VI absorbers, and star-formation histories using box sizes of $25h^{-1}$ Mpc and $50h^{-1}$ Mpc and grids of 256^3, 384^3, 512^3, 768^3, and 1024^3 cells. We note that the Smith et al. (2011) simulations used the HM96 background, rather than HM01 as stated in that paper[3] . This code has a substantial IGM heritage, with applications to O VI absorbers (Smith et al. 2011), the baryon census at $z < 0.4$ (Shull et al. 2012b), clumping factors and critical star-formation rates during reionization (Shull et al. 2012a), and synthetic absorption-line spectra for comparison of simulations with *HST* observations (Egan et al. 2014).

Our current simulations were initialized at a redshift $z = 99$ and run to $z = 0$, using the WMAP-9 maximum likelihood concordance values (Hinshaw et al. 2013) with $\Omega_m = 0.282$, $\Omega_\Lambda = 0.718$, $\Omega_b = 0.046$, $H_0 = 69.7$ km s^{-1} Mpc^{-1}, $\sigma_8 = 0.817$, and $n_s = 0.965$ to create the initial

[3] Because the HM96 background is 2.5 times lower than HM01, the Lyα forest was stronger in the Smith et al. (2011) simulations. However, as we discuss in Section 2.4, the HM96 background is close to the value we recommend in our current study. Consequently, our 2011 simulations are in reasonable agreement with the *HST* observations of the low-redshift Lyα forest.

conditions. The dark matter density power spectrum used the Eisenstein & Hu (1999) transfer function. Three independent realizations of the initial conditions were created in order to constrain the effects of cosmic variance due to the finite box size. Two of the realizations were created using MUSIC (Hahn & Abel 2011) with second-order Lagrangian perturbation theory. The third realization was created using the initial condition generator packaged with `Enzo`. The basic simulations discussed in this paper were run on static, uniform grids with a box size of $50h^{-1}$ comoving Mpc and 512^3 and 768^3 cells. We also analyzed a previous simulation with 1536^3 cells, produced by Britton Smith on the XSEDE supercomputer and discussed in our study of IGM clumping factors (Shull et al. 2012a), as well the ($1024^3, 50h^{-1}$ Mpc) simulations of Smith et al. (2011). Because those 1024^3 models were run with an older UVB from Haardt & Madau (1996), we chose not to compare them to our 512^3 and 768^3 runs, which used more recent backgrounds (HM01, HM05, HM12).

In view of the different predictions of our code for the distribution of low-redshift Lyα absorbers, it is appropriate to compare the resolution[4] of our grid-code simulations to the SPH simulations run by K14. With a co-moving box size of $50h^{-1}$ Mpc, our models have spatial resolutions (cell sizes) of $97.6h^{-1}$, $65.1h^{-1}$, and $32.6h^{-1}$ kpc for grids of 512^3, 768^3, and 1536^3, respectively. The corresponding dark-matter mass resolutions are $m_{\rm dm} = 6.1 \times 10^7\, h^{-1}\ M_\odot$ (512^3), $1.8 \times 10^7\, h^{-1}\ M_\odot$ (768^3), and $2.2 \times 10^6\, h^{-1}\ M_\odot$ (1536^3). For comparison, the simulations analyzed by K14 used the SPH code of Davé et al. (2010), also in a $50h^{-1}$ Mpc box with 576^3 dark-matter (and baryon) particles. The characteristic spatial resolution in their SPH method is the interparticle distance, $50h^{-1}\,{\rm Mpc}/576 \approx 86.8h^{-1}$ kpc. Under gravitational evolution, the SPH particles are concentrated in regions with baryon overdensity $\Delta_b = \rho_b/\bar{\rho}_b > 1$, and the interparticle distance is reduced by a factor of $\Delta_b^{1/3}$. Although K14 do not quote a mass resolution, their simulation ($50h^{-1}$ Mpc, 576^3) would have $m_{\rm dm} \approx 5 \times 10^7 h^{-1}\ M_\odot$, scaling from values quoted in the (512^3, $100h^{-1}$ Mpc)

[4] The original study by Davé et al. (2010) used simulations in a $48h^{-1}$ Mpc box, and most of their studies were run with 384^3 particles. To investigate effects of numerical resolution and box size, they also employed a simulation with 512^3 particles in a $96h^{-1}$ Mpc box. Contemporaneous SPH studies (Tepper-García et al. 2012) of the IGM were conducted by the "OverWhelmingly Large Simulations" (OWLS) project (Schaye et al. 2010) in a $100h^{-1}$ Mpc box with 512^3 dark-matter (and baryon) particles.

SPH calculation of Tepper-García et al. (2012). Therefore, the mass resolution in our 512^3 runs is comparable to that of K14, and our 768^3 and 1536^3 resolutions are superior. Resolution can be important when applied to the large (100-200 kpc) Lyα absorption systems observed in the low-redshift IGM.

Star particles were formed in the simulations using the subgrid physics prescription of Cen & Ostriker (1992). Star formation occurs in cells where the baryon density is greater than 100 times the critical density, the divergence of the velocity is negative, and the cooling time is less than the dynamical time. As described by Smith et al. (2011), we adopted a star formation efficiency of 10% in these cells. Feedback from star formation returns gas, matter, and energy from star particles to the ISM and IGM. Although star particles are formed instantaneously, feedback occurs gradually with an exponential decay over time. Star particles produce 90% of their feedback within four dynamical times of their creation. Of the star particles' total mass, 25% is returned as gas, with 10% of that taking the form of metals and 10^{-5} of the rest-mass energy returned as thermal feedback. The feedback is distributed evenly over 27 grid cells centered on the star particle. This scheme avoids the overcooling and subsequent runaway star formation that occurs when feedback is returned to a single cell. We analyzed this "distributed feedback" method in our previous study (Smith et al. 2011) and found that it produces better convergence and removes the over-cooling. These simulations were able to reproduce both the observed star-formation history and the number density of O VI absorbers per unit redshift over the range $0 < z < 0.4$. Many SPH studies of the IGM (Davé et al. 2010; Tepper-García et al. 2012) suppress the over-cooling by suspending the cooling or turning off the hydrodynamics for a period of time, allowing the injected energy and metals to diffuse into the surrounding gas.

The ionization states of H and He in the IGM were calculated with the non-equilibrium chemistry module in `Enzo` (Abel et al. 1997; Anninos et al. 1997). Metal cooling of the gas was computed using precompiled Cloudy[5] (Ferland et al. 2013) tables that assume ionization equilibrium for the metals and are coupled to the chemistry solver (Smith et al. 2008). Photoionization and radiative

[5] http://nublado.org

heating of the gas come from a spatially uniform metagalactic UVB. For each realization of the initial conditions, we ran three simulations that were identical except for the form of the UVB. Two simulations used analytic fits to the HM01 and HM05 backgrounds, initialized at $z = 8.9$ and reaching full strength by $z = 8$. A third background used the HM12 table implemented in the `Grackle`[6] chemistry and cooling library (Bryan et al. 2014; Kim et al. 2014) that begins at $z = 15.13$.

In order to analyze the distribution of Lyα absorbers in the simulations, we created synthetic quasar sight lines using the YT[7] analysis package (Turk et al. 2011). For each simulation box, we created 200 synthetic sight lines, each constructed from simulation outputs spanning the redshift range $0.0 \leq z \leq 0.4$. A randomly oriented ray was chosen through each output, representing the portion of the sight line beginning at the output redshift and with sufficient pathlength to cover the Δz to the next output file. These rays were then combined to create a sight line spanning the entire redshift range. We used identical random seeds for simulations sharing the same initial conditions; differences in the absorber distributions therefore directly reflect effects of different ultraviolet backgrounds. Each sight line is composed of many line elements, from the portions of the sight line passing through a single grid cell. We identified Lyα absorbers as sets of contiguous line elements with neutral hydrogen density $n_{\rm HI} \geq 10^{-12.5}$ cm^{-3}. Egan et al. (2014) compared this method of identifying absorbers to a more sophisticated method involving synthetic spectra. In their Figure 11, they showed that the resulting absorber column density distributions are in good agreement. We also analyzed a large ($1536^3, 50h^{-1}$ Mpc) simulation run by Britton Smith and discussed in Shull et al. (2012a). The light rays from this simulation were generated by Devin Silvia, and we analyzed them in the same manner.

[6] https://grackle.readthedocs.org/
[7] http://yt-project.org

3.3.4 Comparison of Simulations with HST/COS Observations

The flux decrement D_A is an imperfect metric for estimating the UVB, since measurements of the observed flux decrement depend on spectral resolution. In addition, both measurements and simulations exhibit significant variance in D_A. A more robust IGM diagnostic comes from the distribution of H I column densities. Figure 2 illustrates the observed STIS and COS distributions, $f(N_{\rm HI}, z)$, over the range $12.5 \leq \log N_{\rm HI} \leq 14.5$. The STIS and COS bins are offset by $\Delta \log N_{\rm HI} = 0.1$, using data from Tables 3.2 and 3.3. The COS survey is more extensive in both absorber numbers and column density, and its statistical accuracy is superior to that of the STIS survey. Over the overlapping range in $\log N_{\rm HI}$, the agreement is good. We over-plot values of $f(N_{\rm HI}, z)$ from our new IGM simulations ($50h^{-1}$ Mpc box and 768^3 grid cells) using three different ionizing backgrounds (HM01, HM05, HM12). As analyzed further in Section 2.5, the inferred baryon density requires ionization corrections for the neutral fraction, $n_{\rm HI}/n_H$. Appendix A suggests that the amplitude of the Lyα absorber distribution, $f(N_{\rm HI}, z)$, is proportional to $\Gamma_{\rm H}^{-1/2} T_4^{-0.363}$ for fixed baryon content (Ω_b) and temperature $T = (10^4 \text{ K}) T_4$, and it therefore provides a constraint on the UVB. In our simulations, we find that $f(N_{\rm HI}, z) \propto \Gamma_H^{-0.773}$ for absorbers in the range $13 < \log N_{\rm HI} < 14$.

Figures 3.2–3.7 illustrate the differential absorber distribution, $d^2N/d\,(\log N_{\rm HI})\,dz$, with tests of convergence, cosmic variance, box size, feedback, and redshift evolution. The simulated distributions are compared to observed distributions from *HST* surveys of Tilton et al. (2012) and Danforth et al. (2016). Figure 3.2 presents the primary results of this paper: the H I column-density distributions for three radiation fields (HM01, HM05, HM12) computed with 768^3 grids and a $50h^{-1}$ Mpc box. The lower HM12 background produces significantly more absorbers than earlier UVBs, ranging from a factor of two for absorbers between $12.5 \leq \log N_{\rm HI} \leq 12.7$ to a factor of seven for $14.3 \leq \log N_{\rm HI} \leq 14.5$. The observed distributions fall between the results for the HM01 and HM12 backgrounds, approaching the HM12 simulations for $\log N_{\rm HI} > 14.0$. This suggests that there may be less tension between the HM12 background and observations than implied by the K14 results. Figure 3.3 explores effects of cosmic variance, comparing three models with

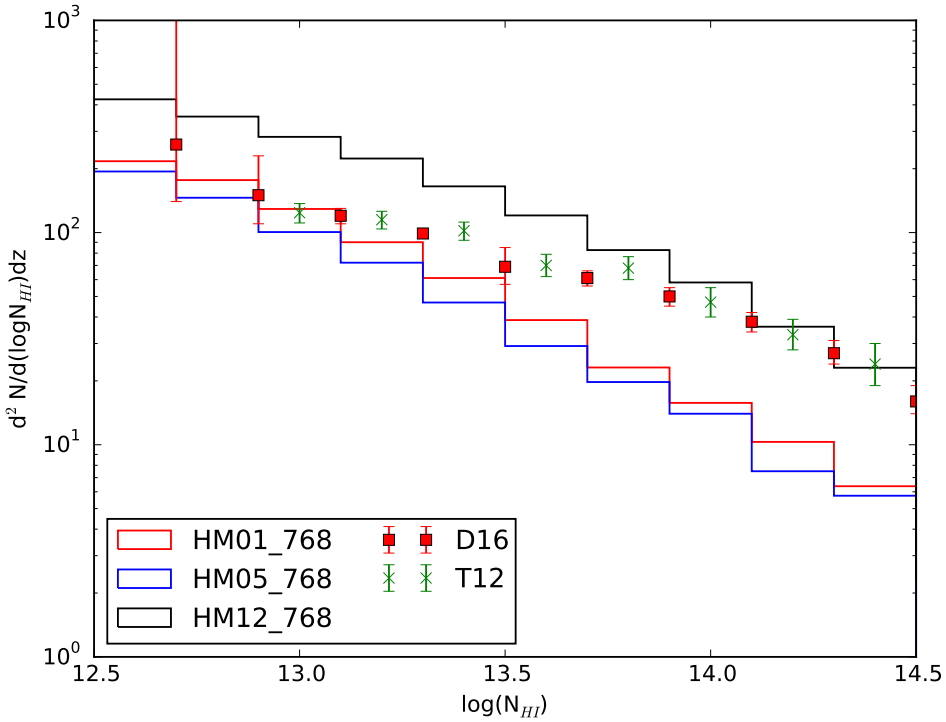

Figure 3.2 *HST* surveys of the column-density distribution of low-redshift IGM absorbers are compared to new cosmological simulations with the `Enzo` grid code (768^3 cells, $50h^{-1}$ Mpc box) with three ionizing UV backgrounds (HM01, HM05, HM12). We plot the bivariate distribution of absorbers, $f(N_{\rm HI}, z) = d^2\mathcal{N}/d(\log N_{\rm HI})dz$, in redshift and column density ($N_{\rm HI}$ in cm^{-2}) with $\Delta \log N_{\rm HI} = 0.2$ bins. Data from *HST*/COS survey (D16: Danforth et al. 2016) are shown as red squares, and data from *HST*/STIS survey (T12: Tilton et al. 2012) as green crosses. Analytic theory (Appendix A) shows that, for fixed baryon content, Lyα line frequency scales with photoionization rate and gas temperature as $\Gamma_{\rm H}^{-1/2} T_4^{-0.363}$. The HM12 simulations use a lower ionizing flux and produce a higher absorption-line density. For data with the best statistics ($13 \leq \log N_{\rm HI} \leq 14$), the observed distribution, $f(N_{\rm HI}, z) \approx (167)[N_{\rm HI}/10^{13}\ {\rm cm}^{-2}]^{-0.65}$, lies between simulations run with higher UVB (HM01 and HM05) and the lower HM12 background, except at the highest column densities. The best-fit distribution requires an ionizing background approximately 2-3 times higher than HM12, but with sufficient uncertainty that a crisis in photon production is unlikely.

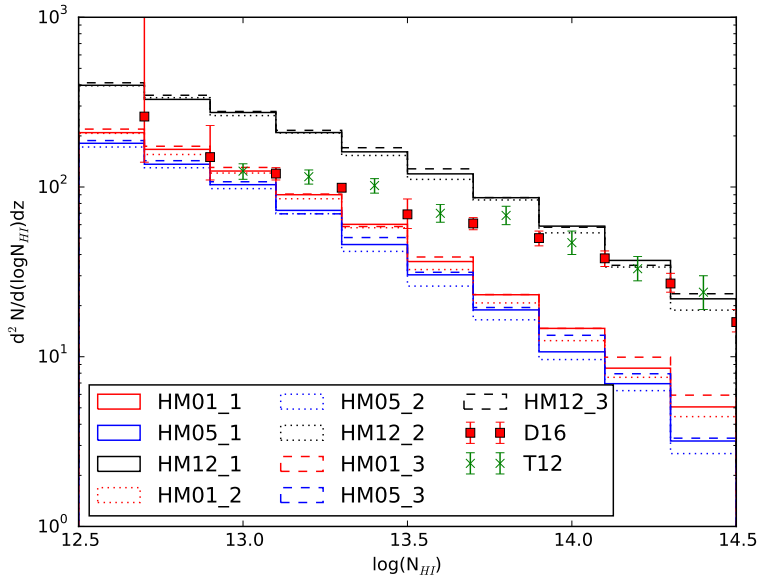

Figure 3.3 Same format as Figure 3.2. To test cosmic variance, we show three ($50h^{-1}$ Mpc, 512^3) simulations for each UVB, labeled HM01_i, HM05_i, and HM12_i (subscripts $i = 1, 2, 3$ correspond to runs with different initial conditions) and compared to *HST* survey data (D16; T12).

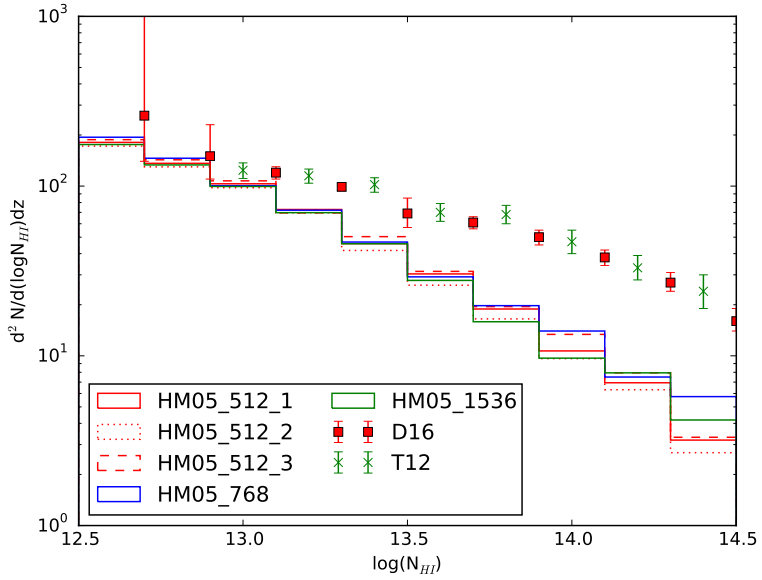

Figure 3.4 Same format as Figure 3.2. To test convergence, we compared three ($50h^{-1}$ Mpc, 512^3) simulations, labeled as HM05_i (subscripts i = 1, 2, 3) with two larger simulations: a new 768^3 simulation (HM05_768) and the 1536^3 simulation (HM05_1536) provided by Britton Smith and first presented in Shull et al. (2012a). All used the same (HM05) ionizing radiation field and are compared to *HST* spectroscopic survey data from STIS (T12) and from COS (D16).

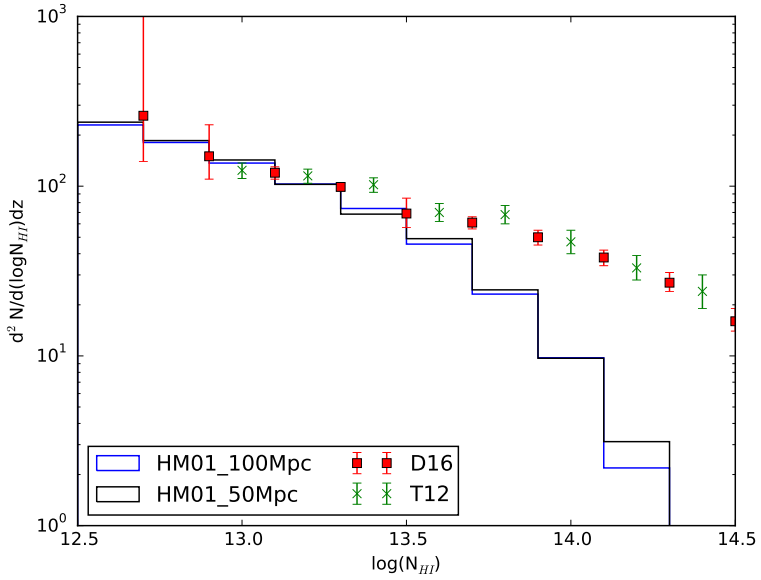

Figure 3.5 Same format as Figure 3.2. To test effects of box size, we show two simulations, one at ($100h^{-1}$ Mpc, 512^3) and another at ($50h^{-1}$ Mpc, 256^3), both using the HM01 ionizing background. Results are compared to our *HST* survey data (D16; T12). The grid cell sizes are identical ($195h^{-1}$ kpc), and the results are essentially the same for $\log N_{\rm HI} < 14$. The roll-off in simulated absorbers at $\log N_{\rm HI} > 13.7$ is an artifact of the poor resolution in these runs.

$50h^{-1}$ Mpc boxes and 512^3 grids. For each radiation field (HM01, HM05, HM12) the simulations labeled with subscripts 1 and 2 are those with the MUSIC initial conditions, and those labeled 3 use the `Enzo`-packaged initial conditions. For a fixed UVB the scatter among simulations is at the 15% level or less, indicating that variance is unlikely to play an important role. Figure 3.4 explores convergence of our simulations, comparing models with $50h^{-1}$ Mpc boxes on grids of 512^3, 768^3, and 1536^3. The differences between these models are relatively small, at the 10% level and within the expected differences arising from sample variance. Figure 3.5 investigates the potential effects of box size, which could suppress structure formation down to low redshift if the box was too small. We ran two simulations ($100h^{-1}$ Mpc, 512^3 and $50h^{-1}$ Mpc, 256^3), both using the same HM01 ionizing background. The grid cell sizes are identical ($195h^{-1}$ kpc), and the results are essentially the same for $\log N_{\rm HI} < 14$.

Figure 3.6 explores the potential influence of our feedback methods. In our 512^3 simulations, feedback has little effect on the distribution of H I column densities. We find little difference if we

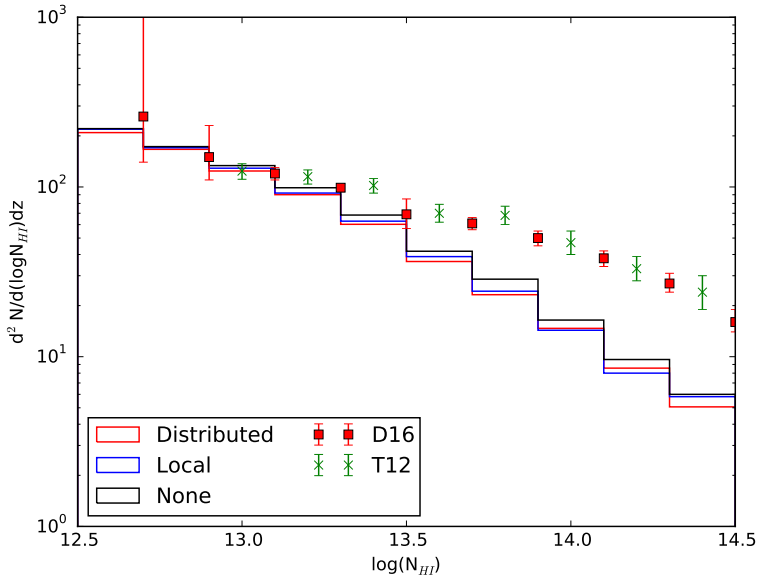

Figure 3.6 Same format as Figure 3.2. To test effects of feedback injection methods, we show three ($50h^{-1}$ Mpc, 512^3) simulations following the feedback prescriptions of Smith et al. (2011). We explored distributed feedback (into the adjoining 27 cells), local feedback (into a single cell), and no feedback from star formation. All simulations are run with the same HM01 radiation field and compared to *HST* survey data (D16; T12).

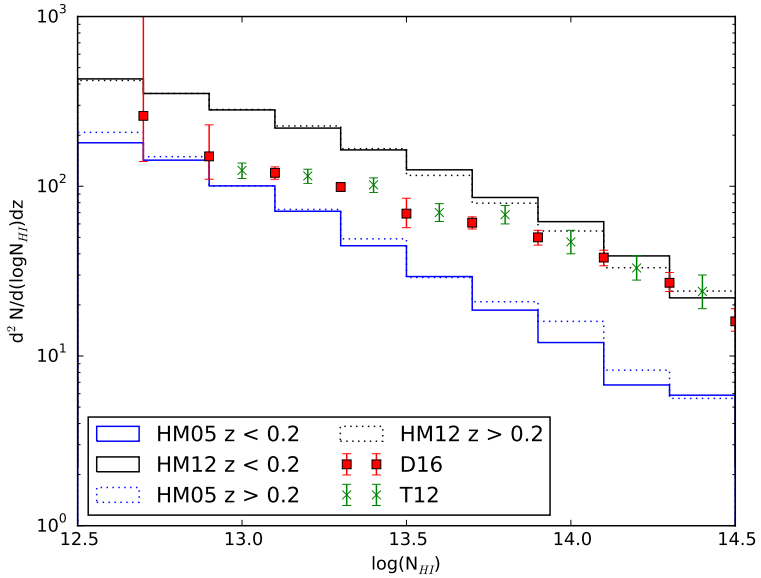

Figure 3.7 Same format as Figure 3.2. To test for redshift evolution of the low-redshift Lyα forest, we split the results into two redshift intervals ($0 < z < 0.2$ and $0.2 < z < 0.4$) for 768^3 simulations, run with both HM05 and HM12 radiation fields. Evolution in the distribution of weak Lyα absorbers in the *HST* survey (D16; T12) are small, differing by less than 5% between $0 < z < 0.4$.

inject mass, metals, and energy within a single cell, in adjacent cells, or eliminating feedback entirely. Clumpiness of the IGM on small scales can be affected by the feedback method, even though the large-scale structural parameters, (T, ρ_b) and $(\Delta_b, N_{\rm HI})$, remain nearly the same. Figure 3.7 investigates the possible effects of redshift evolution of the Lyα forest. We split the simulated results into two redshift intervals ($0 < z < 0.2$ and $0.2 < z < 0.4$) in our 768^3 simulations, all run with the HM01 radiation field. Differences between the simulated distributions are quite small and consistent with COS observations (Danforth et al. 2016), in which the weak Lyα absorbers ($\log N_{\rm HI} < 14$) exhibit little redshift evolution between $z = 0$ and $z = 0.4$.

3.3.5 Comparisons to Previous Simulations

To compare our grid-code simulations with previous SPH models, we examined two structural measures of the IGM. The first measure is the thermal-phase diagram of (T, ρ_b), the temperature vs. baryon density in the low-redshift Lyα forest. For our grid models, these diagrams were shown as Figure 19 in Smith et al. (2011) and as Figure 1 in Shull et al. (2012b). For the SPH models, we examined Figure 8 of Davé et al. (2010) and Figure 7 of Tepper-García et al. (2012). All of these diagrams are consistent with a relation $T = (5000\ {\rm K})\Delta_b^{0.6}$ where Δ_b is the baryon overdensity. A second measure is the correlation of baryon overdensity and column density $(\Delta_b, N_{\rm HI})$, typically expressed as a power-law, $\Delta_b = \Delta_0 N_{14}^{\alpha}$, where Δ_0 is the normalization at a fiducial H I column density $N_{\rm HI} = (10^{14}\,{\rm cm}^{-2})N_{14}$. These correlations vary with redshift, but typically are evaluated at $z = 0.25$. Davé et al. (2010) used $(384^3, 48h^{-1}$ Mpc) simulations with the HM01 background to derive a fit for absorbers with $T < 10^{4.5}$ K,

$$\Delta_b = (35.5 \pm 0.3) N_{14}^{0.741 \pm 0.003}\, f_\tau^{-0.741}\, 10^{-0.365z}\ . \tag{3.6}$$

Here, $f_\tau \approx 2/3$ is a renormalization factor of optical depths introduced to multiply the simulated optical depths to match the mean flux decrement D_A. Thus, at $z = 0.25$ and with $f_\tau \approx 2/3$, they found $\Delta_b = (38.9) N_{14}^{0.741}$. From $(512^3, 100h^{-1}$ Mpc) simulations with the HM01 background, Tepper-García et al. (2012) found $\Delta_b = (48.3) N_{14}^{0.786 \pm 0.010}$, with no renormalization factor f_τ. They

noted a theoretical expectation that $\Delta_b \propto N_{\rm HI}^{0.738}$ for absorbing gas in hydrostatic and photoionization equilibrium (Schaye 2001). In our ($768^3, 50h^{-1}$ Mpc) simulations, also using the HM01 radiation field, we find $\Delta_b = (36.9)N_{14}^{0.65}$ over the range $0.2 < z < 0.3$ for column densities $12.5 < \log N_{\rm HI} < 14.5$. The overdensity is calculated as a weighted average over the line elements that make up the absorber, using the column density as the weight field. We find similar normalizations, $\Delta_0 = (36.9, 38.9, 48.3)$ for the three simulations (Shull et al. 2015; Davé et al. 2010; Tepper-García et al. 2012) evaluated at $z = 0.25$ with the HM01 background.

Evidently, the structural measures of the low-z Lyα forest give similar results. The thermal-phase diagrams are essentially identical, while the differences in the $(\Delta_b, N_{\rm HI})$ correlation likely arise from different methods of identifying and characterizing H I absorbers in column density and over-density. These comparisons are complicated by the fact that Davé et al. (2010) corrected their simulated optical depths by a factor (f_τ), and Tepper-García et al. (2012) corrected for the temperature-density correlation of gas in hydrodynamic and photoionization equilibrium. The simulations also used different cosmological parameters. Tepper-García et al. (2012) adopted density fractions ($\Omega_m = 0.238$ and $\Omega_b = 0.0418$) from WMAP-3, which are lower by 15.6% and 9.1% than our WMAP-9 values ($\Omega_m = 0.282$ and $\Omega_b = 0.046$). Davé et al. (2010) adopted WMAP-7 parameters ($\Omega_m = 0.28$ and $\Omega_b = 0.046$) similar to our values. Kollmeier et al. (2014) used $\Omega_m = 0.25$ (10% lower than our value) and $\Omega_b = 0.044$ (4.3% lower). The simulations also have different resolutions: our standard simulations use (768^3, $50h^{-1}$ Mpc) while Tepper-Garcia use (512^3, $100h^{-1}$ Mpc). Given the scatter in these correlations, their redshift dependence, and the correction factors, we believe the modest differences do not warrant concern.

3.4 Summary: A Higher UV Background?

Using our recent *HST* spectroscopic surveys of intergalactic Lyα absorbers, we have characterized their distribution in H I column density and redshift. By comparing the observed distribution to new `Enzo` simulations of the low-redshift IGM, we find an ionizing background *intermediate* between the HM01 and HM12 values. As shown in Appendix A, the inferred baryon density and

absorption-line frequency depend inversely on the UVB and temperature, scaling as $\Gamma_{\rm H}^{-1/2}T^{-0.363}$. To fit the the *HST* data, we require approximately a factor of 2–3 increase in the photoionization rate above HM12, somewhat less than the factor of five suggested by K14. However, no single UVB agrees with the full distribution. Figure 3.2 suggests that a higher UVB is needed to explain the line frequency of weak absorbers ($12.7 < \log N < 13.9$), while the lower HM12 background is consistent with the distribution of stronger absorbers ($\log N_{\rm HI} > 14$). Given the uncertainties in source emissivities, cosmological radiative transfer, and galaxy LyC escape fractions, our H I results do not constitute a crisis in our understanding of the sources of the UVB.

We have explored a number of potential explanations for the differences between the H I distributions produced by various simulations and their sub-grid feedback schemes, gaseous sub-structure, and injection of mass and metals. In photoionized Lyα absorbers, the neutral hydrogen density depends on n_H^2. Consequently, the UVB and photoionization rate needed to explain the amplitude of $f(N_{\rm HI}, z)$ may be sensitive to the clumping factor, $C_H \equiv \langle n_H^2 \rangle / \langle n_H \rangle^2$. However, a detailed code comparison is beyond the scope of what we can do at this time. In the comparisons discussed earlier, we demonstrated that the integrated column densities, $N_{\rm HI}$, are less sensitive to the procedures for identifying absorbers or the feedback schemes. After investigating convergence, cosmic variance, and feedback, we conclude that the differences must arise elsewhere.

The primary influence on the distribution of H I absorbers in the Lyα forest is the ionizing radiation field. A larger UVB was also found in calculations that included contributions from both quasars and galaxies (Shull et al. 1999; Faucher-Giguère et al. 2009). The primary uncertainties in the UVB are the contribution from massive stars in galaxies (Topping & Shull 2015) and the LyC escape fraction (HM12; Benson et al. 2013), a highly directional quantity that is difficult to constrain statistically from direct observations. The parameterization adopted by HM12, $f_{\rm esc} = (1.8 \times 10^{-4})(1+z)^{3.4}$, was tuned to match observations at $z > 2.5$, but it is likely much too low at $z < 2$ where observational constraints are rare. Reliable values require direct measurements of LyC fluxes from a statistically significant sample ($N_{\rm gal} \gg 20$) of starburst galaxies to constrain the low escape fractions expected from a highly directional LyC escape geometry. For example, if

theoretical models predict $\langle f_{\rm esc} \rangle \approx 0.05$, with 5% of the LyC escaping from each side of a gaseous disk through perpendicular conical chimneys (Dove & Shull 1994), direct detections would be possible, on average, in only 5% of the observations. Constraints on $f_{\rm esc}$ will require large samples to deal with inclination bias. Such a situation is seen in direct-detection observations at $z \approx 3$ (Shapley et al. 2006; Nestor et al. 2013; Mostardi et al. 2013) and at $z \approx 0.2$ (Heckman et al. 2011) which find either large (10-40%) fractions of transmitted LyC flux or none at all. The difficulties with low-z constraints on $f_{\rm esc}$ were discussed by Shull et al. (2014) in their low-z census of IGM metal abundances and ionization ratios (C^{+3}/C^{+2} and Si^{+3}/Si^{+2}).

We therefore suggest that starburst galaxies are important contributors to the ionizing UVB at $z < 2$. Their contribution to the ionizing background would explain the observed distribution of Lyα absorbers and could resolve the discrepancy in IGM photoheating inferred from the opacity of the Lyα forest at $z < 2$ (Puchwein et al. 2015). It has also been suggested that TeV emission from blazars could add significant heat to the IGM through pair-production of high-energy electrons and positrons (Puchwein et al. 2012). We have not investigated their effects on our data, either on $D_A(z)$ or the distribution in H I column density. We summarize the main results of our study as follows:

(1) Compared to `Enzo` N-body hydrodynamical simulations of the low-z IGM with different values of the ionizing UV background, the observed distribution of Lyα forest absorbers ($z < 0.5$) lies intermediate between the HM01 and HM12 background calculations. A fit to the observations requires a factor-of-two increase in the UVB above HM12 with a recommended hydrogen ionization rate $\Gamma_{\rm H}(z) = (4.6 \times 10^{-14}\ {\rm s}^{-1})(1+z)^{4.4}$.

(2) The one-sided ionizing photon flux $\Phi_0 \approx 5700\ {\rm cm}^{-2}\ {\rm s}^{-1}$ at $z = 0$ agrees with the observed IGM metal ionization ratios, C III/C IV and Si III/Si IV (Shull et al. 2014), and suggests a 25–30% contribution of Lyα absorbers to the cosmic baryon inventory.

(3) The increased ionizing background probably requires an increase in the escape fraction of ionizing (LyC) radiation from starburst galaxies above the low values ($f_{\rm esc} < 10^{-3}$) adopted

by HM12. Ionizing photons from galaxies with $\langle f_{\rm esc} \rangle \approx 0.05$ gives results consistent with previous UVB modeling (Shull et al. 1999) that found similar contributions from AGN and starburst galaxies, with specific intensities (erg cm^{-2} s^{-1} Hz^{-1} sr^{-1}) at 13.6 eV of $I_{\rm AGN} = 1.3^{+0.8}_{-0.5} \times 10^{-23}$ and $I_{\rm Gal} = 1.1^{+1.5}_{-0.7} \times 10^{-23}$.

(4) Because LyC propagation through the ISM is expected to be highly directional, detections of escaping photons depend on galaxy orientation and will require large surveys to obtain valid statistical inferences.

Future observational and theoretical work could significantly improve our characterization of the ionizing UVB at $z < 1$. We need better accuracy of the column-density distribution of Lyα absorbers at $\log N_{\rm HI} \leq 13.0$ and $\log N_{\rm HI} \geq 14.5$. Larger surveys of IGM absorbers will allow us to measure the redshift evolution of the distribution, $d^2\mathcal{N}/d(\log N_{\rm HI})dz$, to test the expected increase in photoionization rate, $\Gamma_{\rm H}(z) \propto (1+z)^{4.4}$. The most critical future experiment will be direct measurements of LyC escape fractions from a large sample of starburst galaxies at $z < 0.4$.

Acknowledgements

This work was supported by NASA grant NNX08AC14G for COS data analysis and STScI archival grant AR-11773.01-A. We appreciate the efforts of Britton Smith and Devin Silvia in providing the light rays from unpublished `Enzo` 1536^3 models computed on the XSEDE supercomputer and used to construct column density distributions. We thank Ben Oppenheimer, Ewald Puchwein, Martin Haehnelt, Mark Giroux, and John Stocke for helpful discussions. This work utilized the *Janus* supercomputer, operated by the University of Colorado and supported by the National Science Foundation (award number CNS-0821794), the University of Colorado Boulder, the University of Colorado Denver, and the National Center for Atmospheric Research. Computations described in this work were performed using the publicly-available `Enzo` code (http://enzo-project.org), which is the product of a collaborative effort of many independent scientists from numerous institutions around the world.

Chapter 4

Local Density Effects on the Ionization of Intergalactic Hydrogen by the Metagalactic Ultraviolet Background

4.1 Abstract

Cosmological simulations typically assume a redshift-evolving but spatially uniform metagalactic ultraviolet background (UVB) to calculate photoionization and photoheating rates. Spatial non-uniformities in the true UVB arise from the discrete nature of the ionizing sources and from differential absorption of ionizing photons in the circumgalactic medium (CGM) and intergalactic medium (IGM) due to local density variations. We investigate the importance of this second effect using a simple post-processed ray-tracing routine applied to a simulation of the low-redshift ($z = 0.009$) IGM. Significant local attenuation of the UVB is rare, with a 1% or greater effect seen in only 0.15% of the line elements in our simulated light rays. UVB attenuation is strongly correlated with both H I number density and with the column density of H I absorption systems. Significant ($\geq 5\%$) increases in H I column density are seen for systems with $N_{HI} \geq 10^{15}$ cm^{-2}. These systems are associated with the CGM of nearby galaxies, with higher column densities and UVB attenuations found around more massive halos.

4.2 Introduction

At $z = 0$, only $\sim 7\%$ of baryons in the universe are found inside galaxies, with an additional $\sim 4\%$ found in galaxy clusters (Bregman 2007; Shull et al. 2012b). The remaining baryons reside in various thermal phases of the circumgalactic medium (CGM) and intergalactic medium (IGM),

but $\sim 30\%$ exist in reservoirs, such as hotter gas in galactic halos and the IGM, that have yet to be identified observationally (Shull et al. 2012b). A full accounting of the locations of the cosmic baryons, as well as the flows between the various phases, is needed to form an accurate picture of an evolving universe. Accretion of gas from the IGM through the CGM and into galaxies provides fuel for ongoing star formation, and the disruption of these inflows may lead to the "quenching" that turns actively star-forming galaxies into "red and dead" ellipticals (Larson et al. 1980). In turn, stellar winds, supernovae, and active galactic nuclei (AGN) produce outflows of metal-enriched gas that, depending on the energy of the outflow, returns material to either the CGM or the IGM (e.g., Oppenheimer & Davé 2006; Wiersma et al. 2010).

Observationally, the CGM and IGM are primarily seen through UV absorption lines in the spectra of background AGN. Although neutral hydrogen has been a minority species since cosmic reionization at $z \sim 7$, the overall abundance of hydrogen and the strength of the Lyman alpha (Lyα) and other Lyman series transitions means that H I is by far the most commonly observed ion in AGN absorption spectra. Large IGM surveys have determined the column density distribution of H I absorbers in the Lyα forest (Lehner et al. 2007; Danforth & Shull 2008; Tilton et al. 2012; Danforth et al. 2016). The Lyα forest primarily traces warm ($T < 10^5$ K) gas in filaments of the cosmic web, and accounts for $\sim 20\%$ of the cosmic baryons (Danforth et al. 2016). Hotter (10^5 – 10^6 K) gas in the warm-hot IGM traced by broad Lyα accounts for an additional $\sim 14\%$ of the baryon budget (Lehner et al. 2007; Danforth et al. 2010). Lyα is ubiquitous in the CGM, with near unity covering fraction out to impact parameters of 200 – 300 kpc (Prochaska et al. 2011; Tumlinson et al. 2013; Stocke et al. 2013) tracing $\sim 5\%$ of the cosmic baryons.

Accurate H I ion fractions are required to translate H I column densities into overall hydrogen column densities and absorber gas masses. If multiple metal ions are also present in the spectra, detailed numerical ionization modeling can be used to determine the ionization balance (e.g., Stocke et al. 2013; Werk et al. 2014). However, in the absence of metal absorption, simpler assumptions about the ionization state of the gas must be made. This typically takes the form of photoionization equilibrium from a redshift-evolving but spatially uniform mean metagalactic

ultraviolet background (UVB). Cosmological simulations also rely on an assumed UVB to provide photoionization and photoheating rates for hydrogen and helium chemistry. Numerous UVB models have been developed based on observations of the distribution of ionizing sources and semi-analytic modeling of IGM radiative transfer; the models include Shull et al. (1999), Haardt & Madau (1996, 2001, 2012), Madau & Haardt (2015), and Faucher-Giguère et al. (2009). For $z \lesssim 0.5$, a consensus has recently emerged in favor of a background with roughly twice the intensity of the Haardt & Madau (2012) background (Shull et al. 2015; Khaire & Srianand 2015; Viel et al. 2016, but see Kollmeier et al. 2014 for an alternate perspective), in line with recent observations of the AGN UV luminosity function (Croom et al. 2009; Palanque-Delabrouille et al. 2013).

Spatial variations in the UVB intensity arise from two distinct sources. The first of these is the discrete nature of the ionizing sources. The majority of ionizing photons at low redshift come from AGN (e.g., Haardt & Madau 2012). Bright AGN are extremely rare, with a comoving space density of $\sim 4 \times 10^{-6}$ Mpc^{-3} mag^{-1} for the faintest AGN in the $0.68 < z < 1.06$ sample from Palanque-Delabrouille et al. (2013). Additional ionizing photons come from O and B stars in young stellar populations. However, very little of this Lyman continuum (LyC) radiation escapes from the host galaxy into the IGM, with observations from Bridge et al. (2010) and Siana et al. (2010) indicating a mean $z \sim 1$ escape fraction of $f_{esc} \leq 0.03$ (measured relative to the escape fraction at 1500 Å), although escape fractions for individual galaxies can be higher (e.g., Leitherer et al. 2016). High-resolution zoom simulations indicate that what little LyC radiation reaches the IGM does so in a highly time-varying and anisotropic fashion (Cen & Kimm 2015; Ma et al. 2015). The required combination of large box size (to accommodate rare AGN) and high resolution (for accurate AGN accretion, star formation, and LyC escape) makes direct inclusion of discrete ionizing sources impractical in modern cosmological simulations.

The second source of spatial non-uniformity in the UVB is local density variations. Although the typical mean free path of ionizing photons is large due to the highly ionized nature of the IGM, partial Lyman-limit systems (pLLS, defined here as 10^{16} cm$^{-2} \leq N_{HI} \leq 10^{17.2}$ cm^{-2}) and Lyman-limit systems (LLS) with $N_{HI} > 10^{17.2}$ cm^{-2} create significant Lyα optical depths over

relatively short distances. LLSs are rare, with an occurrence rate of 0.37 ± 0.10 per unit redshift over the interval $0.242 \leq z \leq 1.078$ (Ribaudo et al. 2011), but their presence indicates the potential importance of local attenuation of the UVB. Both pLLSs and LLSs are associated with galaxies. Regardless of the presence of ionizing sources, the high H I column densities found in galaxies and the surrounding CGM may significantly influence the local radiation environment.

These local density effects may be important for understanding the observed column density distribution of Lyα absorbers. Although the overall normalization of the distribution is consistent with the most recent UVB models, difficulties remain in explaining the slope. The observed column density distribution is shallower than predicted for a uniform UVB, with more absorbers than expected for $N_{HI} \gtrsim 10^{13.5}$ cm^{-2} (Figure 3.2). This slope may be partially explained by an "inverse proximity effect," where higher column density absorption systems are found in denser regions which are partially shielded from ionizing UV radiation. In this paper, we quantify the magnitude of these local density effects on the H I number density of the $z = 0.009$ CGM and IGM. We post-process a large (768^3) cosmological simulation from Shull et al. (2015) using a simple ray-tracing procedure to measure the attenuation of the UVB by gas within 5 Mpc of a given location. We use the attenuated UVB photoionization rates to determine new H I number densities for individual simulation grid cells, as well as column densities for simulated absorption systems. In Section 4.3, we summarize our simulation methods and describe the ray tracing and absorber identification routines. Section 4.4 describes the principal results for increases in H I number density (n_{HI}) and absorber N_{HI} due to local UVB attenuation, as well as correlations between n_{HI}, N_{HI}, and attenuation. Section 4.5 explores the relationship between H I absorbers and nearby dark matter halos. It also describes potential changes to our ray tracing method to produce more accurate column densities for LLSs. We summarize our conclusions in Section 4.6. Throughout the paper, distances are given in comoving units unless otherwise specified.

4.3 Simulation Methods

The simulation analyzed here was first described in Shull et al. (2015) as run HM01_768. Full details of the numerical methods and subgrid physics modules used, along with convergence testing, can be found in Shull et al. (2015) and Smith et al. (2011); the most relevant aspects are summarized below. The simulation used for this analysis was produced using the Eulerian N-body + hydrodynamics code `Enzo`[1] (Bryan et al. 2014). The simulation domain encompasses a representative cosmological volume of side length $50h^{-1}$ Mpc, subdivided into a uniform 768^3 grid. This provides a spatial resolution of $65.1h^{-1}$ kpc and a dark matter particle mass of $1.8\times10^7h^{-1}M_\odot$. Shull et al. (2015) demonstrated that this resolution is sufficient to achieve a numerically converged distribution of H I column densities. The simulation was initialized at z = 99 with the WMAP-9 maximum likelihood concordance cosmological parameters (Hinshaw et al. 2013) of $\Omega_m = 0.282$, $\Omega_\Lambda = 0.718$, $\Omega_b = 0.046$, $H_0 = 69.7$ km s^{-1} Mpc^{-1}, $\sigma_8 = 0.817$, and $n_s = 0.965$ and run to z = 0.

Star particles are created in the simulation using the method described in Cen & Ostriker (1992). Stars form in grid cells with a baryon density of at least 100 times the critical density, a negative divergence of the velocity, and a gas cooling time of less than the dynamical time. The star formation efficiency within these cells is 10%. Stellar winds and supernovae return gas, metals, and energy to the surrounding cells. Although star particles are formed instantaneously within the simulation, stellar feedback occurs gradually to reflect the age distribution of a real stellar population. The rate of feedback peaks after one dynamical time and decays exponentially afterward. Over its lifetime, a star particle returns 25% of its total mass to the simulation, 10% of which is in the form of metals, as well as 10^{-5} of its rest-mass energy as thermal feedback. Feedback is distributed evenly over cube of 27 grid cells centered on the cell containing the star particle. This "distributed feedback" method is required to avoid the runaway cycle of excess cooling and subsequent star formation that can occur if all stellar feedback is deposited in a single cell (Smith et al. 2011).

[1] http://enzo-project.org

The thermal state of the gas is governed by a non-equilibrium chemistry solver for H and He (Abel et al. 1997; Anninos et al. 1997). Metal cooling rates come from precompiled CLOUDY[2] (Ferland et al. 2013) tables that assume ionization equilibrium and solar abundance ratios (Smith et al. 2008). Photoionization and radiative heating come from the spatially-uniform Haardt & Madau (2001) metagalactic UVB, which we will refer to as HM01. The UVB turns on at $z = 8.9$ and reaches full strength at $z = 8$.

4.3.1 Light Ray Creation

To conduct our analysis in a way consistent with observations, we created 2000 mock AGN sight lines from the $z = 0.009$ simulation output. Each sight line is made from a single ray traversing the simulation volume with a randomly chosen starting point and orientation. Rays were created using the YT analysis package[3] (Turk et al. 2011). Each ray has a length of $50h^{-1}$ Mpc, corresponding to a change in redshift of $\Delta z = 0.0165$; this provides a total path length of $\Delta z = 33$, comparable to the $\Delta z = 21.7$ path length covered by Danforth et al. (2016).

Each light ray is composed of a series of line elements (lixels). An individual lixel is the portion of the ray passing through a single grid cell of the simulation (Figure 4.1). Along with its location and path length, each lixel contains information on the gas properties of the cell, including density, temperature, metallicity, and the number densities of various atomic species. Each lixel also contains information on the virial masses, virial radii, and distances to nearby dark matter halos identified with the `Rockstar` halo finder (Behroozi et al. 2013b).

4.3.2 Local UVB Attenuation

The simulation uses the spatially uniform HM01 radiation background. At $z = 0.009$, this background produces a hydrogen ionization rate of $\Gamma_{HI} = 1.1 \times 10^{-13}$ s^{-1}. Our analysis requires modifying the strength of the UVB to account for the effects of local density structures. This is accomplished with a simple ray-tracing scheme, illustrated schematically in Figure 4.1. For each

[2] http://nublado.org
[3] http://yt-project.org

lixel of a light ray, a set of rays are cast from the center of the corresponding grid cell of the simulation out to a fixed distance. The rays are approximately evenly spaced in solid angle using an algorithm from Saff & Kuijlaars (1997). For each ray, the H I column density is calculated, excluding the contribution from the grid cell at the ray's origin. The column density is then converted to an optical depth using the median hydrogen photoionization cross section for the HM01 background weighted by ionization rate. This cross section is $\sigma_H = 4.3 \times 10^{-18}$ cm^2, or 68% of the cross section at the hydrogen ionization threshold. Finally, the optical depths are converted to transmission fractions and averaged to determine the new UVB intensity for the lixel.

For our analysis, we use 2000 rays per lixel with a length of 5 Mpc each. The number of rays was chosen so that an L* halo at 5 Mpc would be traced by at least one ray. The strongest effects on the UVB should come from structures located at significantly smaller distances. A galaxy located two virial radii from the lixel will cover a solid angle of $\sim \pi/4$ sr and will be traced by ~ 125 rays, which is sufficient to sample the galaxy's density profile. The precise number of rays used and their lengths do not significantly impact our results.

In grid cells with a sufficiently high H I number density, self-absorption of UVB photons within the cell becomes a significant source of attenuation. In these cells we calculate an additional self-absorption correction to the UVB intensity, which is shown in Figure 4.2. For each cell, 20 evenly spaced points are chosen along the corresponding lixel. From each point, 200 uniformly spaced rays are then cast to the grid cell boundaries. As with the external attenuation calculation, H I column densities are calculated for each ray and then converted to optical depths and UVB transmission fractions. The transmission fractions are averaged across the rays from all 20 points to determine the cell's self-absorption correction. Self-absorption corrections are calculated for all lixels with $n_{HI} \geq 5 \times 10^{-9}$ cm^{-3}, which corresponds to an optical depth of 6×10^{-3} across the $65.1h^{-1}$ kpc width of the cell.

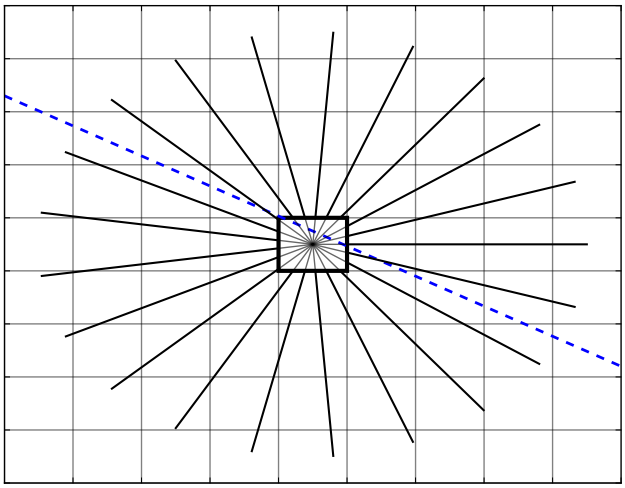

Figure 4.1 Two-dimensional schematic illustration of the ray-tracing procedure. The dashed blue line is the trajectory of the light ray, which passes through the central cell. A set of evenly spaced rays are cast from the center of this cell out to a fixed distance. The H I column density is calculated for each ray, excluding the portion of the ray within the central cell. The column densities are then converted to UVB transmission fractions and averaged to produce a single UVB intensity for the cell.

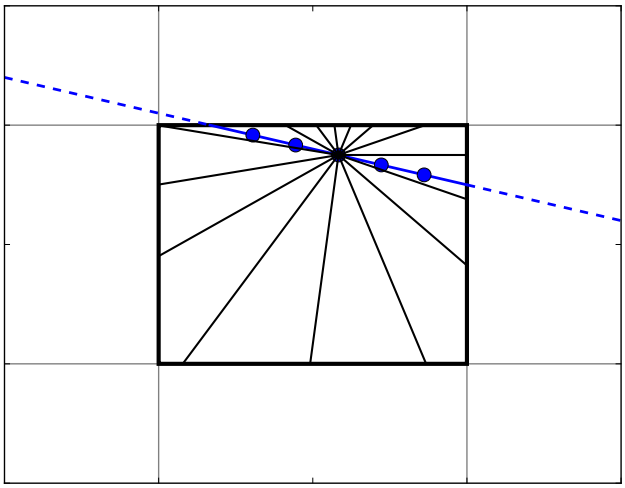

Figure 4.2 Two-dimensional schematic illustration of the self-absorption correction. The blue line is the trajectory of the light ray, with the solid segment indicating the portion of the ray within the cell where the correction is applied. A set of evenly spaced points, shown in blue, are chosen along the light ray segment. A set of rays, evenly spaced in angle, are cast from each point to the grid cell boundaries. H I optical depths are calculated for each ray, and the corresponding UVB transmission fractions are averaged across all rays and points to determine the mean UVB transmission within the cell.

4.3.3 Absorber Identification

Observations of H I in the IGM primarily take the form of absorption lines in AGN spectra. The absorption lines are then typically fit to create a catalog of column densities and line widths (e.g., Danforth et al. 2016). To create an analogous set of simulated column densities, we first need to calculate revised H I number densities for our light rays using the new UVB photoionization rates. The original H I number densities in the simulation were calculated using a non-equilibrium H and He chemistry network (Abel et al. 1997; Anninos et al. 1997). Our updated H I number density values are equilibrium values determined from a balance between collisional ionization, photoionization by the UVB, and radiative recombination, using the reaction rates from `Enzo`'s chemistry module. With an unmodified UVB intensity, the equilibrium H I number densities are in close agreement with their non-equilibrium counterparts. The median fractional difference across all lixels is 5.9×10^{-4}, with only 0.02% of the lixels having a difference of 1% or greater.

For each lixel, we calculate three values of the H I number density, corresponding to different photoionization rates. The first value uses the unmodified HM01 UVB intensity. The second H I number density uses a photoionization rate that is reduced by the external UVB attenuation to the lixel. The third value includes both external attenuation and self-absorption. This density is calculated in a two-step process. The H I number density with only external attenuation is used to determine the magnitude of the self-absorption correction, as described in the previous section. Then, a final photoionization rate is calculated using both attenuation values and is used to find the final equilibrium H I number density. For most lixels, the second and third H I number density values are identical.

Synthetic H I absorbers are identified in the light rays using the newly calculated H I number densities. An absorber is defined as a set of contiguous lixels with an H I number density above a specified threshold. We adopt a threshold of $n_{HI} = 10^{-13}$ cm^{-3} for this paper. The numbers and column densities of absorbers are not sensitive to the specific choice of threshold. For our adopted threshold, the $N_{HI} \geq 10^14$ cm^{-2} absorbers considered in our analysis contain a median of 21 lixels.

Table 4.1. Number of lixels with UVB attenuations above the specified thresholds

Model	Attenuation Threshold				
	1%	2.5%	5%	10%	20%
External Attenuation	3425	745	249	81	16
Self Absorption	86	52	28	18	11
Total Attenuation	3429	759	266	93	28

Each absorber has a column density calculated from its component lixels, as well as column-density weighted mean gas properties such as temperature and H I number density. Egan et al. (2014) showed that column densities calculated with a similar "contour method" are in good agreement with values determined from synthetic spectra. Absorbers also store information on the distances and properties of nearby dark matter halos.

4.4 Results

Mean UVB attenuations were calculated for all 2.3×10^6 lixels across our 2000 light rays. The light rays are randomly located, so the majority of these lixels are in the volume-filling voids of the simulation. The median H I number density in the simulation is 8.9×10^{-15} cm^{-3}, which for a path length of 5 Mpc corresponds to a column density of 1.4×10^{11} cm^{-2} or an optical depth of 5.8×10^{-7}. This means that most of the lixels suffer no meaningful attenuation of the UVB. Only 3425 lixels (0.15%) have a UVB attenuation of at least 1%. Including the self-absorption correction increases this to 3429 lixels. Only 93 lixels have a total attenuation of at least 10%. Table 4.1 summarizes the number of lixels above various attenuation thresholds.

The clustering of matter in overdense regions makes the H I number density of a lixel a good predictor of its UVB attenuation. Figure 4.3 shows the distribution of UVB attenuations (without self-absorption) as a function of n_{HI}. At the median simulation n_{HI} of 8.9×10^{-15} cm^{-3}, the probability of a 5% or greater attenuation is $\sim 10^{-6}$. Reaching a 10% probability for 5% attenuation requires $n_{HI} \gtrsim 10^{-9}$ cm^{-3}. H I number densities this high are only found in overdense regions,

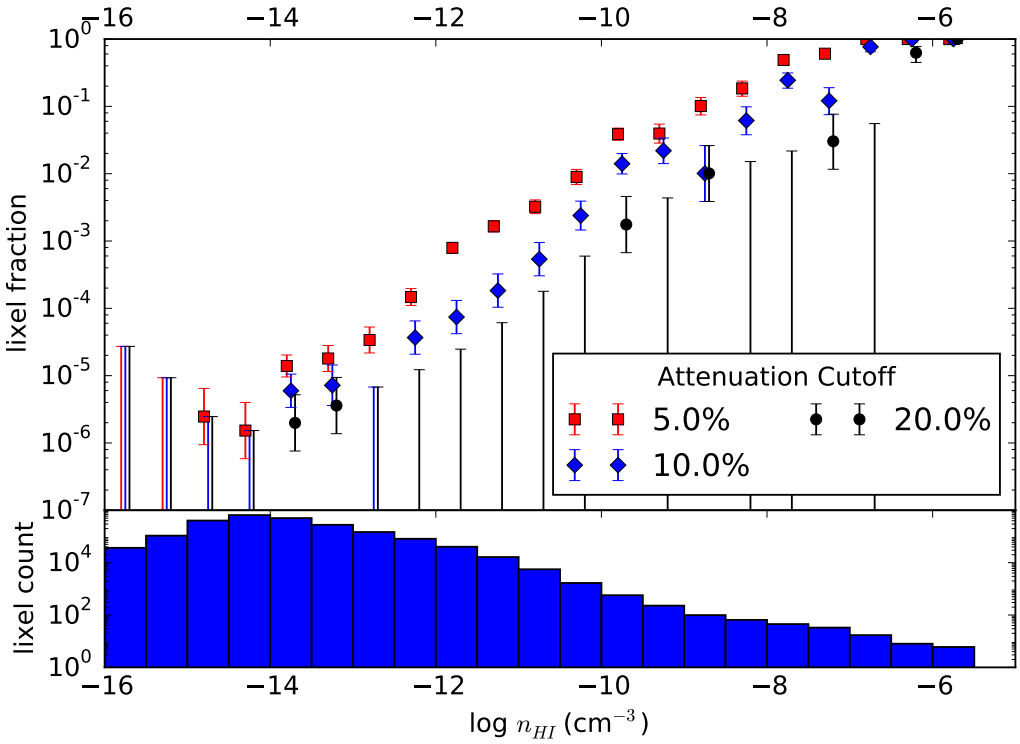

Figure 4.3 Histogram of external UVB attenuation as a function of lixel H I number density. The red squares, blue diamonds, and black circles show the fraction of lixels with attenuations of at least 5%, 10%, and 20%, respectively. Number densities $n_{HI} \gtrsim 10^{-9}$ cm^{-3} are needed for a 10% chance of local UVB attenuation of $\geq 5\%$. The bottom panel is a histogram of the lixel n_{HI} distribution.

typically in the vicinity of a galaxy. Of the lixels with $n_{HI} > 10^{-9}$ cm^{-3}, 79% are found within the virial radius of the nearest dark matter halo. Greater UVB attenuations require correspondingly higher gas densities. A 10% chance of 10% attenuation requires $n_{HI} \gtrsim 10^{-8}$ cm^{-3}, with 93% of these lixels found within a halo's virial radius. The corresponding values for 20% attenuation are $n_{HI} \gtrsim 10^{-7}$ cm^{-3} with all lixels within r_{vir} of the nearest halo.

A reduced flux of ionizing photons is not sufficient to guarantee a change in the hydrogen ionization balance of a lixel. H II is produced through both photoionization and collisional ionization. For a reduced photoionization rate to produce a significant increase in the neutral hydrogen fraction, photoionization must be the dominant ionization process. The balance between the ionization rates depends on both density and temperature. Figure 4.4 shows the ratio of the two ionization rates as a function of electron density and temperature. At the low densities found in the IGM, photoionization is always the dominant process for hydrogen. However, in the overdense regions where UVB attenuation becomes important, collisional ionization becomes significant for $T \gtrsim 10^5$ K. The majority of this dense gas is at cooler temperatures, but 12% of the lixels with $n_{HI} > 10^{-9}$ cm^{-3} are collisionally ionized.

Observationally, H I in the IGM is seen primarily through absorption lines, from which column densities (N_{HI}) and gas properties are inferred. There is a particularly strong correlation between N_{HI} and the density of the absorber's gas, shown in Figure 4.5 for our simulated absorbers. The correlation does have a significant spread, with absorbers exhibiting a range of ~ 2 dex in n_{HI} at fixed column density. Low column density absorbers are by far the most common, with absorber counts peaking at $\log N_{HI} \approx 12.2$ and $\log n_{HI} \approx -11.9$. As discussed earlier, a density of $n_{HI} \gtrsim 10^{-9}$ cm^{-3} is required for 10% probability of $\geq 5\%$ UVB attenuation. This corresponds to a column density of $N_{HI} \gtrsim 10^{15}$ cm^{-2}. The likelihood of significant UVB attenuation increases further at high column densities. In addition, the ionization balance shifts more firmly in favor of photoionization at the highest column densities. For 10^{15} cm$^{-2} < N_{HI} < 10^{16}$ cm^{-2}, eight out of 47 absorbers are dominated by collisional ionization, while for $N_{HI} \geq 10^{16}$ cm^{-2}, the same is true for only one out of 34 absorbers.

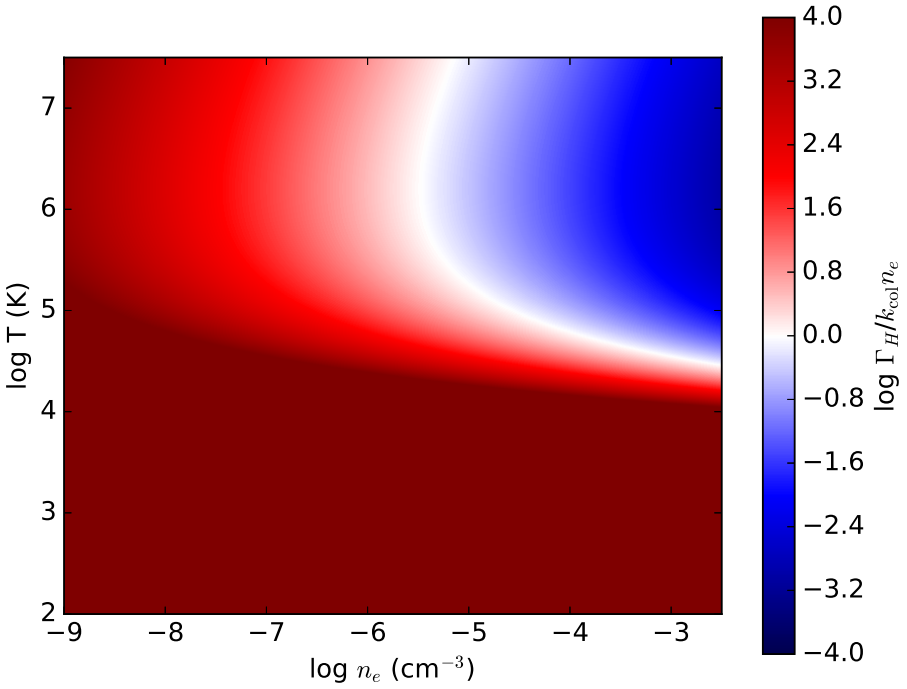

Figure 4.4 Relative rates of photoionization and collisional ionization of H I as a function of electron density and temperature. Red areas of the plot are photoionization dominated, while collisional ionization dominates the blue region in the upper right. When collisional ionization is dominant, attenuation of the UVB does not have a significant effect on the hydrogen ionization balance.

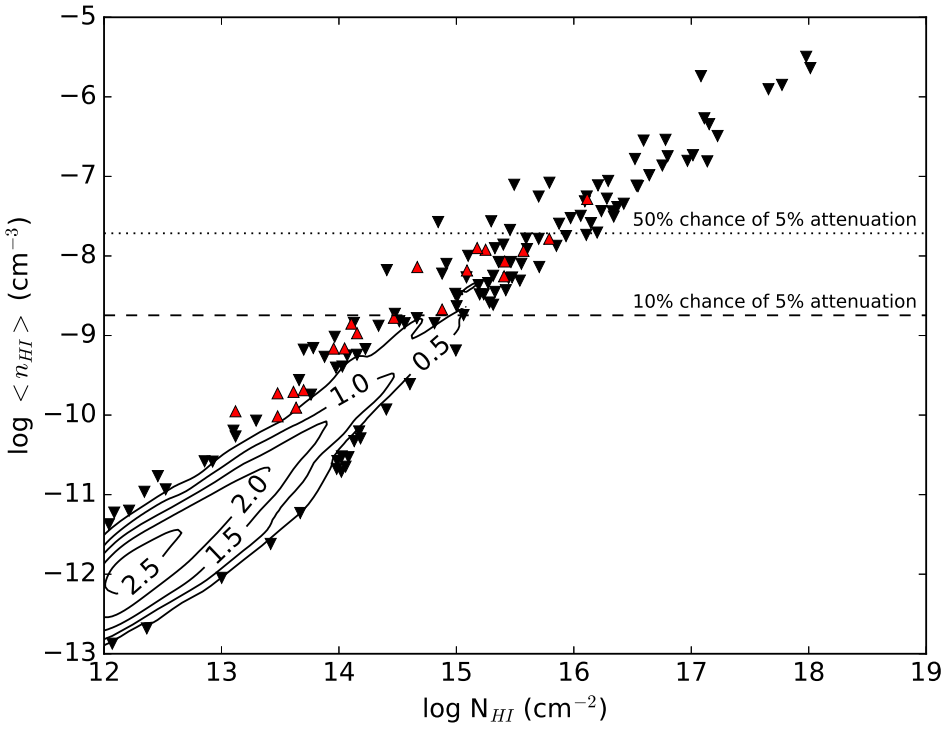

Figure 4.5 Relationship between H I absorber column density and column-density-weighted mean n_{HI} for our simulated absorbers. Contours are the log of absorber counts per unit redshift and per dex in N_{HI} and n_{HI}. Absorbers in lower density regions of the plot are individually marked. The downward-facing black triangles mark absorbers that are photoionization dominated, while the upward-facing red triangles are collisionally ionized. The dashed and dotted horizontal lines mark thresholds in n_{HI} for the specified chance of 5% UVB attenuation, based on a power-law fit to the data in Figure 4.3. The majority of absorbers with $N_{HI} < 10^{15}$ cm^{-2} have densities too low to see significant UVB attenuation.

Table 4.2. Increases in N_{HI} due to external attenuation of the UVB.

N_{HI} (cm^{-2})	N_{abs}	N_{HI} Ratio > 1.05	> 1.1	> 1.2
10^{14} – 10^{15}	205	3	0	0
10^{15} – 10^{16}	47	7	2	0
10^{16} – $10^{17.2}$	29	22	11	4
$> 10^{17.2}$	5	5	5	4

Note. — Columns give counts of absorbers above the specified thresholds in the ratio of attenuated to unattenuated column density.

Our absorber creation method allows us to directly compare the column densities of absorbers with and without attenuation of the UVB. A baseline set of H I absorbers are identified using the unattenuated equilibrium n_{HI} values. Column densities are then calculated for the same sets of lixels using the H I number density fields with UVB attenuation included to produce sets of matched absorbers. Tables 4.2 and 4.3 summarize the changes in column density due to external attenuation and external attenuation plus self-absorption, respectively. The derived column density ratios are in good agreement with our qualitative inferences from Figure 4.5. Significant UVB attenuation is rare for column densities below 10^{15} cm^{-2}, and self-absorption effects are entirely absent. The importance of attenuation grows at the highest Lyα forest column densities, but a 5% or greater increase in N_{HI} is still seen in fewer than 25% of absorbers. Partial Lyman-limit systems are significantly impacted by external attenuation, with 22 out of 29 absorbers exhibiting an increase in column density of 5% or more. At the highest end of the column density distribution, our light rays contain five Lyman-limit systems with $N_{HI} > 10^{17.2}$ cm^{-2}. The LLSs are all found in high density environments, with external UVB attenuation resulting in H I column density increases of at least 10%. By definition, a LLS also experiences significant self-absorption. This self-absorption can have extreme effects on the resulting column densities; the highest column density system in our data undergoes a more than 20-fold increase in N_{HI} from 1.0×10^{18} cm^{-2} to 2.2×10^{19} cm^{-2}.

Table 4.3. Increases in N_{HI} due to external attenuation and self-absorption of the UVB.

N_{HI} (cm^{-2})	N_{abs}	N_{HI} Ratio > 1.05	> 1.1	> 1.2
10^{14} – 10^{15}	205	3	0	0
10^{15} – 10^{16}	47	10	2	0
10^{16} – $10^{17.2}$	29	26	18	11
$> 10^{17.2}$	5	5	5	5

Note. — Columns give counts of absorbers above the specified thresholds in the ratio of attenuated to unattenuated column density.

For these systems, the calculated final column densities are likely underestimates, as our simple self-absorption correction is no longer sufficient. We will discuss this in more detail in Section 4.5.2.

4.5 Discussion

The lack of even 5% increases in column density for H I absorbers with $N_{HI} \leq 10^{15}$ cm^{-2} means that an "inverse proximity effect" is not important for the column density distribution of Lyα forest absorbers. Figure 4.6 compares the simulated column density distributions both without UVB attenuation (solid black) and with both external attenuation and self-absorption (dashed blue) to the observed distribution from Danforth et al. (2016). Bringing the slopes of the simulated and observed distributions into agreement for $N_{HI} \gtrsim 10^{13.5}$ cm^{-2} would require many simulated Lyα forest column densities to increase by a factor of $\sim 2 - 3$ as opposed to the $< 5\%$ effect from local attenuation.

Although the explanation for the slope of the Lyα forest column density distribution must lie elsewhere, local attenuation of the UVB is important at higher column densities. The consistently high degree of external UVB attenuation seen in the pLLSs and LLSs is not surprising. It simply indicates that we do not view them from a privileged perspective; their observed high H I column densities are matched by equally large columns out of the line of sight. The lack of attenuation

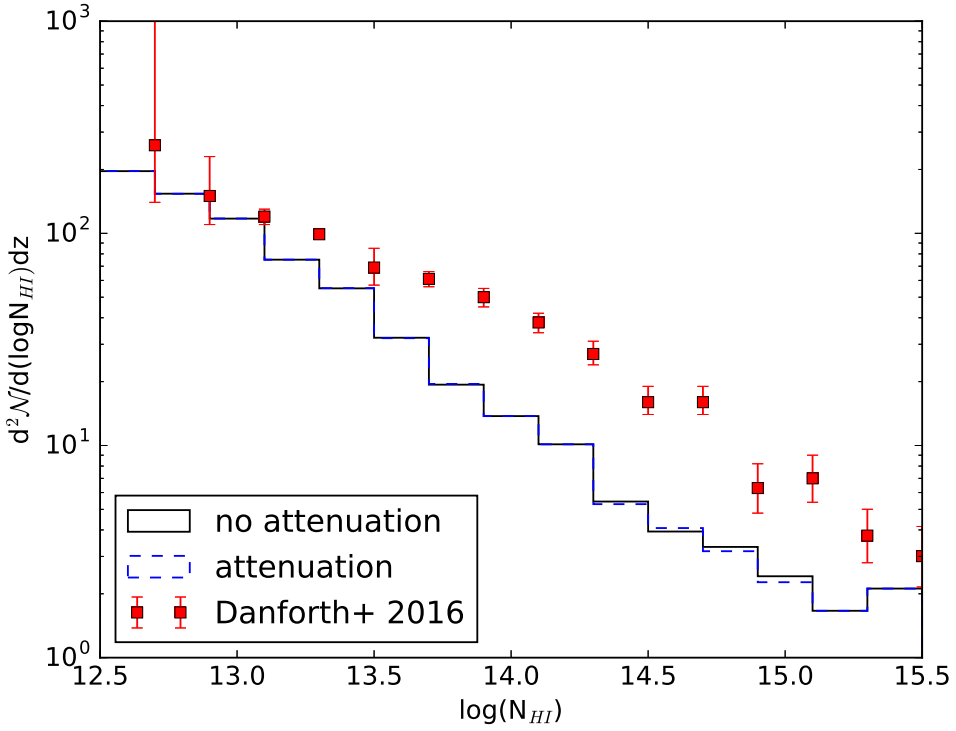

Figure 4.6 Simulated H I absorber column density distributions without (solid black) and with (dashed blue) local attenuation of the UVB compared to the observed distribution from Danforth et al. (2016). Although the simulated and observed distributions are consistent for $N_{HI} \lesssim 10^{13.5}$ cm^{-2}, the absorber counts in the simulated distribution drop off too steeply at higher column densities. The lack of significant increases in column density due to local attenuation for $N_{HI} \lesssim 10^{16}$ cm^{-2} means that an "inverse proximity effect" cannot account for the difference in the distributions.

in Lyα forest absorbers with $N_{HI} < 10^{15}$ cm^{-2} means that the majority of these absorbers do not come from outer regions of the same structures that produce pLLSs and LLSs. If they did, then they would have significant H I optical depths in at least some directions out of the line of sight. Instead, most of these absorbers come from structures with lower peak overdensities. Using the information on nearby dark matter halos included in the light rays, we can compare the host environments of the absorbers in these two column density ranges.

4.5.1 Nearest Halo Properties

The majority of Lyα forest absorbers are thought to arise in the IGM, likely along filaments in the cosmic web. In contrast, the densities of pLLSs and LLSs require that they be circumgalactic in origin. This implies that there must be some column density at which H I absorption lines transition from primarily tracing the IGM to primarily tracing CGM gas. Figure 4.7 shows the relationship between column density and distance to the nearest dark matter halo for our simulated H I absorbers. Distances are measured relative to the halo's virial radius, as this directly correlates with the solid angle covered by the halo as viewed from the absorber. There is a clear transition between IGM and CGM absorbers at $N_{HI} \sim 10^{14}$ cm^{-2}. Above this column density, almost all of the absorbers are found within $2r_{vir}$ of the nearest galaxy. The CGM H I absorbers include column density ranges both with and without significant UVB attenuation, so the transition from IGM to CGM absorbers is not the primary source of this difference.

Each absorber also stores information on the virial mass of the nearest halo. Figure 4.8 shows the distribution of halo virial masses for three different H I column density ranges. Only absorbers within $2r_{vir}$ of the nearest halo are included, as absorbers at larger distances are likely associated with the IGM instead. Although each distribution has significant scatter, there is a clear progression toward more massive halos for higher column density absorbers. The absorbers with 10^{14} cm$^{-2} < N_{HI} \leq 10^{15}$ cm^{-2} have nearest halos with a median mass of 10^{11} M$_{\odot}$ and a median impact parameter of $1.0r_{vir}$ ($\sim$ 130 kpc), while the pLLS and LLS absorbers have host halos with a median mass of $10^{11.7}$ M$_{\odot}$ and median impact parameter of $0.4r_{vir}$ ($\sim$ 90 kpc). This helps

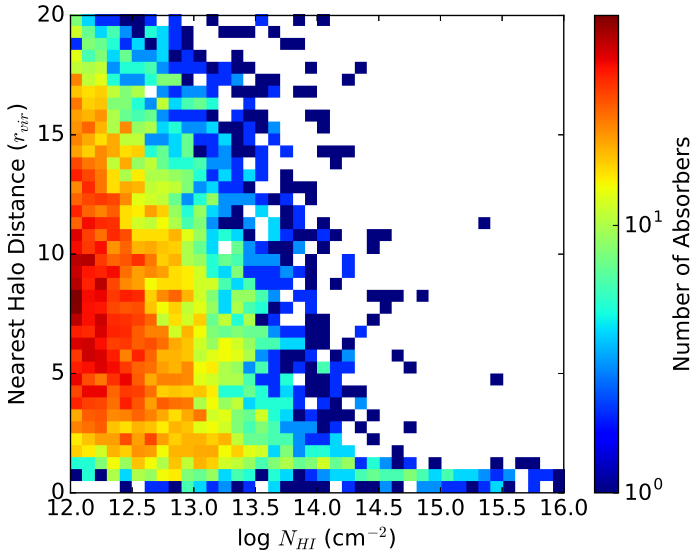

Figure 4.7 Histogram of absorber counts in bins of log N_{HI} and distance to the nearest dark matter halo. Distances are scaled to the halo's virial radius. At a column density of $\sim 10^{14}$ cm^{-2}, the H I absorbers transition from tracing the IGM to tracing the CGM.

to explain the strong correlation of UVB attenuation with column density. Although all of these absorbers are associated with the CGM of galaxies, higher column density absorbers are found near more massive halos and at smaller impact parameters, which in turn leads to higher H I optical depths.

The trends seen here are broadly consistent with circumgalactic H I column densities in the COS-Halos survey (Tumlinson et al. 2011, 2013; Werk et al. 2012). COS-Halos used AGN sight lines to probe the CGM of 44 galaxies with $10^{11.2}$ M$_\odot \leq M_{vir} \leq 10^{13.5}$ M$_\odot$ (with $\sim 80\%$ having $M_{vir} \leq 10^{12.5}$ M$_\odot$) and impact parameters out to ~ 150 kpc. Of their 40 H I detections, 9 had $N_{HI} \leq 10^{15}$ cm^{-2}, 18 had 10^{15} cm$^{-2} < N_{HI} \leq 10^{16}$ cm^{-2}, and 13 had $N_{HI} > 10^{16}$ cm^{-2}. Many of the derived column densities are lower limits due to line saturation, so the true fraction of pLLSs and LLSs is likely higher. The absorber counts are consistent with Figure 4.8, which shows that for $M_{vir} \geq 10^{11.5}$ M$_\odot$, absorbers in these three column density ranges are found in roughly equal proportions. The relatively scarcity of $N_{HI} \leq 10^{15}$ cm^{-2} absorbers in the COS-halos data is due to their ~ 150 kpc impact parameter cutoff, as many of our low column density absorbers are found at larger separations.

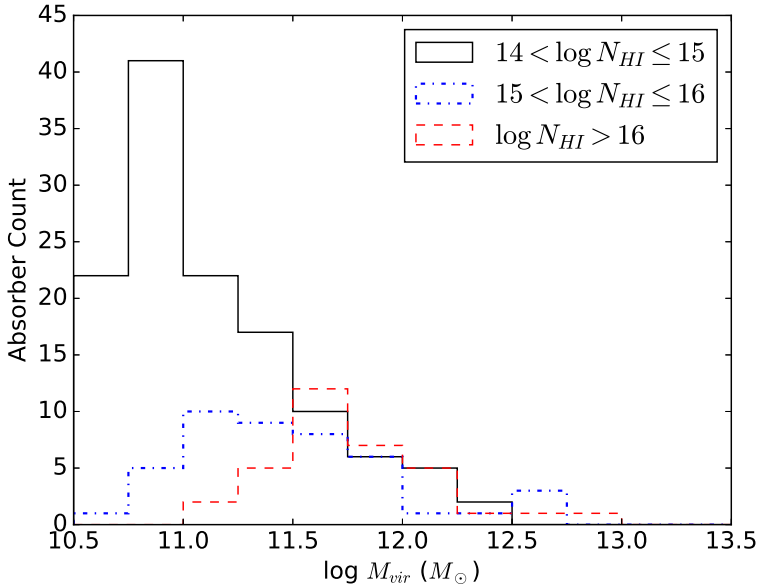

Figure 4.8 Histograms of nearest halo virial mass for absorbers with 10^{14} cm$^{-2} < N_{HI} \leq 10^{15}$ cm^{-2} (solid black), 10^{15} cm$^{-2} < N_{HI} \leq 10^{16}$ cm^{-2} (dot-dashed blue), and $N_{HI} > 10^{16}$ cm^{-2} (dashed red). Only absorbers within $2r_{vir}$ of the nearest halo are included. The high column density absorbers are near significantly more massive halos.

4.5.2 Lyman-Limit Systems

The external UVB attenuations in our analysis are calculated using the unattenuated n_{HI} values from the simulation. However, in principle, the increased n_{HI} values due to an attenuated UVB in turn imply higher H I optical depths to neighboring regions. For the majority of regions with low optical depths this second-order correction is insignificant. A percent-level change in the density of given grid cell has only a minor impact on the optical depth of a 5 Mpc ray, and only a small subset of the rays from a nearby lixel will pass through the cell. For lixels in these low-density regions, our simple attenuation calculation produces accurate photoionization rates.

The accuracy of this approach begins to break down as optical depths approach unity. At this point, the H I number densities with and without the attenuation correction can imply significantly different optical depths. This is particularly true of LLSs where, by definition, the H I optical depth at the hydrogen ionization threshold is at least one over a relatively small number of lixels. This is the reason why our self-absorption correction uses the post-attenuation n_{HI} value for a

cell. However, for accurate column densities in pLLSs and LLSs, a fully iterative approach should be used. Regions necessitating an iterative approach can be identified either by absorber column densities, or by the same density cutoffs used for the self-absorption correction. In these regions, alternating rounds of external attenuations and self-absorptions should be calculated for all cells (instead of just cells intersected by a light ray), with the equilibrium densities calculated from each step used as inputs for the next one. The iteration will continue until a desired accuracy is reached in the lixels contained in the region. The rarity of LLSs means that the iterative approach will only need to be applied in a small number of regions.

At the highest overdensities, even this iterative approach may prove insufficient. The densest lixel in our light rays has $n_{HI} = 3.2 \times 10^{-6}$ cm^{-3}, which implies a column density of 9.2×10^{17} cm^{-2} across the length of the cell, or an optical depth of 4. At this point, attenuation of the UVB should produce varying H I densities across the cell, and our assumption of a uniform n_{HI} in the self-absorption correction is no longer correct. Ideally, in a study of LLSs these high-density regions would be simulated at higher spatial resolution, but this is not always feasible from a computational standpoint. A computationally cheaper compromise is to increase the resolution of these regions for the post-processing step only. Each high density cell can be refined into higher resolution subcells, which are initialized with the parent cell's gas properties. The initially uniform n_{HI} of the subcells will rapidly evolve due to variations in external UVB attenuation. With sufficient refinement, the optical depth in any given subcell will be small, and only the external attenuation step will be needed. Refinement in post-processing can thus serve as a more accurate replacement for the self-absorption correction. Implementing and testing this approach is beyond the scope of the current work, but would be quite useful in a study focused on the pLLS and LLS populations.

4.6 Summary

We implement a simple post-processing ray-tracing routine to determine the effects of local density variations on the strength of the metagalactic ionizing UV background and its effects on hydrogen ionization balance in the IGM and CGM. Using mock AGN lines of sight, we identify H I

absorbers analogous to the structures found in observations of the Lyα forest. Our main results are the following:

(1) Significant UVB attenuation is rare, with a 1% or greater effect seen in only 0.15% of the lixels in our light rays.

(2) Both n_{HI} of individual lixels and N_{HI} of absorption systems correlate strongly with UVB attenuation.

(3) Local attenuation is unimportant in the Lyα forest, with almost no effects seen for $N_{HI} \leq 10^{15}$ cm^{-2}. An "inverse proximity effect" cannot explain the difference in slopes between the simulated and observed Lyα forest column density distributions.

(4) Significant attenuation is found for $N \geq 10^{16}$ cm^{-2}. With self-absorption included, pLLSs commonly show a 10% or greater increase in column density, and all LLSs have at least a 20% increase in N_{HI}.

(5) Almost all H I absorption systems with $N_{HI} > 10^{14}$ cm^{-2} are associated with the CGM, with at least one dark matter halo of $M_{vir} \geq 10^{10.5}$ M$_{\odot}$ located within $2r_{vir}$. Higher column density absorbers are found near more massive halos and at smaller impact parameters, which leads to increased UVB attenuation.

Acknowledgements

This work utilized the *Janus* supercomputer, operated by the University of Colorado and supported by the National Science Foundation (award number CNS-0821794), the University of Colorado Boulder, the University of Colorado Denver, and the National Center for Atmospheric Research. Computations described in this work were performed using the publicly-available `Enzo` code (http://enzo-project.org), which is the product of a collaborative effort of many independent scientists from numerous institutions around the world.

Chapter 5

Measuring the Spatial Extent of Circumgalactic Oxygen Absorbers in Cosmological Simulations

The contents of this chapter have been submitted to *Monthly Notices of the Royal Astronomical Society* as Moloney & Shull.

5.1 Abstract

Highly ionized oxygen is one of the most important tracers of flows of metal-enriched gas between galaxies and the surrounding circumgalactic (CGM) and intergalactic medium (IGM). O VI is well studied in the CGM, but only out to distances of one to two virial radii. We use a large, uniform-resolution cosmological simulation to study the distribution of circumgalactic oxygen ions around dark matter halos with $10^{11}\,\mathrm{M}_{\odot} \leq M_{vir} \leq 10^{14}\,\mathrm{M}_{\odot}$ at distances out to $5r_{vir}$. We use models of collisional ionization equilibrium (CIE) and collisional + photoionization equilibrium (C+P) to study the spatial distribution of O VI, O VII, and O VIII ion fractions, as well as to construct simulated absorption covering factors modeled after the COS Halos survey of CGM absorption lines. The CIE model produces an extended O VI distribution reaching distances of $4r_{vir}$, with helium-like O VII as the dominant ionization state in circumgalactic gas. The C+P model restricts O VI to reside within the virial radius, with the majority of oxygen in the form of hydrogenic O VIII. Analyzing the physical conditions underlying each ionization model, we find that outside of the virial radius the dominant ionization process depends on the presence of high density structures or interfaces below the resolution of our simulation. Identifying the true ionization state

at these distances will require either simulations with higher spatial resolution or a COS Halos-like study of O VI extending to large impact parameters. Additionally, we present a method for using simulated covering factors as a prior to more accurately identify absorber-galaxy pairs in crowded environments.

5.2 Introduction

Understanding the flows of gas into and out of galaxies is a crucial part of studying galaxy growth and evolution. Inflowing gas from the intergalactic medium (IGM) can replenish the interstellar medium (ISM) and provide fuel to sustain ongoing star formation. Disrupting this gas accretion can quench star formation and lead to the transition from a star-forming disc galaxy to a "red and dead" elliptical (Larson et al. 1980). Feedback from stellar winds, supernovae, and active galactic nuclei (AGNs) ejects metal-enriched gas into the circumgalactic medium (CGM). These outflows are seen in the local universe as the galactic winds of starburst galaxies such as M82 (e.g., Watson et al. 1984). During the peak of star formation at $z \sim 2$, strong galactic winds were widespread. The ultimate fate of the ejected gas depends on the energetics of the wind (e.g., Oppenheimer & Davé 2006; Wiersma et al. 2010). Material traveling at speeds below the escape velocity will eventually be re-accreted through a "galactic fountain" (Shapiro & Field 1976), while faster-moving gas can escape the galaxy's gravitational attraction and travel on to enrich the IGM (Dekel & Silk 1986). At high redshift, the higher star formation rates and lower masses of typical galaxies lead to significant IGM metal enrichment.

The large fractional abundance of oxygen makes its high ions some of the most useful observational tracers of galactic outflows and circumgalactic gas in general. O VI in particular has a strong UV doublet at $\lambda\lambda$ 1032, 1038 Å which makes it the most commonly observed metal species in warm-hot extragalactic gas. The COS Halos survey (Tumlinson et al. 2011; Werk et al. 2013) found that strong O VI absorption is nearly universal within the virial radius of star-forming L* galaxies. At temperatures of 10^6 K and higher, O VI has been replaced by O VII and O VIII. Much of the volume of the CGM may contain gas in this hot phase (Stocke et al. 2013). Although the

X-ray absorption from O VII and O VIII is significantly more difficult to detect, such absorption has been observed in the CGM of the Milky Way (Nicastro et al. 2002; Gupta et al. 2012). Cosmological zoom simulations of the CGM (e.g., Oppenheimer et al. 2016; Gutcke et al. 2017) provide additional context for the observations by connecting absorption lines to the underlying physical conditions and masses of the gas phases that they trace.

Metal-enriched gas also plays an important role in understanding the IGM. At $z = 0$, a significant fraction of the baryons in the universe reside in reservoirs that have not yet been identified observationally (Shull et al. 2012b; Bregman 2007). Many of these "missing baryons" likely exist in the Warm-Hot (WHIM) and hot phases of the IGM, which contain O VI, O VII, and O VIII. Observational surveys of O VI absorption in the IGM (Tripp et al. 2008; Tilton et al. 2012; Savage et al. 2014; Danforth et al. 2016) find $\sim 10\%$ of the cosmic baryons in the O VI-traced WHIM. Simulations indicate that an additional $\sim 15\%$ of the baryons may be found in O VII and O VIII-traced gas (Shull et al. 2012b). Some detections of O VII and O VIII absorption in the IGM have been made in AGN sight lines (e.g., Fang et al. 2010; Nicastro et al. 2013). However, the small sample size and low significance of the detections makes any statistical analysis of the hot IGM phases problematic.

All of the oxygen seen in the IGM was originally created within galaxies, but an accurate model of the flow of material from the CGM to the IGM is needed to place the IGM observations in their proper context. However, our understanding of the distribution of oxygen in extended circumgalactic gas is currently lacking. CGM observations of O VI such as COS Halos are restricted to within the virial radius. Similarly, the refined volume of cosmological zoom simulations typically extends to distances of only 2–3r_{vir}. Most of the large IGM absorption line surveys have not examined the distribution of their absorbers with respect to galaxies. Those that have (e.g., Stocke et al. 2006, 2013) find modest covering factors for O VI out to distances of $\lesssim 1$ Mpc, but the sample sizes are too small to fully constrain the O VI distribution.

In this paper, we use a large, uniform-resolution cosmological simulation to study the extended circumgalactic distribution of high oxygen ions. We use two ionization models to calculate

the oxygen ion fractions: a collisional ionization equilibrium (CIE) model and a collisional + photoionization (C+P) model. These two models allow us to explore the spatial distribution of circumgalactic O VI, O VII, and O VIII and the physical conditions governing it. In Section 5.3, we describe the methods used to run and analyze our simulation. Section 5.4 presents the spatial distribution of circumgalactic O VI ion fractions and absorbers as a function of halo virial mass (M_{vir}). Section 5.5 describes the spatial distribution of O VII and O VIII. In Section 5.6, we discuss the physical conditions responsible for setting the oxygen ion balance. We also describe the difficulty of deciding which galaxy is responsible for a given absorption line in dense environments, and propose a new method for determining this using simulated covering factors as a prior. Section 5.7 summarizes our conclusions. Throughout the paper, physical distances are given in comoving units unless otherwise specified.

5.3 Simulation Methods

The simulation analyzed in this paper was run by Britton Smith and first described in Shull et al. (2012a). The simulation was produced using the Eulerian N-body + hydrodynamics code `Enzo`[1] (Bryan et al. 2014). It covers a representative $50h^{-1}$ Mpc cosmological volume with a uniform 1536^3 grid. This provides a dark matter particle mass of $2.2 \times 10^6 h^{-1}\,\mathrm{M}_\odot$ and a grid cell size of $32.6h^{-1}$ kpc. The simulation domain was initialized at $z = 99$ using the initial conditions generator included with `Enzo` and run to $z = 0$. The cosmological parameters for the simulation are the WMAP-7 concordance values (Komatsu et al. 2011) with $\Omega_m = 0.273$, $\Omega_\Lambda = 0.727$, $\Omega_b = 0.0455$, $H_0 = 70.2$ km s^{-1} Mpc^{-1}, $\sigma_8 = 0.807$, and $n_s = 0.961$. The subgrid astrophysics models used in the simulation, along with convergence testing and comparisons to observations, are fully described in Smith et al. (2011). We summarize the details most relevant to the current research in the following section.

Star particles are formed in the simulation following the prescription of Cen & Ostriker (1992). Grid cells can form stars if they have a density of at least 100 times the critical density,

[1] http://enzo-project.org

negative divergence of the velocity field, and a cooling time of less than the dynamical time. The star formation efficiency within these cells is set to 10%. Stellar feedback returns material to the ISM and CGM in the form of gas, metals, and energy. A star particle returns 25% of its total mass to the simulation, of which 10% takes the form of metals, and 10^{-5} of the star particle's rest mass energy is converted to thermal feedback. Although star particles are formed instantaneously, feedback is gradual, with a rate that peaks after one dynamical time and then decays exponentially. Spatially, stellar feedback is distributed evenly over a 27 grid cell cube centered on the star particle. This "distributed feedback" model is necessary to mitigate the rapid cooling and subsequent overproduction of stars that occurs if all feedback is deposited into a single grid cell (Smith et al. 2011). The simulation does not contain a model for AGN growth and feedback. The most important effect of this is that high mass galaxies that would typically have their star formation quenched by AGN activity instead continue to produce stars through $z = 0$.

The thermal state of gas in the simulation is governed by a non-equilibrium chemistry solver for H and He (Abel et al. 1997; Anninos et al. 1997). Metal cooling rates are derived from precompiled CLOUDY[2] (Ferland et al. 2013) tables under the assumption of ionization equilibrium and solar metal abundances (Smith et al. 2008). Photoionization and radiative heating rates assume a spatially uniform metagalactic UVB. The simulation uses the 2005 update to the Haardt & Madau (2001) UVB, which is included in CLOUDY. The UVB is initialized at $z = 8.9$ and reaches full strength at $z = 8$.

5.3.1 Halo Finding

Dark matter halos were identified in 23 redshift outputs with $0 \leq z \leq 0.4$ using the `Rockstar` halo finder (Behroozi et al. 2013b). `Rockstar` finds halos and identifies substructure by linking particles based on their distance in six-dimensional phase space. The halo catalogs produced for each output include the position, peculiar velocity, virial mass, and virial radius of each halo. The smallest halos in the catalogs have $M_{vir} \approx 10^{9.5}\,\mathrm{M}_{\odot}$. However, our analysis only includes halos

[2] http://nublado.org

with $M_{vir} \geq 10^{11}\,\mathrm{M}_{\odot}$, which contain enough dark matter particles for robust star formation. The `Rockstar` halo catalogs only include dark matter masses; stellar masses are calculated by summing the masses of star particles within the halo's virial radius. Star particles found within two or more halos are assigned to the halo with the nearest center, scaled by the halo's virial radius. This leads to accurate stellar masses for central halos, but creates some uncertainty in the stellar masses of satellites.

The virial masses and radii of halos play a central role in our analysis, and there is significant variation in the definition of these terms in the literature. `Rockstar` calculates virial properties using the redshift-evolving virial overdensity from Bryan & Norman (1998). The virial overdensity (Δ_{vir}) is defined relative to the critical density and calculated as

$$\Delta_{vir}(z) = 18\pi^2 + 82\left[\Omega_m(z) - 1\right] - 39\left[\Omega_m(z) - 1\right]^2. \tag{5.1}$$

For each halo, `Rockstar` identifies a sphere, centered on the halo position, with mean density equal to Δ_{vir}. The radius and enclosed mass of this sphere are taken as r_{vir} and M_{vir}, respectively. The resulting virial masses and radii exhibit a tight correlation that depends only on redshift. A least-squares fit to this relationship in the halo catalogs gives

$$r_{vir} = (121\ \mathrm{kpc})(M_{vir}/10^{11}\,\mathrm{M}_{\odot})^{0.335}(1+z)^{0.327} \tag{5.2}$$

with an rms scatter in r_{vir} of 3 kpc.

5.3.2 Light Ray Creation

We conducted our analysis on a set of 430 mock AGN sight lines constructed from the same 23 simulation outputs used for the halo catalogs. A randomly oriented ray is chosen through each output, beginning at the output redshift and with sufficient pathlength to cover the Δz to the next output file. The rays are then combined into a single sight line covering the full redshift range $0 \leq z \leq 0.4$. Each sight line consists of thousands of individual line elements (lixels), which are the portion of the sight line passing through a single grid cell of the simulation. The light ray stores

the gas properties of each lixel, including density, temperature, bulk velocity, and metallicity. In addition, all halos within $5r_{vir}$ of a lixel are identified, and their unique identifiers, virial masses, virial radii, and distances to the lixel are recorded. If no halo is within $5r_{vir}$, then the properties of the nearest halo (scaled to the halo's virial radius) are stored instead.

Ionization fractions for O VI, O VII, and O VIII are calculated from the gas properties of each lixel using two different models. The first model assumes pure CIE. This model depends only on gas temperature and uses ionization tables from Sutherland & Dopita (1993). The second model uses equilibrium values including both collisional and photoionization processes. The C+P model calculates ionization fractions by interpolating the lixel gas properties on three dimensional grids of redshift, density, and temperature. We use grids from Oppenheimer et al. (2012), which were constructed from Cloudy models using the Haardt & Madau (2001) UVB. Ionization fractions are converted to number densities using the gas metallicity and assume solar abundance ratios.

Observational studies of AGN sight lines identify O VI through absorption lines. We identify synthetic absorbers in each sight line for comparison to observations. An absorber consists of a set of contiguous lixels where the ion of interest's number density is above a fixed floor (10^{-13} cm^{-3} for O VI). The absorber's column density is determined by integrating the number density of the ion along the length of the absorber. Column densities derived using this method are insensitive to the specific choice of density floor. Across our three ions and two ionization models, adjusting the density floor by 1 dex in either direction changes the number of identified absorbers by a maximum of 7.4% and a median of 1.2%. Column densities in this manner are also in good agreement with results from more sophisticated methods using synthetic spectra (Egan et al. 2014).

5.4 O VI Spatial Distribution

O VI is one of the most widely studied IGM metals due to the high abundance of oxygen and its strong UV doublet. Although the primary focus of this paper is on circumgalactic gas, comparisons to IGM observations provide a good test of metal production and ionization modeling in the simulation. Danforth et al. (2016) provide the most comprehensive study of the low-redshift

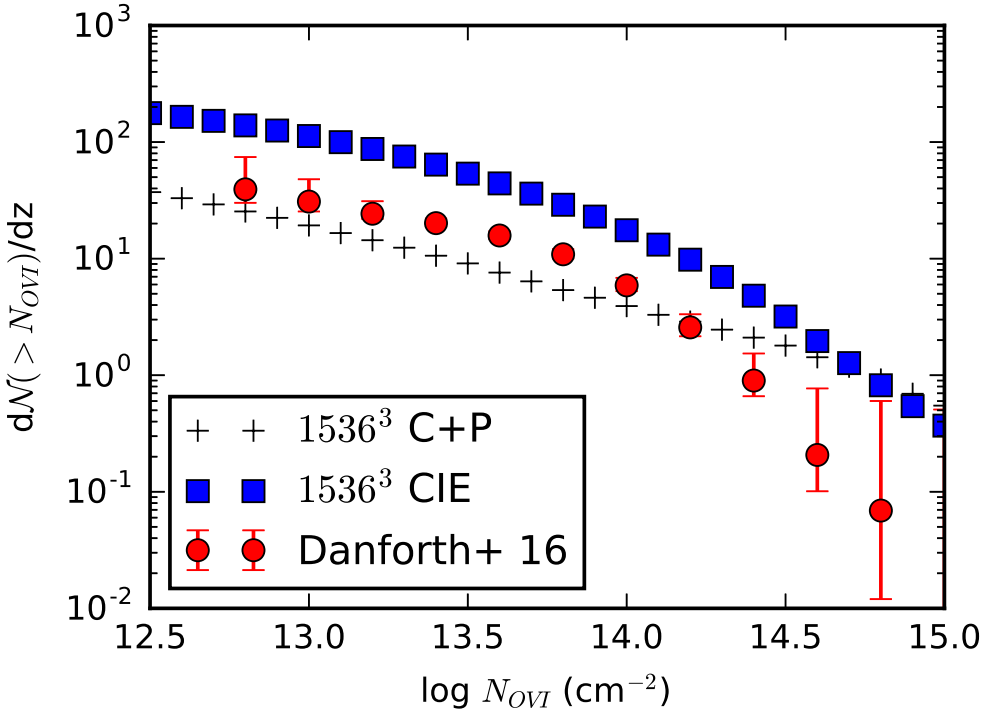

Figure 5.1 Cumulative O VI column density distribution per unit redshift. Red circles are observational data from Danforth et al. (2016). Blue squares and black pluses are simulated distributions using the CIE and C+P ionization models, respectively. The CIE model matches the slope of the observed distribution but systematically overpredicts the number of absorbers by a factor of $\sim$ 2–3.

IGM to date, with 280 O VI absorption systems across 82 AGN sight lines. Figure 5.1 compares their cumulative O VI column density distribution to the simulated results from our two ionization models. The CIE distribution qualitatively matches the shape of the observations, but its normalization is too high by a factor of 2–3 at all column densities. The C+P model produces more accurate numbers of low column density absorbers, but it converges with the CIE distribution at high columns, overpredicting the observations for $N_{OVI} \gtrsim 10^{14.2}$ cm^{-2}, which is the relevant column density range for CGM O VI absorption.

The primary cause of the high O VI abundance is an overproduction of stars, and hence metals, in the simulation. Figure 5.2 shows the stellar mass fractions of our simulated halos at $z = 0$ as a function of M_{vir}. The red line shows the median value for all halos with non-zero stellar mass, with the shaded region encompassing the middle 50% of the distribution. The blue line shows an observationally constrained distribution from the abundance matching model of Behroozi et al. (2013a) for comparison. The lack of a turnover in the simulation at high virial mass is due to the lack of AGN feedback mentioned in Section 5.3. The deviations at lower halo mass ($M_{vir} \sim 10^{12}\,\mathrm{M}_{\odot}$) where AGN activity is less pronounced may be partially due to some remaining overcooling and subsequent enhanced star formation from the distributed stellar feedback. Increased star formation leads to increased metal production, which in turn creates the elevated O VI column densities seen in Figure 5.1. Increased metallicity also produces enhanced metal line cooling. However, other than that, the effects on the fractional abundances of the oxygen ions studied in this paper are relatively small. In the context of this paper, the most useful interpretation of the elevated metallicity is that, while the spatial distribution of oxygen absorbers is accurate, their column densities are elevated by ~ 0.3 dex relative to observations.

5.4.1 Ionization Fraction

We begin studying the spatial distribution of O VI around halos by directly examining the O VI ionization fraction. The small difference in the ionization energies needed to create O VI and to ionize it to O VII (114 vs 138 eV) means that O VI is never a majority species. In CIE,

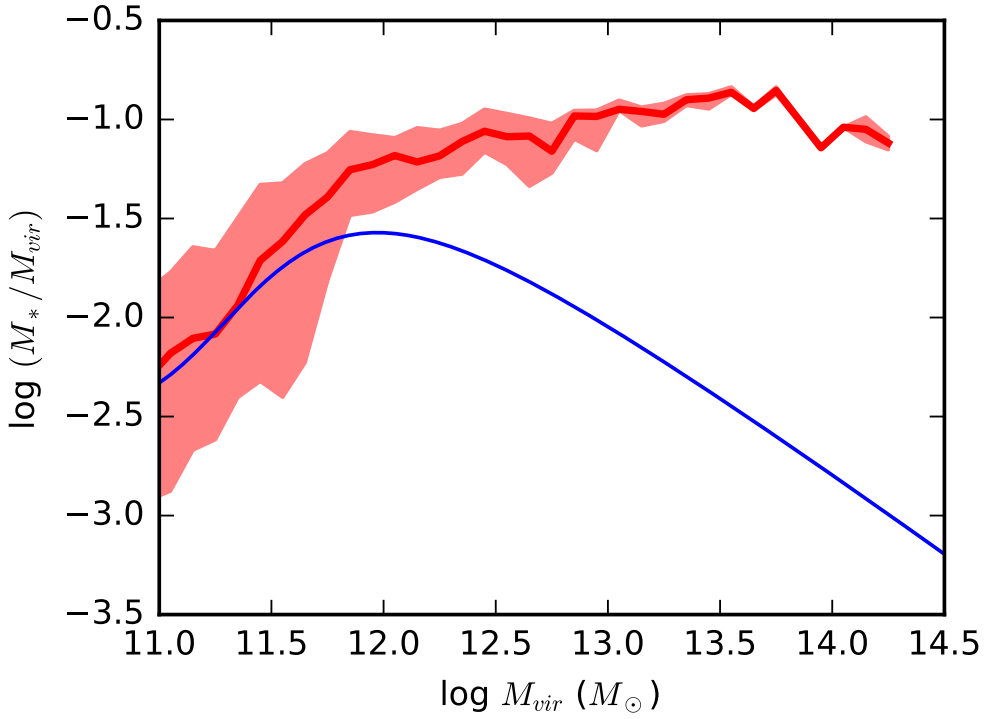

Figure 5.2 Stellar mass fraction of halos at $z = 0$. The red line is the median for all simulated halos with non-zero stellar mass, while the shaded region shows the middle 50% of the simulated distribution. The abundance matching model from Behroozi et al. (2013a) is plotted as the blue line. The growing gap between the two lines at high M_{vir} is primarily due to the lack of AGN feedback in the simulation.

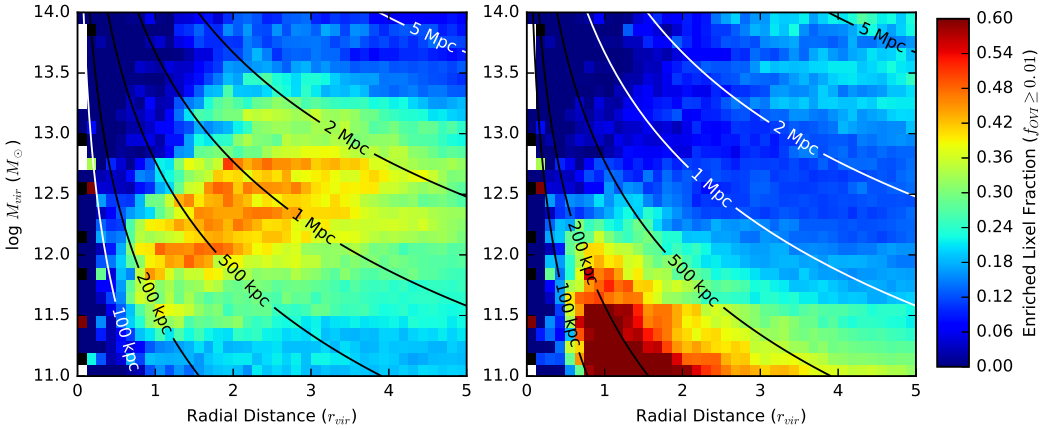

Figure 5.3 Spatial distributions of circumgalactic O VI enriched gas as a function of halo mass and radial distance (in virial radii). The colour bar indicates the fraction of lixels with an O VI ionization fraction of at least 1%. The left panel shows results for the CIE model, while the right panel shows the C+P abundances. Contours on the figure show lines of constant radial distance in physical units based on the relationship from Equation 5.2 with $z = 0.2$.

the peak ionization fraction of O VI is only 20%. However, the high overall abundance of oxygen and the strength of the O VI UV doublet means that even percent-level ionization fractions can produce observable column densities. Figure 5.3 shows the spatial distribution of O VI enriched gas, where we define a lixel as enriched if it has a fractional O VI abundance (relative to the total oxygen abundance) of at least 1%. In the CIE model (left panel), O VI is found in a broad region extending out to several virial radii around halos with $11.8 \lesssim \log(M_{vir}/\mathrm{M}_{\odot}) \lesssim 12.8$.

The C+P ionization model produces a markedly different distribution. O VI enriched gas is only found around halos with $\log(M_{vir}/\mathrm{M}_{\odot}) \lesssim 12.2$. The spatial extent of the gas is also restricted to distances of $1.5r_{vir}$ and below for the more massive halos. Only for halos below $10^{11.5}\,\mathrm{M}_{\odot}$ does the O VI enriched gas extend to distances of 2 virial radii and beyond. O VI is also more prevalent in the extended CGM of low mass halos than it is in any location in the CIE model.

The differences between the two models are due to the low gas densities found in the extended circumgalactic gas. At these low densities ($n_H < 10^{-4}$ cm^{-3}), gas that would contain O VI under CIE can be photoionized to O VII or higher ionization states given sufficient EUV and soft X-ray radiation fields (Oppenheimer & Davé 2009; Ford et al. 2013). At the same time, cooler gas around low mass halos (due to their lower virial temperatures) can be photoionized from low oxygen ions up to O VI. The gas conditions responsible for the differences between the two ionization models and the implications for the ionization state of circumgalactic oxygen will be discussed in more detail in Section 5.6.

5.4.2 Covering Factor

Ionization fraction is only one of the factors affecting the observability of O VI absorption. Gas density and metallicity combine with ionization fraction to determine the O VI number density. In addition, an AGN sight line passing near a galaxy will intersect gas with a range of radial distances determined by the sight line's impact parameter (distance of closest approach). To make comparisons to observations, we need to use discrete absorbers rather than individual lixels. COS Halos (Tumlinson et al. 2011, 2013; Werk et al. 2012, 2013) is the most comprehensive study

of circumgalactic O VI to date, so we match the creation of our synthetic observations to their techniques for ease of comparison.

Each dark matter halo within $5r_{vir}$ of a given light ray is assigned a systematic redshift based on the redshift of the nearest lixel. The peculiar velocity of the halo is then projected along the line of sight and used to create an observed redshift (z_{obs}) for the halo. Each lixel of the light ray is also assigned a z_{obs} based on the lixel's systematic redshift and the bulk velocity of the gas. The z_{obs} of absorbers, created as described in Section 5.3.2, is the O VI column density weighted mean z_{obs} of the component lixels. An absorber is considered associated with a given halo if the velocity offset (Δv) implied by their respective z_{obs} is less than 300 km s^{-1}, the velocity window used by COS Halos. The exact size of the velocity window has only a minor effect on the number of halo-absorber pairs. Using $\Delta v < 200$ km s^{-1} decreases the number of pairs by 20% for both ionization models. Broadening the velocity window to $\Delta v < 400$ km s^{-1} increases the number of pairs by 17% and 14% for the CIE and C+P models, respectively. In observations, absorption from multiple physical structures can be blended and difficult to distinguish. To account for this, we use the sum of the column densities of all absorbers within the velocity window as the column density of the absorption system associated with a given halo.

Figure 5.4 shows the spatial distribution of circumgalactic O VI absorption systems expressed as area covering factors. We define covering factor as the fraction of light ray-halo pairs with an associated O VI absorption system of $N_{OVI} > 10^{14}$ cm^{-2} located within the velocity window. This column density cut is at the upper end of the range of limiting column densities for the star-forming COS Halos galaxies ($10^{13.5}$ cm^{-2} to $10^{14.0}$ cm^{-2}) to account for the the overproduction of metals in the simulation.

Within one virial radius, both ionization models produce qualitatively similar area covering factors. Absorbers are common over a wide range of halo masses extending up to $M_{vir} \approx 10^{13}\,\mathrm{M}_{\odot}$. The peak O VI covering factors are found at somewhat lower virial masses in the C+P ionization model. The majority of the COS Halos observations fall within this one virial radius range. The star-forming galaxies in COS Halos (which are more representative of the halos in our simulation

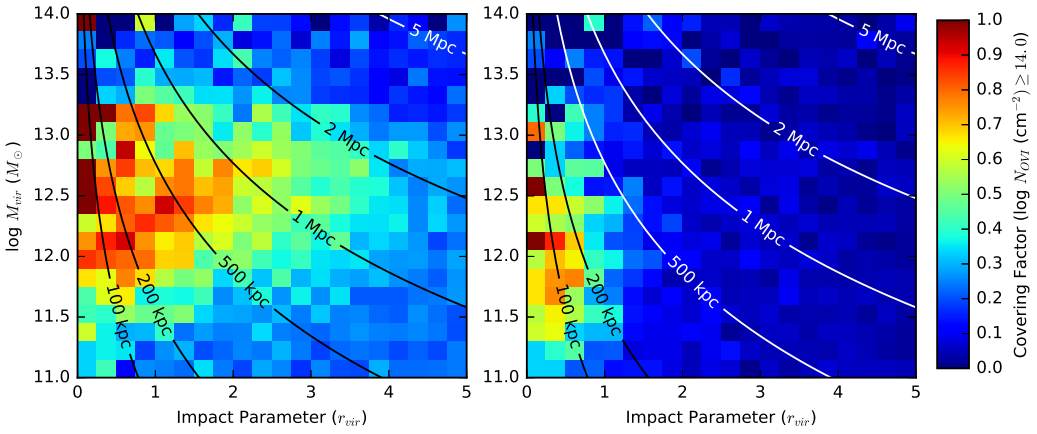

Figure 5.4 Covering factors of O VI as a function of halo mass and impact parameter (in virial radii). The covering factor within a given bin is defined as the fraction of light ray-halo pairs with an associated O VI absorption system with $N_{OVI} > 10^{14}$ cm^{-2}. The left panel shows covering factors for the CIE model, while the right panel contains the C+P distribution. Contours are the same as in Figure 5.3.

than passive galaxies) have typical masses in the range $11.5 \lesssim \log(M_{vir}/\mathrm{M}_\odot) \lesssim 12.1$ and an overall O VI covering factor of 90%. At the low mass end, this is in moderate tension with the CIE model, which produces covering factors of 40–60%. For halo masses of $\sim 10^{12}\,\mathrm{M}_\odot$ both ionization models produce area covering factors of $\sim$ 80%. The significantly lower ($\sim$ 30%) O VI covering factors around passive COS Halos galaxies may be heavily influenced by AGN feedback (Suresh et al. 2015), which is absent in our simulation.

Beyond one virial radius, the two ionization models produce completely different results. In the CIE model, the spatially extended O VI enriched gas from Figure 5.3 leads to covering factors $\geq$ 40% out to distances of $4r_{vir}$ for halos with $12.0 \leq \log(M_{vir}/\mathrm{M}_\odot) \leq 13.0$. In contrast, the C+P model leads to almost no O VI absorbers beyond the virial radius with column densities above 10^{14} cm^{-2}. Which ionization model is more accurate has important implications for the potential existence of extended O VI enriched halos around Milky Way-mass galaxies.

It is worth noting that the O VI covering factors at large impact parameters ($> 4r_{vir}$) are not representative of the abundance of O VI absorbers in the general IGM. Galaxies typically exist in overdense environments, so even gas not directly influenced by the galaxy will have higher than

average O VI number density. In the CIE model, the mean covering factor for impact parameters between 4 and $5r_{vir}$ is 23%, while the equivalent covering factor for a randomly chosen IGM location is only 4.3%. For the C+P model the equivalent covering factors are 4.1% and 0.8% for large impact parameters and random IGM locations, respectively.

5.5 O VII and O VIII Distributions

Although O VI is the oxygen species most commonly observed in the CGM and IGM, it is not the most abundant oxygen ion. Much of the volume of the IGM is thought to be filled with hot, low density gas where the oxygen is in the form of O VII, O VIII, or fully ionized O IX. Shull et al. (2012b) estimate that 15% of the baryons at $z = 0$, roughly half of the "missing baryons," may be in gas traced primarily by O VII and O VIII. The spectral lines of these ions are primarily weak X-ray transitions, which makes detecting this gas costly in terms of observing time at the relatively low spectral resolution of *Chandra* and *XMM-Newton*. Understanding the spatial distribution and column densities of potential O VII and O VIII absorbers is an important precursor to any planned observations.

Figure 5.5 shows the spatial distribution of O VII (left) and O VIII (right) for the CIE model. The distribution of O VII is similar to the O VI distribution in Figure 5.3 but for a higher halo mass range of $12.3 \lesssim \log(M_{vir}/\mathrm{M}_\odot) \lesssim 13.5$ and with a significantly greater peak abundance. The O VIII enriched gas is restricted to a narrow range of halo masses above $10^{13}\,\mathrm{M}_\odot$ and radial distances of less than $2r_{vir}$. Figure 5.6 shows the equivalent spatial distributions for the C+P model. In this model, O VIII is the dominant oxygen species in the majority of the circumgalactic gas. The abundance of O VIII in some regions is so high, that in the right panel of Figure 5.6 we raised the cutoff for a lixel to be considered O VIII enriched from an ionization fraction of 0.2 to 0.4 to maintain sufficient dynamic range. In both ionization models, the CGM around group-mass halos (top left corner of the figures) is missing both O VII and O VIII and is instead filled with fully ionized oxygen. The diagonal swath in the right panel of Figure 5.6 where the O VIII abundance dips is similarly dominated by O IX, while the O VIII-containing gas in the upper-right corner is

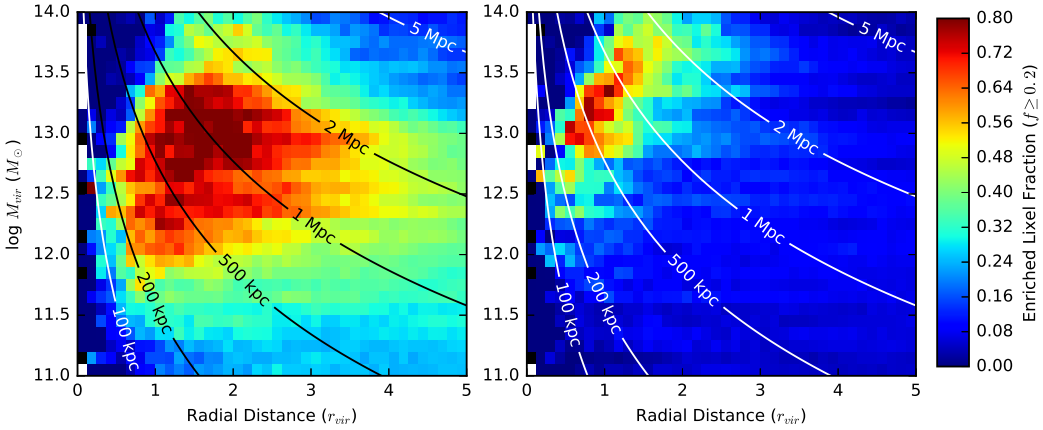

Figure 5.5 Spatial distributions of circumgalactic O VII (left) and O VIII (right) enriched gas for the CIE model as a function of halo virial mass and radial distance. The color bar indicates the fraction of lixels that are enriched in the given ion. A lixel is considered enriched in its respective ion if the ion's ionization fraction is at least 0.2. Contours on the figure show lines of constant radial distance in physical units based on the relationship from Equation 5.2 with $z = 0.2$.

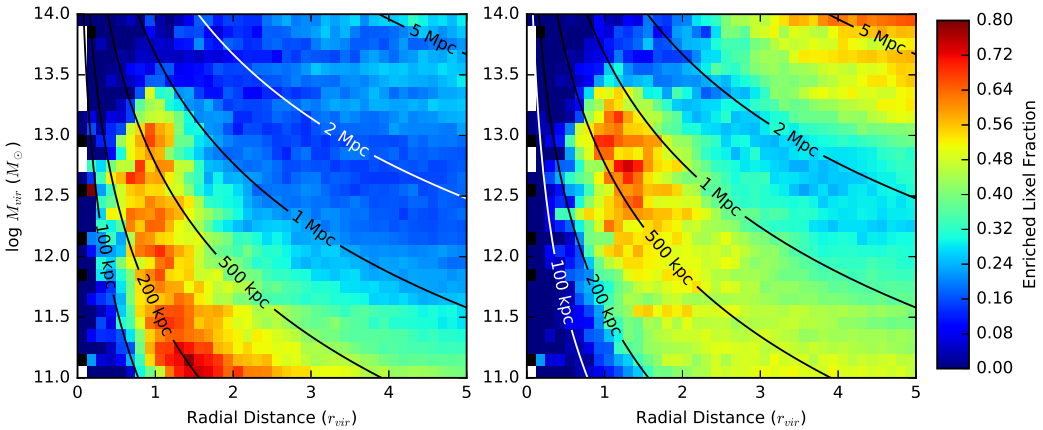

Figure 5.6 Same as Figure 5.5 but for the C+P model. The ionization fraction required for a lixel to be considered O VIII enriched has been increased to 0.4 due to the overall high O VIII fraction. O VIII is by far the dominant oxygen species in circumgalactic gas in the C+P model. The narrow diagonal band in the right panel where the O VIII abundance dips primarily contains fully ionized O IX.

photoionized gas in the cool phase of the IGM ($T < 10^4$ K).

We determine covering factors for O VII and O VIII absorbers using the methodology described in Section 5.4.2. Due to the higher ionization fractions and weaker spectral lines of the ions, we require a minimum column density of 10^{15} cm^{-2} for a halo to considered to have an associated O VII or O VIII absorption system. Figure 5.7 shows the spatial distribution of covering factors for the CIE model. Sight lines with O VII absorption are ubiquitous in this model, with covering factors above 40% for almost any choice of M_{vir} and impact parameter. This abundance extends into the IGM, with a covering factor for randomly chosen IGM locations of 6.1%. The peak O VII covering factors occur for halo masses of $12.2 \lesssim \log(M_{vir}/\mathrm{M}_\odot) \lesssim 13.2$ and impact parameters out to 3 virial radii. The distribution of O VIII absorbers in the CIE model is much smaller, with high column densities only common around halos with $M_{vir} \gtrsim 10^{12.5}\,\mathrm{M}_\odot$ and within 1.5 r_{vir}.

The situation reverses in the C+P model, shown in Figure 5.8. O VIII is still the only oxygen species with significant column densities around halos with $M_{vir} > 10^{13.5}\,\mathrm{M}_\odot$, but now it also has higher covering factor than O VII for halos down to $M_{vir} \approx 10^{12}\,\mathrm{M}_\odot$. The spatial extent of O VII in this model is limited to impact parameters of 1.5 r_{vir} or less. Significant O VIII covering factors extend out to distances of $\sim 3r_{vir}$ for virial masses in the range $12.3 \lesssim \log(M_{vir}/\mathrm{M}_\odot) \lesssim 13.0$. Both oxygen ions have modest IGM abundance, with covering factors for randomly chosen IGM locations of 1.6% and 3.3% for O VII and O VIII, respectively.

5.6 Discussion

The two ionization models considered in this paper, pure collisional ionization equilibrium and collisional + photoionization equilibrium, produce markedly different pictures of the ionization state of circumgalactic oxygen. In the CIE model, O VI is abundant in a large swath of circumgalactic gas extending beyond 3 virial radii and centered on Milky Way-mass halos. O VII is the dominant circumgalactic oxygen species, with covering factors above 40% for almost all halo masses and impact parameters. O VIII is common only in a narrow region within $2r_{vir}$ of group-mass halos.

In the C+P model, the typical ionization state of circumgalactic oxygen is much higher. The

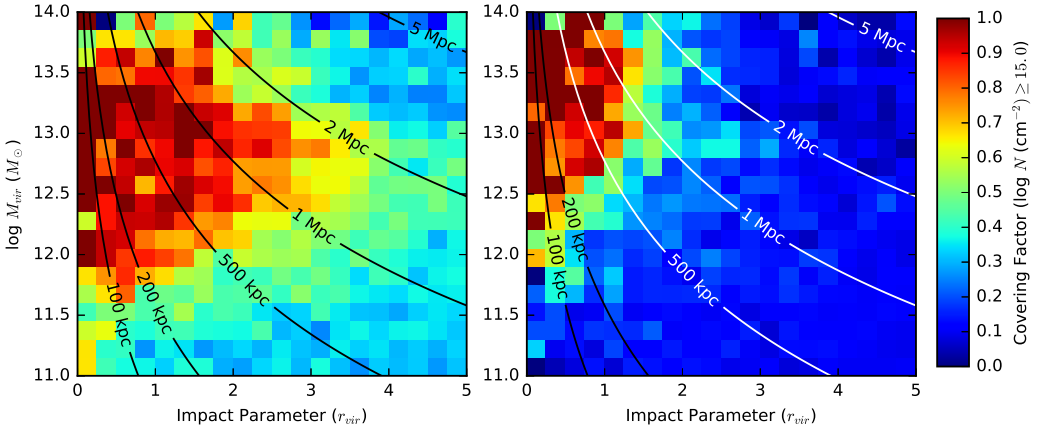

Figure 5.7 Covering factors of O VII (left) and O VIII (right) for the CIE model as a function of halo mass and impact parameter (in virial radii). The column density required for a halo to have an associated absorption system is 10^{15} cm^{-2}. Almost all circumgalactic gas exhibits high covering factors of O VII in this model. Contours on the figure show lines of constant radial distance in physical units based on the relationship from Equation 5.2 with $z = 0.2$.

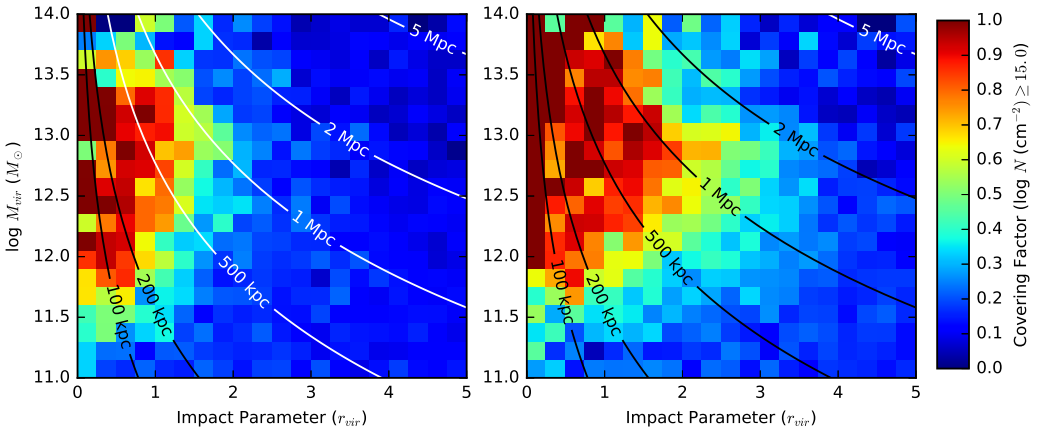

Figure 5.8 Same as Figure 5.7 but for the C+P model. The relative importance of O VII (left) and O VIII (right) has swapped between the two models. With photoionization taken into account, O VIII is now the dominant X-ray tracer of circumgalactic gas beyond the virial radius. The exact balance between O VII and O VIII depends on the intensity of the EUV and soft X-ray radiation fields.

O VI absorbers are only abundant in the range of halo masses and impact parameters probed by COS Halos. The spatial distribution of O VII is also restricted to within $2r_{vir}$ for most halo masses, extending to large distances only for halos with $M_{vir} < 10^{11.5}\,M_\odot$. Instead, O VIII is the dominant circumgalactic oxygen species. High column density O VIII absorbers are ubiquitous within the virial radii of galaxies for $M_{vir} > 10^{12}\,M_\odot$ and extend to impact parameters of $\sim 3r_{vir}$ for halos with $M_{vir} \approx 10^{12.7}\,M_\odot$.

Reconciling these competing models is a necessary step for planning future observations of circumgalactic oxygen ions. A study aimed at finding the extended O VI halos predicted by the CIE model would be fruitless if the C+P picture is correct. Similarly, attempts to detect CGM O VII and O VIII through X-ray absorption would be best focused on different halo masses and impact parameters in the two models. In the following subsections we begin this process by examining the physical processes behind each ionization model and discussing ways to determine which conditions prevail in different circumgalactic regions.

5.6.1 Collisional Ionization Equilibrium

CIE is the simpler of the two models, as it depends on only a single parameter - the gas temperature. O VI is abundant in a narrow temperature range near $10^{5.5}$ K. The large gap between the ionization energies needed to produce and destroy O VII gives it near unity abundance over a wide range of temperatures between $10^{5.6}$ and $10^{6.1}$ K. O VIII becomes the dominant oxygen species at $T \geq 10^{6.3}$ K and maintains percent level ionization fraction until 10^7 K, at which point almost all of the oxygen is fully ionized.

Figure 5.9 shows the radial temperature distribution for halos in three mass ranges centered on $10^{11.5}$ (left), $10^{12.5}$ (center), and $10^{13.5}\,M_\odot$ (right). The temperature distribution for each mass range is peaked around a central value that increases with increasing M_{vir}. For the $10^{13.5}\,M_\odot$ halos, the temperature distribution becomes dominated by cool $T \approx 10^3$ K gas beyond $3r_{vir}$. This temperature is characteristic of cold IGM gas and indicates the declining influence of the central halo at these distances. The virial theorem can be used to predict a temperature for a simple

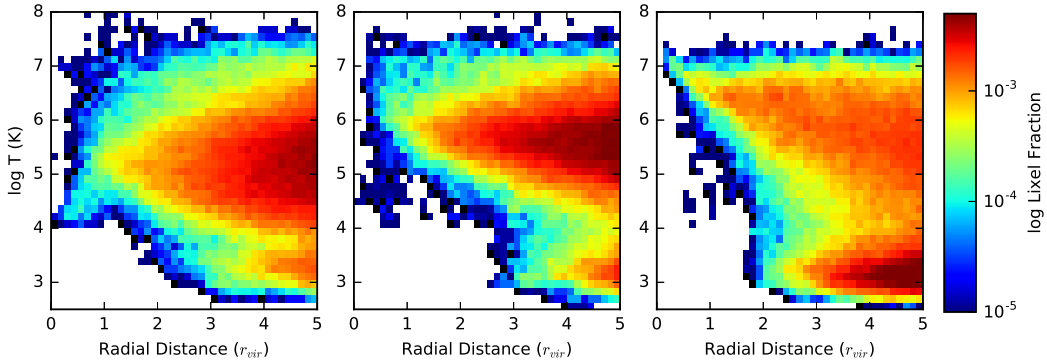

Figure 5.9 Histograms of gas temperature as a function of radial distance for dark matter halos with masses of $10^{11.5}$ (left), $10^{12.5}$ (center), and $10^{13.5}\,\mathrm{M}_\odot$ (right). Circumgalactic gas temperature increases with increasing M_{vir}. The growing abundance of cold gas at large distances from $10^{13.5}\,\mathrm{M}_\odot$ halos indicates the onset of a typical IGM temperature profile.

isothermal halo, which at $z = 0$ scales as

$$T_{vir} = (10^{5.7}\ \mathrm{K})(M_{vir}/10^{12}\,\mathrm{M}_\odot)^{2/3}. \tag{5.3}$$

This predicts virial temperatures, from low to high M_{vir}, of $10^{5.4}$, $10^{6.0}$, and $10^{6.7}$ K for the three halo mass ranges in Figure 5.9. In all three cases, the peak of the CGM temperature distribution is ~ 0.2 dex below the predicted T_{vir}. This slight decrease in temperature is likely due to the effects of metal cooling. Therefore, in our CIE model, the halo mass determines the typical temperature of circumgalactic gas, which in turn determines the oxygen ionization balance. The $T \approx 10^{5.5}$ K temperatures required for O VI are found in halos with $12.0 \lesssim \log(M_{vir}/\mathrm{M}_\odot) \lesssim 12.5$, matching the results from Section 5.4. O VII and O VIII are found primarily in higher mass halos with higher virial temperatures.

These results agree with one of the main conclusions from Oppenheimer et al. (2016). They used cosmological zoom simulations of galaxies with a range of masses to study the distribution of O VI within $\sim 2r_{vir}$. For L* galaxies and group-mass halos, they find that within the virial radius, the CGM gas temperature is well matched to the virial temperature. The halo temperature is the primary factor influencing the O VI abundance within the virial radius in their non-equilibrium C+P model.

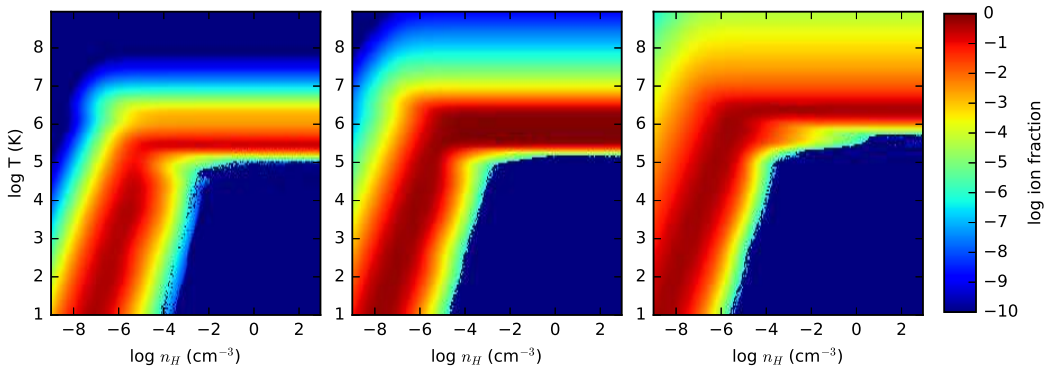

Figure 5.10 O VI (left), O VII (middle), and O VIII (right) ionization fractions as a function of hydrogen number density and gas temperature. The abundances are taken from the C+P model at $z = 0$. At high n_H where collisional processes dominate, the ionization state is only a function of T. At densities near the virial overdensity, photoionization becomes important for all three ions.

5.6.2 Collisional + Photoionization Equilibrium

The C+P model adds density (and redshift) as an additional parameter affecting the oxygen ionization balance. Collisional ionization is a two-body process with a rate dependent on both the ion and electron densities, while photoionization depends only on the ion density and the ionizing photon fluxes above the thresholds: 114 (O V), 138 (O VI), 739 (O VII), and 871 eV (O VIII). Figure 5.10 shows the C+P ionization balance for O VI (left), O VII (middle), and O VIII (right) at $z = 0$. Photoionization becomes important for O VI at densities of $n_H \lesssim 10^{-4.5}$ cm^{-3}, or photoionization parameters of $\log U \gtrsim -1.5$. This corresponds to 165 times the mean hydrogen density in the simulation, which is comparable to the virial overdensity. Within the virial radius, the O VI abundance should primarily be determined by collisional ionization, while at large radial distances photoionization becomes important. O VII and O VIII have similar thresholds for the onset of photoionization.

The C+P ionization balance in Figure 5.10 explains the shape of the ion abundance distributions in Figures 5.3 and 5.6. As density decreases, the peak abundance of a given ion shifts to lower temperatures. In the simulation, lower density corresponds to larger radial distances, while lower temperature corresponds to smaller M_{vir}. This explains the curved abundance distributions, as the abundance peaks shift to greater distances from lower mass halos. The relationship between

halo M_{vir} and ionization state from the CIE model is still present, with higher oxygen ions found around more massive halos at fixed radial distance.

The balance between collisional and photoionization also depends on redshift. Density evolves as $(1+z)^3$, and the strength of the UVB increases as $(1+z)^\gamma$ with a γ that depends on the specific UVB. The Haardt & Madau (2001) background used in the C+P model has $\gamma = 3.1$, so the transition from collisional to photoionization is largely independent of redshift. However, more recent characterizations of the UVB (e.g., Shull et al. 2015; Khaire & Srianand 2015) find $\gamma \approx 4.5$. In this case, photoionization may become important even within the virial radius at higher redshift.

5.6.3 CIE vs C+P

The C+P model includes the full effects of collisional processes. Therefore, in principle it should be superior to the model with only collisional ionization. However, the balance between collisional and photoionization in the C+P model is determined by the average densities present *on the spatial scales that are resolved in the simulation.* For our 1536^3 simulation, this corresponds to the grid cell size of $32.6h^{-1}$ kpc. If substructures exist on smaller spatial scales in the CGM and IGM with sufficient density to be collisionally dominated, then the CIE model is more appropriate in these regions.

Within r_{vir}, there is strong evidence for the existence of these substructures. Within the Milky Way's halo, dense structure is seen in the form of high-velocity clouds (HVCs). Typical HVC complexes have sizes of $\sim$ 15 kpc, with further cloud structure on smaller scales (Putman et al. 2012, and references therein). Dense molecular clouds are seen entrained in outflows from starburst galaxies such as M82 (e.g., Salas et al. 2014), at least some of which may reach the CGM. Stocke et al. (2013) used photoionization modeling of CGM absorbers to infer cloud sizes of 0.08 - 31 kpc. Zoom simulations such as those in Oppenheimer et al. (2016) also create dense substructure at distances of $\lesssim 0.5r_{vir}$. O VI may also be found in interfaces between the ambient CGM and dense clouds, which would imply even smaller spatial scales.

Direct evidence of dense substructure is lacking at distances outside of r_{vir}, but the existence

of at least some structure can be inferred. As shown in Figure 5.1, the C+P model underpredicts the abundance of O VI absorbers with $N_{OVI} \leq 10^{14}$ cm^{-2} despite the overproduction of metals. These lower column density absorbers are found in the IGM, implying the existence of at least some substructure at larger radial distances. However, the abundance of these features is poorly constrained.

One possible means of determining the distribution of density structures in the extended CGM and IGM is through higher resolution simulations. Simulations using moving-mesh techniques are particularly promising, as the spatial resolution automatically increases in dense regions. Structures on the scale of an HVC complex have gas masses on the order of 3×10^5 M$_\odot$ (Putman et al. 2012) and would require a grid cell gas mass of $\sim 10^4$ M$_\odot$ to resolve. Resolutions this high are readily attainable in galaxy-scale simulations, but are computationally challenging to extend to distances of $5r_{vir}$ around L* and above galaxies. If O VI instead exists in sub-kpc dense clouds or CGM-cloud interfaces, then the computational cost of resolving these structures over a sufficiently large volume would likely prove prohibitive.

An alternate approach is a COS Halos-like survey focused on impact parameters beyond the virial radius, where abundant O VI is predicted by the CIE model but not the C+P one. Detection of significant O VI covering factors would then indirectly indicate the existence of dense substructure. The difficulty here lies in identifying galaxies near each sight line. The area that needs to be surveyed grows as the square of the impact parameter. In addition, the number of galaxies near a given absorber grows with impact parameter as well. This makes it hard to uniquely determine galaxy-absorber pairs, a problem that will be discussed in the next section.

5.6.4 Host Halo Confusion

Uniquely matching circumgalactic O VI absorbers to galaxies is a difficult observational task. Often, multiple galaxies are close to a given absorber, complicating the identification of the source of the absorbing gas. This problem only grows worse when looking at large impact parameters as the definition of a "nearby" galaxy becomes looser. For our CIE model, 30% of the O VI absorbers

with $N_{OVI} > 10^{14}$ cm^{-2} have at least two halos within $3r_{vir}$. Correctly matching these ambiguous absorbers to their source halos is necessary for an accurate picture of the circumgalactic O VI distribution. Observers typically assume that an absorber is associated with the nearest galaxy, using the impact parameter either in physical units or scaled to the galaxy's virial radius. We test both methods on our simulated absorbers and compare the results. In addition, we implement a third method that uses our simulated covering factors as a prior. For each halo near a given absorber, we use the halo's virial mass and impact parameter to determine the associated covering factor. This covering factor, normalized by the sum over all nearby halos, is taken as the probability of the absorber being associated with that specific halo.

We applied all three methods to each ambiguous absorber and tested how often the methods agreed. The two different metrics for the nearest halo (physical and scaled distance) agreed 54% of the time. The worst agreement was between the physical impact parameter and covering factor weighting methods. The most probable associated halo in the covering-factor method was only the physically closest halo for 38% of the absorbers. The scaled impact parameter method agreed with the covering factor weighting 69% of the time. All of these agreement percentages are low enough that the choice of method is clearly important.

Figure 5.11 compares the distribution of M_{vir} for the halos associated with O VI absorbers using each disambiguation method. Two different distributions are plotted for the covering-factor method. The first takes the mass of the halo with the highest probability of being associated with the absorber (blue dashed), while the second weights the virial mass of each associated halo by its respective probability (cyan). Determining halo-absorber associations by physical impact parameter unrealistically favors low mass halos. Both other methods favor Milky Way-mass halos, with the most probable halos from the covering factor method producing a much narrower distribution.

The probability-weighted distribution for the covering factor method likely overestimates the importance of low mass halos. The left panel of Figure 5.4 shows covering factors of $\sim 20\%$ even for impact parameters beyond $4r_{vir}$ around low mass halos. These O VI absorbers are unlikely to be directly associated with the halo; instead they arise from dense regions of the nearby IGM.

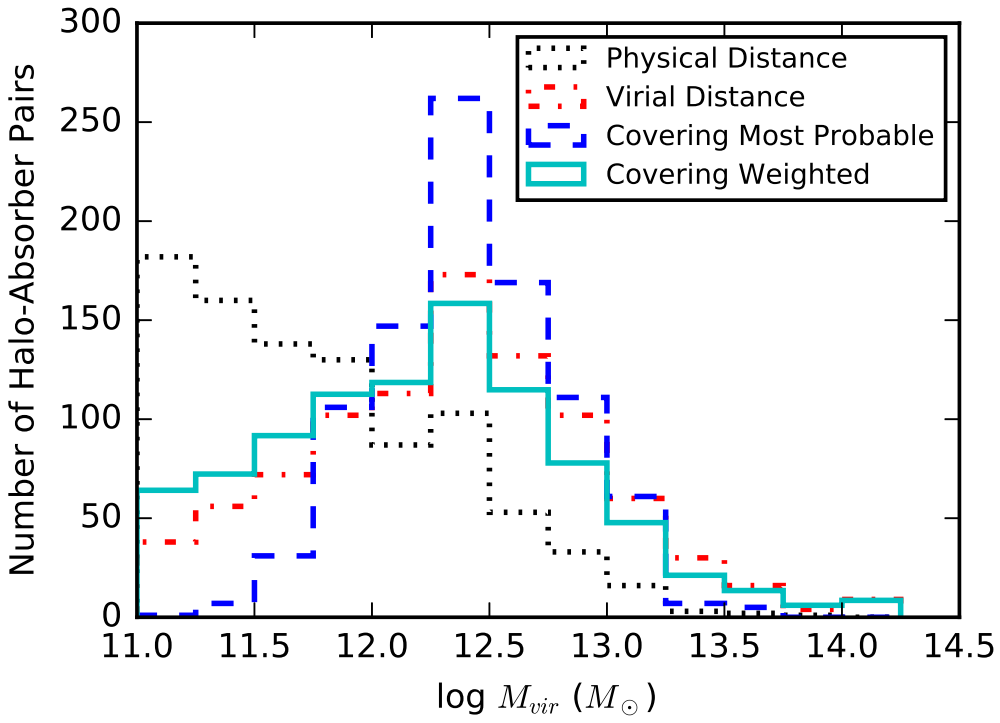

Figure 5.11 Histogram of M_{vir} for the halos associated with CIE O VI "ambiguous absorbers" using each method of matching absorbers to halos. The black dotted and red dash-dotted histograms were made by matching absorbers to the closest halo measuring by physical impact parameter and impact parameter scaled to the halo's virial radius, respectively. The blue dashed histogram uses the halo with the highest probability of being associated with a given absorber from our covering factor method. The cyan histogram instead uses the virial masses of all nearby halos, weighted by their respective probabilities.

The covering factor method could be adapted to account for this by taking the mean covering factor at large impact parameters (4-5r_{vir}) as the probability of an absorber being associated with the IGM rather than a specific halo. This value could then be subtracted off from the covering factors before calculating the probabilities for each halo. The effect of this would be to increase the likelihood of absorbers being associated with Milky Way-mass halos, while also adding a probability of the absorber being unassociated with any halos, something missing from the other methods. The resolution of the simulation in this paper is too low, and the difference between the two ionization models too large, for our covering factors to be directly used to constrain observations. However, this method could easily be used with a higher resolution simulation to interpret future observational studies.

5.7 Conclusions

We used a large, uniform resolution cosmological simulation to study the distribution of highly ionized oxygen in circumgalactic gas. Using both collisional ionization equilibrium and collisional + photoionization models, we measured the ionization fractions of O VI, O VII, and O VIII around dark matter halos with masses from 10^{11} to 10^{14} $M_{\odot}$ and radial distances out to $5r_{vir}$. We then converted these abundances to simulated absorber covering factors using a method modeled on the COS Halos observations. We analyzed how the differences in our CIE and C+P ionization models arose from the physical assumptions underlying them. Our main results are the following:

(1) In CIE, large O VI column densities are present out to impact parameters of $4r_{vir}$ around Milky Way-mass galaxies. However, helium-like O VII is the dominant ion in circumgalactic gas.

(2) With our C+P model, O VI absorption is limited to within the virial radius. The dominant circumgalactic oxygen species is O VIII, with some gas fully ionized to O IX.

(3) Within the virial radius, collisional processes dominate and the oxygen ionization state is determined by the halo's virial temperature (with some metal cooling). Higher mass halos

contain higher ionization states.

(4) Beyond the virial radius, the prevailing ionization model depends on the existence of dense substructure or CGM-cloud interfaces below the $32.6h^{-1}$ kpc resolution of the simulation. Either higher resolution simulations or observations of O VI absorption at impact parameters of 2 - $4r_{vir}$ will be needed to determine the true ionization state of the gas.

(5) Simulated O VI covering factors can be used as a prior to more accurately match O VI absorbers to associated galaxies in crowded environments.

Acknowledgements

The authors thank Devin Silvia for assistance with creating the simulated light rays, which were created using NSF BlueWaters grants PRAC_gka and GLCPC_jth. The authors would additionally like to thank Ben Oppenheimer, James Green, Britton Smith, and Evan Tilton for helpful comments. This work was supported by HST archival theory grant HST-AR-14314.01-A.

Chapter 6

Toward a Greater Understanding of Intergalactic Ionization

In the time since the initial publication of the work in Chapter 3, a consensus has begun to develop for the intensity of the low-redshift UVB. Gaikwad et al. (2017) used a GADGET-2 simulation, post-processed to include the effects of the UVB, to determine the hydrogen photoionization rate $\Gamma_{\rm H}$ for $z < 0.4$ by comparing the probability density function and power spectrum of Lyα forest fluxes from their simulation to the spectra from Danforth et al. (2016). The values of $\Gamma_{\rm H}$ that they obtained are in good agreement with the results from Chapter 3 (see their Figure 16 for a direct comparison). In addition, recently updated AGN UV luminosity functions from Croom et al. (2009) and Palanque-Delabrouille et al. (2013) have increased the estimated ionizing photon flux from AGN by a factor of two compared to the Haardt & Madau (2012) UVB. New UVB models incorporating these updated AGN luminosity functions (Khaire & Srianand 2015; Madau & Haardt 2015) match our derived $\Gamma_{\rm H}$ values without requiring large LyC escape fractions or more exotic ionizing sources such as TeV blazars.

However, uncertainties in the nature of the low-redshift UVB remain, including the explanation for the steep slope of the simulated column-density distribution discussed in Chapter 4. More generally, the current paradigm for creating UVB models is problematic. Existing UVB models are derived from a small number of (often private or closed-source) one-dimensional radiative transfer codes, and are only occasionally updated to incorporate new observations. The accuracy of these codes is unclear, and the dependence of the resulting models on their redshift-evolving input parameters, including the quasar luminosity function and slope, the LyC escape fraction, and the

distribution of neutral hydrogen in the IGM and CGM, is often poorly understood. The recent use of cosmological simulations to constrain properties of the UVB, started by Kollmeier et al. (2014) and continued in this work, opens the possibility of a new, more empirical approach to developing UVB models. Instead of using existing prescriptions for the UVB, simulations would be run for an entire grid of potential UVB models. The models would be generated from an open-source code and would cover the full range of potential values for the various input parameters. Comparing the outputs of the simulation grid to observations of the Lyα forest would lead to both a statistically-robust model of the UVB and constraints on the population of ionizing sources.

Such a project is already possible with current computational resources. As demonstrated in Figure 3.4, a relatively low-resolution 512^3 simulation grid is sufficient to achieve numerical convergence of the Lyα column density distribution for a $50h^{-1}$ Mpc box size. Such a simulation requires $\sim 10^4$ CPU hours on a modern supercomputer. This means that a grid of hundreds of simulations can be run on a reasonable ($< 10^7$ CPU hour) allocation. The greatest difficulty comes from understanding the effects of other aspects of the simulation on the results. The source of the differences between the Kollmeier et al. (2014) simulations and ours is still unclear, and the steep slope of the column density distribution in our simulations may arise from issues unrelated to the UVB. Therefore, the first step of this project would be a code comparison similar to that of Iliev et al. (2006, 2009) for radiative transfer codes but aimed at understanding the differences in how simulations model the UVB and the Lyα forest. The results of this code comparison would be used to determine the best code and analysis technique for simulating the full grid of UVB models.

Some possibilities for future work to improve our understanding of the distribution of circumgalactic oxygen ions have already been discussed in Section 5.6. On the simulation side of the equation, the need for higher resolution in the CGM is clear. This can be achieved through moderate levels of adaptive mesh refinement (AMR) in regions at or above the virial overdensity. A simulation similar to the one from Chapter 5 but with three levels of AMR would provide a maximum spatial resolution of $4.1h^{-1}$ kpc. Although this resolution would still not be sufficient to resolve small dense clouds or CGM-cloud interfaces, it should significantly improve the accuracy

of the collisional + photoionizaton equilibrium model and remove the need to consider a purely collisional ionization equilibrium alternative as an additional limiting case.

Observationally, a COS-Halos-like survey aimed at galaxy impact parameters out to 300 – 500 kpc would be extremely beneficial. The results of both observational studies (Tumlinson et al. 2011; Stocke et al. 2014; Keeney et al. 2017) and cosmological simulations (Oppenheimer et al. 2016 and this work) indicate that there are likely large column densities ($> 10^{14}$ cm^{-2}) of O VI extending out to distances of several virial radii around Milky Way-mass galaxies. Determining the distribution and maximum spatial extent of this oxygen-enriched gas would greatly improve our understanding of how effectively galactic outflows influence the IGM. With *HST* nearing the end of its life and no new large UV telescopes on the horizon, time may be running out for such a survey. However, our collisional + photoionization equilibrium model also predicts large amounts of circumgalactic O VIII with even greater spatial extent. Although detecting most of this gas is likely not possible with *Chandra* or *XMM-Newton*, it should be well within the capabilities of future X-ray missions such as *ATHENA*.

Bibliography

Abel, T., Anninos, P., Zhang, Y., & Norman, M. L. 1997, NewA, 2, 181

Anninos, P., Zhang, Y., Abel, T., & Norman, M. L. 1997, NewA, 2, 209

Baes, M., Verstappen, J., De Looze, I., et al. 2011, ApJS, 196, 22

Balogh, M. L., Pearce, F. R., Bower, R. G., & Kay, S. T. 2001, MNRAS, 326, 1228

Bautista, M. A., & Kallman, T. R. 2001, ApJS, 134, 139

Behroozi, P. S., Wechsler, R. H., & Conroy, C. 2013a, ApJ, 770, 57

Behroozi, P. S., Wechsler, R. H., & Wu, H.-Y. 2013b, ApJ, 762, 109

Benson, A., Venkatesan, A., & Shull, J. M. 2013, ApJ, 770, 76

Boera, E., Murphy, M. T., Becker, G. D., & Bolton, J. S. 2014, MNRAS, 441, 1916

Bolton, J. S., Becker, G. D., Haehnelt, M. G., & Viel, M. 2014, MNRAS, 438, 2499

Bonamente, M., Nevalainen, J., Tilton, E., et al. 2016, MNRAS, 457, 4236

Bondi, H. 1952, MNRAS, 112, 195

Bondi, H., & Hoyle, F. 1944, MNRAS, 104, 273

Bordoloi, R., Tumlinson, J., Werk, J. K., et al. 2014, ApJ, 796, 136

Bregman, J. N. 2007, ARA&A, 45, 221

Bridge, C. R., Teplitz, H. I., Siana, B., et al. 2010, ApJ, 720, 465

Bristow, P. D., & Phillipps, S. 1994, MNRAS, 267, 13

Bryan, G. L., & Norman, M. L. 1998, ApJ, 495, 80

Bryan, G. L., Norman, M. L., Stone, J. M., Cen, R., & Ostriker, J. P. 1995, Computer Physics Communications, 89, 149

Bryan, G. L., Norman, M. L., O'Shea, B. W., et al. 2014, ApJS, 211, 19

Camps, P., & Baes, M. 2015, Astronomy and Computing, 9, 20

Cantalupo, S., Arrigoni-Battaia, F., Prochaska, J. X., Hennawi, J. F., & Madau, P. 2014, Nature, 506, 63

Cen, R., & Kimm, T. 2015, ApJL, 801, L25

Cen, R., & Ostriker, J. P. 1992, ApJL, 399, L113

Cen, R., & Safarzadeh, M. 2016, ArXiv e-prints, arXiv:1609.03583

Chevalier, R. A., & Clegg, A. W. 1985, Nature, 317, 44

Cicone, C., Maiolino, R., Sturm, E., et al. 2014, A&A, 562, A21

Colella, P., & Woodward, P. R. 1984, Journal of Computational Physics, 54, 174

Croom, S. M., Richards, G. T., Shanks, T., et al. 2009, MNRAS, 399, 1755

Cyburt, R. H., Fields, B. D., Olive, K. A., & Yeh, T.-H. 2016, Rev. Mod. Phys., 88, 015004

Dalla Vecchia, C., & Schaye, J. 2012, MNRAS, 426, 140

Danforth, C. W., & Shull, J. M. 2005, ApJ, 624, 555

—. 2008, ApJ, 679, 194

Danforth, C. W., Stocke, J. T., & Shull, J. M. 2010, ApJ, 710, 613

Danforth, C. W., Keeney, B. A., Tilton, E. M., et al. 2016, ApJ, 817, 111

Davé, R., Oppenheimer, B. D., Katz, N., Kollmeier, J. A., & Weinberg, D. H. 2010, MNRAS, 408, 2051

Davis, M., Efstathiou, G., Frenk, C. S., & White, S. D. M. 1985, ApJ, 292, 371

Dekel, A., & Birnboim, Y. 2006, MNRAS, 368, 2

Dekel, A., & Silk, J. 1986, ApJ, 303, 39

Di Matteo, T., Colberg, J., Springel, V., Hernquist, L., & Sijacki, D. 2008, ApJ, 676, 33

Dove, J. B., & Shull, J. M. 1994, ApJ, 430, 222

Egan, H., Smith, B. D., O'Shea, B. W., & Shull, J. M. 2014, ApJ, 791, 64

Eisenstein, D. J., & Hu, W. 1999, ApJ, 511, 5

Eisenstein, D. J., & Hut, P. 1998, ApJ, 498, 137

Fang, T., Buote, D. A., Humphrey, P. J., et al. 2010, ApJ, 714, 1715

Faucher-Giguère, C.-A., Lidz, A., Zaldarriaga, M., & Hernquist, L. 2009, ApJ, 703, 1416

Ferland, G. J., Porter, R. L., van Hoof, P. A. M., et al. 2013, RMxAA, 49, 137

Ford, A. B., Oppenheimer, B. D., Davé, R., et al. 2013, MNRAS, 432, 89

Fryxell, B., Olson, K., Ricker, P., et al. 2000, ApJS, 131, 273

Fukugita, M., Hogan, C. J., & Peebles, P. J. E. 1998, ApJ, 503, 518

Gaikwad, P., Khaire, V., Choudhury, T. R., & Srianand, R. 2017, MNRAS, 466, 838

Gehrels, N. 1986, ApJ, 303, 336

Genzel, R., Tacconi, L. J., Lutz, D., et al. 2015, ApJ, 800, 20

Green, J. C., Froning, C. S., Osterman, S., et al. 2012, ApJ, 744, 60

Gupta, A., Mathur, S., Krongold, Y., Nicastro, F., & Galeazzi, M. 2012, ApJL, 756, L8

Gutcke, T. A., Stinson, G. S., Macciò, A. V., Wang, L., & Dutton, A. A. 2017, MNRAS, 464, 2796

Haardt, F., & Madau, P. 1996, ApJ, 461, 20

Haardt, F., & Madau, P. 2001, in Clusters of Galaxies and the High Redshift Universe Observed in X-rays, ed. D. M. Neumann & J. T. V. Tran

—. 2012, ApJ, 746, 125

Hahn, O., & Abel, T. 2011, MNRAS, 415, 2101

Heckman, T. M., Borthakur, S., Overzier, R., et al. 2011, ApJ, 730, 5

Hinshaw, G., Larson, D., Komatsu, E., et al. 2013, ApJS, 208, 19

Hockney, R. W., & Eastwood, J. W. 1988, Computer simulation using particles

Hopkins, P. F. 2015, MNRAS, 450, 53

Hopkins, P. F., Kereš, D., Oñorbe, J., et al. 2014, MNRAS, 445, 581

Hopkins, P. F., Richards, G. T., & Hernquist, L. 2007, ApJ, 654, 731

Hoyle, F., & Lyttleton, R. A. 1939, Proceedings of the Cambridge Philosophical Society, 35, 405

Iliev, I. T., Ciardi, B., Alvarez, M. A., et al. 2006, MNRAS, 371, 1057

Iliev, I. T., Whalen, D., Mellema, G., et al. 2009, MNRAS, 400, 1283

Keeney, B. A., Stocke, J. T., Rosenberg, J. L., et al. 2013, ApJ, 765, 27

Keeney, B. A., Stocke, J. T., Danforth, C. W., et al. 2017, ApJ, submitted

Kennicutt, Jr., R. C. 1998, ApJ, 498, 541

Kereš, D., Katz, N., Weinberg, D. H., & Davé, R. 2005, MNRAS, 363, 2

Khaire, V., & Srianand, R. 2015, MNRAS, 451, L30

Kim, J.-h., Abel, T., Agertz, O., et al. 2014, ApJS, 210, 14

Kirkman, D., Tytler, D., Lubin, D., & Charlton, J. 2007, MNRAS, 376, 1227

Kollmeier, J. A., Weinberg, D. H., Oppenheimer, B. D., et al. 2014, ApJL, 789, L32

Komatsu, E., Smith, K. M., Dunkley, J., et al. 2011, ApJS, 192, 18

Kravtsov, A. V. 1999, PhD thesis, NEW MEXICO STATE UNIVERSITY

Larson, R. B., Tinsley, B. M., & Caldwell, C. N. 1980, ApJ, 237, 692

Lehner, N., Savage, B. D., Richter, P., et al. 2007, ApJ, 658, 680

Leitherer, C., Hernandez, S., Lee, J. C., & Oey, M. S. 2016, ApJ, 823, 64

Leitherer, C., Schaerer, D., Goldader, J. D., et al. 1999, ApJS, 123, 3

Leroy, A. K., Walter, F., Martini, P., et al. 2015, ApJ, 814, 83

Lusso, E., Worseck, G., Hennawi, J. F., et al. 2015, MNRAS, 449, 4204

Lynds, C. R., & Sandage, A. R. 1963, AJ, 68, 284

Ma, X., Kasen, D., Hopkins, P. F., et al. 2015, MNRAS, 453, 960

Mac Low, M.-M., McCray, R., & Norman, M. L. 1989, ApJ, 337, 141

Madau, P., & Haardt, F. 2015, ApJL, 813, L8

McCray, R., & Snow, Jr., T. P. 1979, ARA&A, 17, 213

Monaghan, J. J., & Gingold, R. A. 1983, Journal of Computational Physics, 52, 374

Mostardi, R. E., Shapley, A. E., Nestor, D. B., et al. 2013, ApJ, 779, 65

Nestor, D. B., Shapley, A. E., Kornei, K. A., Steidel, C. C., & Siana, B. 2013, ApJ, 765, 47

Nicastro, F., Zezas, A., Drake, J., et al. 2002, ApJ, 573, 157

Nicastro, F., Mathur, S., Elvis, M., et al. 2005, ApJ, 629, 700

Nicastro, F., Elvis, M., Krongold, Y., et al. 2013, ApJ, 769, 90

Oppenheimer, B. D., & Davé, R. 2006, MNRAS, 373, 1265

—. 2009, MNRAS, 395, 1875

Oppenheimer, B. D., Davé, R., Katz, N., Kollmeier, J. A., & Weinberg, D. H. 2012, MNRAS, 420, 829

Oppenheimer, B. D., Crain, R. A., Schaye, J., et al. 2016, MNRAS, 460, 2157

Palanque-Delabrouille, N., Magneville, C., Yèche, C., et al. 2013, A&A, 551, A29

Peeples, M. S., Werk, J. K., Tumlinson, J., et al. 2014, ApJ, 786, 54

Penton, S. V., Shull, J. M., & Stocke, J. T. 2000, ApJ, 544, 150

Penton, S. V., Stocke, J. T., & Shull, J. M. 2004, ApJS, 152, 29

Persic, M., & Salucci, P. 1992, MNRAS, 258, 14P

Planck Collaboration, Ade, P. A. R., Aghanim, N., et al. 2014, A&A, 571, A16

—. 2016, A&A, 594, A13

Prochaska, J. X., Weiner, B., Chen, H.-W., Mulchaey, J., & Cooksey, K. 2011, ApJ, 740, 91

Puchwein, E., Bolton, J. S., Haehnelt, M. G., et al. 2015, MNRAS, 450, 4081

Puchwein, E., Pfrommer, C., Springel, V., Broderick, A. E., & Chang, P. 2012, MNRAS, 423, 149

Putman, M. E., Peek, J. E. G., & Joung, M. R. 2012, ARA&A, 50, 491

Ribaudo, J., Lehner, N., & Howk, J. C. 2011, ApJ, 736, 42

Saff, E. B., & Kuijlaars, A. B. J. 1997, Math. Intel., 19, 5

Saintonge, A., Catinella, B., Cortese, L., et al. 2016, MNRAS, 462, 1749

Salas, P., Galaz, G., Salter, D., et al. 2014, ApJ, 797, 134

Savage, B. D., Kim, T.-S., Wakker, B. P., et al. 2014, ApJS, 212, 8

Schaye, J. 2001, ApJ, 559, 507

Schaye, J., & Dalla Vecchia, C. 2008, MNRAS, 383, 1210

Schaye, J., Dalla Vecchia, C., Booth, C. M., et al. 2010, MNRAS, 402, 1536

Scott, J. E., Kriss, G. A., Brotherton, M., et al. 2004, ApJ, 615, 135

SDSS Collaboration, Albareti, F. D., Allende Prieto, C., et al. 2016, ArXiv e-prints, arXiv:1608.02013

Sembach, K. R., Tripp, T. M., Savage, B. D., & Richter, P. 2004, ApJS, 155, 351

Shapiro, P. R., & Field, G. B. 1976, ApJ, 205, 762

Shapley, A. E., Steidel, C. C., Pettini, M., Adelberger, K. L., & Erb, D. K. 2006, ApJ, 651, 688

Shull, J. M. 2003, in Astrophysics and Space Science Library, Vol. 281, The IGM/Galaxy Connection. The Distribution of Baryons at z=0, ed. J. L. Rosenberg & M. E. Putman, 1

Shull, J. M. 2014, ApJ, 784, 142

Shull, J. M., Danforth, C. W., & Tilton, E. M. 2014, ApJ, 796, 49

Shull, J. M., Harness, A., Trenti, M., & Smith, B. D. 2012a, ApJ, 747, 100

Shull, J. M., Moloney, J., Danforth, C. W., & Tilton, E. M. 2015, ApJ, 811, 3

Shull, J. M., Roberts, D., Giroux, M. L., Penton, S. V., & Fardal, M. A. 1999, AJ, 118, 1450

Shull, J. M., Smith, B. D., & Danforth, C. W. 2012b, ApJ, 759, 23

Shull, J. M., Stevans, M., & Danforth, C. W. 2012c, ApJ, 752, 162

Siana, B., Teplitz, H. I., Ferguson, H. C., et al. 2010, ApJ, 723, 241

Sijacki, D., Springel, V., Di Matteo, T., & Hernquist, L. 2007, MNRAS, 380, 877

Smith, B., Sigurdsson, S., & Abel, T. 2008, MNRAS, 385, 1443

Smith, B. D., Hallman, E. J., Shull, J. M., & O'Shea, B. W. 2011, ApJ, 731, 6

Springel, V. 2005, MNRAS, 364, 1105

—. 2010, MNRAS, 401, 791

Springel, V., & Hernquist, L. 2003, MNRAS, 339, 289

Springel, V., White, S. D. M., Tormen, G., & Kauffmann, G. 2001, MNRAS, 328, 726

Stevans, M. L., Shull, J. M., Danforth, C. W., & Tilton, E. M. 2014, ApJ, 794, 75

Stocke, J. T., Keeney, B. A., Danforth, C. W., et al. 2013, ApJ, 763, 148

Stocke, J. T., Penton, S. V., Danforth, C. W., et al. 2006, ApJ, 641, 217

Stocke, J. T., Keeney, B. A., Danforth, C. W., et al. 2014, ApJ, 791, 128

Strickland, D. K., & Heckman, T. M. 2009, ApJ, 697, 2030

Suresh, J., Rubin, K. H. R., Kannan, R., et al. 2015, ArXiv e-prints, arXiv:1511.00687

Sutherland, R. S., & Dopita, M. A. 1993, ApJS, 88, 253

Telfer, R. C., Zheng, W., Kriss, G. A., & Davidsen, A. F. 2002, ApJ, 565, 773

Tepper-García, T., Richter, P., Schaye, J., et al. 2012, MNRAS, 425, 1640

Teyssier, R. 2002, A&A, 385, 337

Tilton, E. M., Danforth, C. W., Shull, J. M., & Ross, T. L. 2012, ApJ, 759, 112

Tilton, E. M., Stevans, M. L., Shull, J. M., & Danforth, C. W. 2016, ApJ, 817, 56

Tombesi, F., Sambruna, R. M., Reeves, J. N., et al. 2010, ApJ, 719, 700

Topping, M. W., & Shull, J. M. 2015, ApJ, 800, 97

Toro, E. F., Spruce, M., & Speares, W. 1994, Shock Waves, 4, 25

Tripp, T. M., Sembach, K. R., Bowen, D. V., et al. 2008, ApJS, 177, 39

Tumlinson, J., Thom, C., Werk, J. K., et al. 2011, Science, 334, 948

—. 2013, ApJ, 777, 59

Turk, M. J., Smith, B. D., Oishi, J. S., et al. 2011, ApJS, 192, 9

Viel, M., Haehnelt, M. G., Bolton, J. S., et al. 2016, ArXiv e-prints, arXiv:1610.02046

Volonteri, M. 2010, A&A Rv, 18, 279

Wadsley, J. W., Stadel, J., & Quinn, T. 2004, NewA, 9, 137

Watson, M. G., Stanger, V., & Griffiths, R. E. 1984, ApJ, 286, 144

Werk, J. K., Prochaska, J. X., Thom, C., et al. 2012, ApJS, 198, 3

—. 2013, ApJS, 204, 17

Werk, J. K., Prochaska, J. X., Tumlinson, J., et al. 2014, ApJ, 792, 8

Werk, J. K., Prochaska, J. X., Cantalupo, S., et al. 2016, ApJ, 833, 54

Westmoquette, M. S., Smith, L. J., Gallagher, III, J. S., et al. 2009, ApJ, 696, 192

Wiersma, R. P. C., Schaye, J., Dalla Vecchia, C., et al. 2010, MNRAS, 409, 132

Xu, H., Wise, J. H., & Norman, M. L. 2013, ApJ, 773, 83

Yao, Y., Shull, J. M., Wang, Q. D., & Cash, W. 2012, ApJ, 746, 166

Appendix A

Dependence of Lyα Absorbers on Ionization Rate

The intergalactic Lyα absorbers are thought to arise as fluctuations in dark-matter confined clumps or filaments. Modeling their distribution and frequency throughout intergalactic space depends on the cosmological evolution of this gas, coupled to calculations of the "neutral fraction", $f_{\rm HI} \equiv n_{\rm HI}/n_H$, produced by the balance of photoionization and radiative recombination. These physical processes can be modeled by N-body hydrodynamic simulations, but one can also derive their general behavior through simple analytic arguments (Shull et al. 2012b). Here, we describe the key assumptions and parameters to illustrate how the baryon density and hydrogen ionization rate $\Gamma_{\rm H}$ can be inferred from observations of the H I column density distribution and the frequency, $d\mathcal{N}/dz$, of absorbers per unit redshift.

We assume a distribution of IGM absorbers with constant co-moving space density, $\phi(z) = \phi_0(1+z)^3$, and constant cross section πp^2. We adopt a cosmological relation between proper distance and redshift, $d\ell/dz = c(dt/dz) = [c/(1+z)H(z)]$, where the Hubble parameter at redshift z in a flat ΛCDM cosmology is $H(z) = H_0[\Omega_m(1+z)^3 + \Omega_\Lambda]^{1/2}$. In this model, the frequency of absorbers is $d\mathcal{N}/dz = [c/(1+z)H(z)]\,\pi p^2\,\phi(z)$. The internal density distributions of the absorbers are approximated as singular isothermal spheres, and the IGM baryon density and H I fractions follow from photoionization models that translate the observed H I to total hydrogen. To compare with observations, we integrate through the cloud along a chord at impact parameter $p = (100\ {\rm kpc})p_{100}$ of the AGN sight line through the absorber. We adopt a 100-kpc characteristic scale length of Lyα absorbers, normalized at fiducial H I column density $N_{\rm HI} = (10^{14}\ {\rm cm}^{-2})N_{14}$. Because most

Lyα-forest absorbers are low density and optically thin in their Lyman lines, we use a case-A hydrogen recombination rate coefficient, $\alpha_{\rm H}^{(A)} = (4.09 \times 10^{-13}\ {\rm cm^3\ s^{-1}}) T_4^{-0.726}$, scaled to temperature $T = (10^4\ {\rm K}) T_4$. For nearly fully ionized H and He, with helium abundance $y = n_{\rm He}/n_{\rm H} \approx 1/12$ by number, we adopt electron density $n_e = (1 + 2y) n_{\rm H}$ and mean baryon mass per hydrogen $\mu_b = (1 + 4y) m_H$.

The co-moving baryon mass density of Lyα absorbers of column density $N_{\rm HI}$, probed at impact parameter p, is the product of absorber space density,

$$\phi(z) = \frac{(d\mathcal{N}/dz) H(z) (1+z)}{(\pi p^2)\, c} \quad , \tag{A.1}$$

and absorber mass

$$M_b(p) = 4\pi \mu_b\, p^{5/2} \left[\frac{2\, \Gamma_{\rm H}(z)\, N_{\rm HI}(p)}{\pi (1+2y) \alpha_H^{(A)}} \right]^{1/2} \quad . \tag{A.2}$$

The co-moving mass density, $\rho_b = \phi_0 M_b \propto [p\, N_{\rm HI}\, \Gamma_{\rm HI}]^{1/2} (d\mathcal{N}/dz)$, is then integrated over the distribution in H I column density. We normalize ρ_b to the closure parameter, $\Omega_b^{\rm (HI)} = \rho_b/\rho_{\rm cr}$ at redshift $z = 0$, relative to critical density $\rho_{\rm cr} = (3H_0^2/8\pi G)$. Because our *HST* surveys extend to $z \approx 0.5$, we must include the cosmological evolution in $H(z)$, $\phi(z)$, and $\Gamma_{\rm H}(z)$. Before introducing these corrections, we outline the method at low redshift, for which the Euclidean calculation gives

$$\begin{aligned} \Omega_b^{\rm (HI)} &= \left[\frac{32 (2\pi)^{1/2}}{3} \right] \left(\frac{d\mathcal{N}}{dz} \right) \left(\frac{G \mu_b}{c H_0} \right) \left[\frac{p\, N_{\rm HI}\, \Gamma_{\rm H}}{\alpha_{\rm H}^{(A)} (1+2y)} \right]^{1/2} \\ &= (7.1 \times 10^{-3}) \left[\frac{d\mathcal{N}/dz}{100} \right] \left[p_{100}\, N_{14} \left(\frac{\Gamma_{\rm H}}{\Gamma_{\rm HM12}} \right) \right]^{1/2} h_{70}^{-1}\, T_4^{0.363} \, . \end{aligned} \tag{A.3}$$

Here, we normalize the Lyα frequency to a characteristic value $d\mathcal{N}/dz = 100$ and scale $\Gamma_{\rm H}$ to the HM12 ionization rate, $\Gamma_{\rm HM12} = (2.28 \times 10^{-14}\ {\rm s^{-1}})(1+z)^{4.4}$, which we fitted over the range $0 < z < 0.7$. The weak temperature dependence comes from the recombination rate coefficient. The coefficient (7.1×10^{-3}) corresponds to $\sim 15\%$ of the cosmological baryon fraction, $\Omega_b = 0.0463 \pm 0.00093$ (Hinshaw et al. 2013; Planck Collaboration et al. 2014). For fixed baryon density $\Omega_b^{\rm (HI)}$ in the Lyα forest, the *observed* frequency of Lyα absorbers, $d\mathcal{N}/dz \propto \Gamma_{\rm H}^{-1/2}$, scaling as the inverse square root of the ionizing background.

Our *HST* surveys of Lyα absorbers provide accurate values of $\Omega_b^{(\rm HI)}$, based on an integration over the column-density distribution. After inserting the redshift corrections to $\phi(z)$, $H(z)$, and $\Gamma_{\rm H}(z)$, we derive a general expression for $\Omega_b^{(\rm HI)}$,

$$\begin{aligned} \Omega_b^{(\rm HI)} &= (7.1 \times 10^{-5}) \left[\frac{\Gamma_{\rm H}}{\Gamma_{\rm HM12}}\right]^{1/2} \left[\frac{H(z)}{H_0}\right]^{1/2} h_{70}^{-1} p_{100}^{1/2}\, T_4^{0.363} (1+z)^{0.2} \\ &\times \int_{N_{\rm min}}^{N_{\rm max}} \frac{d^2\mathcal{N}}{d\log(N_{\rm HI}) dz}\, N_{14}^{1/2}\, d(\log\, N_{\rm HI})\ . \end{aligned} \tag{A.4}$$

Owing to the n_H^2 dependence of neutral fraction in photoionization equilibrium, the factor $\Gamma_{\rm H}(z)$ enters Equations (8) and (10) as the square root, with a $(1+z)^{2.2}$ dependence that nearly balances the $(1+z)^2$ from the cosmological ratio $[\phi(z)/(1+z)]$ in Equation (7). Two recent *HST* surveys (Tilton et al. 2012; Danforth et al. 2016) probed Lyα absorbers out to $z \approx 0.47$ and found that between 24% and 30% of the baryons reside in the low-z Lyα forest. Equation (10) is consistent with those estimates, particularly with our recommended factor-of-two increase in ionizing background, $\Gamma_{\rm H}(z) = (4.6 \times 10^{-14}\ {\rm s}^{-1})(1+z)^{4.4}$ over the range $0 < z < 0.7$.